MBUD2: DEVELOPMENT AND TESTING OF A NEW VERSION OF MBUD FOR CUED CLASSIFICATION OF MARINE UXO

Project MR-2321

FINAL TECHNICAL REPORT

Erika Gasperikova, Frank Morrison

egasperikova@lbl.gov, 510-486-4930

Lawrence Berkeley National Laboratory
One Cyclotron Road, M/S-74R316C
Berkeley, CA 94720

Ugo Conti

Marine Advanced Research, Inc.
(UCRFS) 1301 S. 46th Street, Bldg. 300A
Richmond, CA 94804

May 15, 2018

TABLE OF CONTENT

ABSTRACT ..... - 1 -

1. INTRODUCTION ..... - 1 -

2. TECHNOLOGY ..... - 3 -

3. LAND TESTS ..... - 8 -

4. UNDERWATER TESTS ..... - 15 -

5. SUMMARY AND CONCLUSIONS ..... - 25 -

6. ACKNOWLEDGMENTS ..... - 25 -

7. REFERENCES ..... - 26 -

8. LIST OF ACRONYMS ..... - 27 -

APPENDIX 1 ..... - 28 -

APPENDIX 2 ..... - 95 -

LIST OF FIGURES

Figure 1. Size vs. depth plot for marine UXO (from DiMarco et al., 2010). Superimposed is the size-depth limit for polarizability resolution for the MBUD system. ..... - 2 -

Figure 2a. Schematic of MBUD2 configuration. ..... - 4 -

Figure 2b. Assembled MBUD2 prototype system. ..... - 4 -

Figure 3a. Inversion results for the principal polarizabilities of 105 mm projectile. ..... - 7 -

Figure 3b. Inversion results for the principal polarizabilities of scrap metal. ..... - 7 -

Figure 4. Test targets. ..... - 8 -

Figure 5. MBUD2 for a cued mode operation. ..... - 9 -

Figure 6. Background responses at the test (a) start and (b) end. Each panel represents one transmitter (x, y, or z) and responses are measured on 12 channels (ch1 - ch12). ..... - 10 -

Figure 7. Target response. Each panel represents one transmitter (x, y, or z) and responses are measured on 12 channels (ch1 - ch12). ..... - 11 -

Figure 8. Principal polarizabilities as a function of time for symmetric test targets - (a) 6-in shotput, (b) 9-in steel spheroid, and (c) 9-in aluminum spheroid. ..... - 12 -

Figure 9. Principal polarizabilities as a function of time for selected UXOs - (a) 60-mm mortar, (b) 2.75-in rocket, and (c) 105-mm projectile. ..... - 13 -

Figure 10. Principal polarizabilities as a function of time for non-UXO targets - (a) anchor, (b) chain, (c) propeller, and (d) scrap metal. ..... - 14 -

Figure 11. Richmond Marina map with the loading ramp (dark blue rectangle) in the north-west corner of the marina and the test location (red rectangle). The NOAA nautical chart indicates the average water depth (in feet). ..... - 15 -

Figure 12. Transport and deployment of MBUD2 in Richmond marina – (a) carrier boat and MBUD2 on a trailer towed behind an SUV, (b) carrier boat and MBUD2, (c) service boat Aria. . - 16 -

Figure 13. MBUD2 transportation between the dock to the test site – (a) MBUD2 towed behind Aria, (b) MBUD2 towed on the side of Aria. ..... - 17 -

Figure 14. MBUD2 underwater deployment – (a) MBUD2 maneuvered by the diver, (b) UXO under MBUD2. ..... - 17 -

Figure 15. MBUD2 underwater field experiment – (a) MBUD2 underwater, (b) data acquisition on Aria. .....- 18 -
Figure 16. Background responses at the test (a) start and (b) end. Each panel represents one transmitter (x, y, or z) and responses are measured on 12 channels (ch1 - ch12). .....- 19 -
Figure 17. Target response. Each panel represents one transmitter (x, y, or z) and responses are measured on 12 channels (ch1 - ch12).....- 20 -
Figure 18. Principal polarizabilities as a function of time for test targets - (a) 6-in shotput, (b) 6-in shotput at the depth of 1.0 m, (c) 9-in steel spheroid, and (d) 9-in aluminum spheroid.....- 22 -
Figure 19. Principal polarizabilities as a function of time for (a) 60-mm mortar, (b) 2.75-in rocket, (c) 105-mm projectile at the depth of 1.0 m at 45°, and (d) scrap metal. .....- 23 -
Figure 20. Comparison of principal polarizabilities for (a) 60-mm mortar, (b) 2.75-in rocket, (c) 105-mm projectile, and (d) 9-in steel spheroid from land (red curves) and underwater tests (blue curves).....- 24 -

LIST OF TABLES

Table 1. Land tests – actual targets placements, and inversion estimated horizontal position, depth, orientation, and polarizability index of the targets. Polarizability responses are plotted in Figures listed in the first column. .....- 30 -
Table 2. Underwater tests - actual targets placements, and inversion estimated horizontal position, depth, orientation, and polarizability index of the targets. Polarizability responses are plotted in Figures listed in the first column. .....- 96 -

ABSTRACT

An improved version of the Marine UXO characterization system MBUD, called MBUD2, has been built and tested. The improved version has a new data acquisition system and incorporates technical modifications to eliminate the noise encountered in seawater with the MBUD1 version. The target is illuminated with fields from three orthogonal transmitters, and the signal is measured using four three component receivers. The receivers are arranged in a configuration that inherently cancels the response of the system to enclosing seawater, and to the response of the air-sea interface for shallow deployments. The system was operated as a cued system. It is mounted on a simple platform on top of a support structure that is transported to a predefined survey location by a carrier boat, lowered to the sea bottom, and maneuvered by a diver. The support structure extends one meter below the system platform to allow for the object placement to a specific location by the diver in low-visibility conditions. MBUD2 is able to classify a detected object on the basis of its size, orientation, depth, shape and metal content. The classification is done by estimating the principal dipole polarizabilities of a target using 33 channels of normalized induction responses computed at 46 logarithmically spaced times between 0.0005 and 0.013 s after transient shutoff. Our results clearly show that MBUD2 can resolve the intrinsic polarizabilities of the target, and that there are very clear distinctions between symmetric intact UXO and irregular scrap metal. The system was tested on land and in San Francisco Bay with excellent results. The system meets the design requirements: it cancels the response of the seawater and air-sea interface, the measurements are stable and repeatable, and target responses estimated from marine measurements are identical to those from land measurements.

1. INTRODUCTION

There continues to be a need for an electromagnetic induction (EMI) system that can characterize UXO in the marine environment. There are many areas in the millions of acres that host

underwater UXO. The US Army Corps of engineers has identified 400 underwater formerly used Defense sites. These sites all have munitions or UXO in less than 40 m of water. A size-depth plot typical for these UXO from DiMarco et al. (2010) was used as a design guide for the first MBUD system and is reproduced here as Figure 1. A compilation of polarizability calculations from a variety of targets for BUD and MBUD is shown by the dashed line in Figure 1. This line indicates that the MBUD system can effectively classify most targets to a depth about 1.2 m.

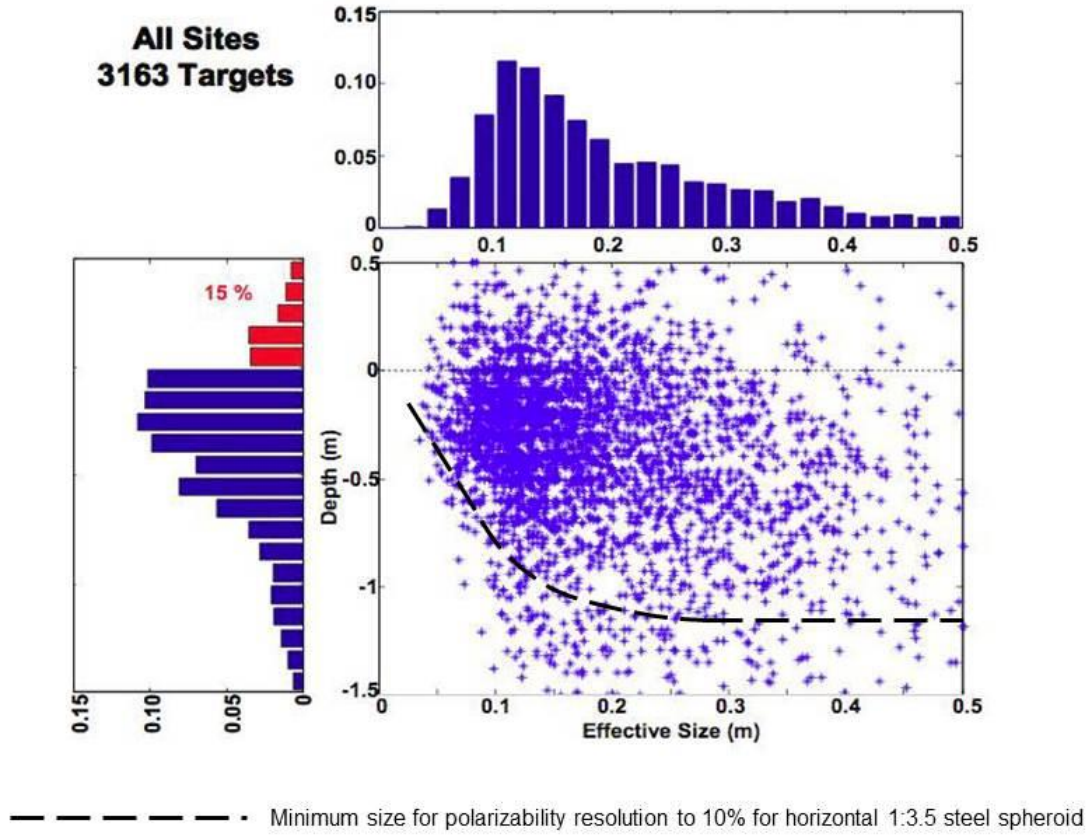

Figure 1. Size vs. depth plot for marine UXO (from DiMarco et al., 2010). Superimposed is the size-depth limit for polarizability resolution for the MBUD system.

Currently wide-area assessment is carried out using low and high-frequency acoustic and magnetometer arrays, both of which must be moved over the area at some distance above the sea bottom. The magnetic response of small targets decreases rapidly with increasing distance from

the object. Further magnetometer surveys can be ineffective if the sea bottom has magnetic rock, sand or gravel (as is common in Hawaii). Low-frequency acoustic scanners have low resolving power for small targets beneath the bottom and may not be effective in water depths of less 3-5 m. Low-frequency acoustic scanning methods may eventually be able to characterize buried medium to large objects, but at present, they can only locate small objects as point scatterers. EMI systems must be operated on the bottom, and in many locations this is often difficult or impossible. Quoting from a recent SERDP symposium, "EMI technology will probably be restricted to cued classification" and eventually will be deployed with a commercial midsized ROV (SERDP/Office of Naval Research Workshop on Acoustic Detection and Classification of UXO in the Underwater Environment, September 2013).

MBUD2 is well suited for this role. The performance of MBUD2 was demonstrated on land and in San Francisco Bay. MBUD2 was operated in a cued mode – the system was stationary and targets were emplaced to various locations by an operator (on land) or a diver (in San Francisco Bay).

2. TECHNOLOGY

A simple open frame MBUD2 prototype system configuration consists of four, three-component, receiver cubes that are at the corners of 1-m^2 area with the three orthogonal transmitters at the center (Figure 2) mounted on a simple platform. Differences in field at symmetrically positioned receivers cancel the response of the seawater and of the air-sea interface for shallow deployments. Note, MBUD2 is using existing components from MBUD1, which constrain possible changes that could be implemented. The pulser and electronics that is inside of the pressure casing is at the other end of the platform. Next to it is also a dedicated pressure casing, inside of which all the signal and power connections are redistributed to a bundle of long cables that reach the surface vessel where the data are processed and analyzed.

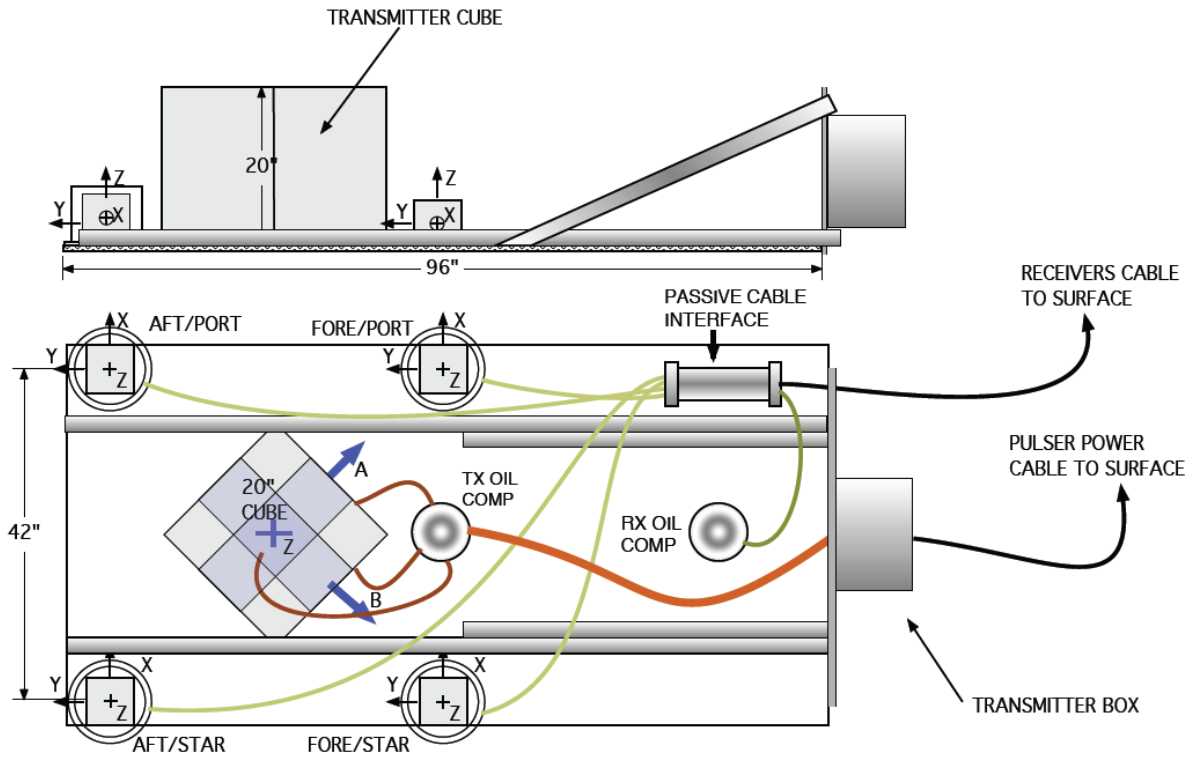

Figure 2a. Schematic of MBUD2 configuration.

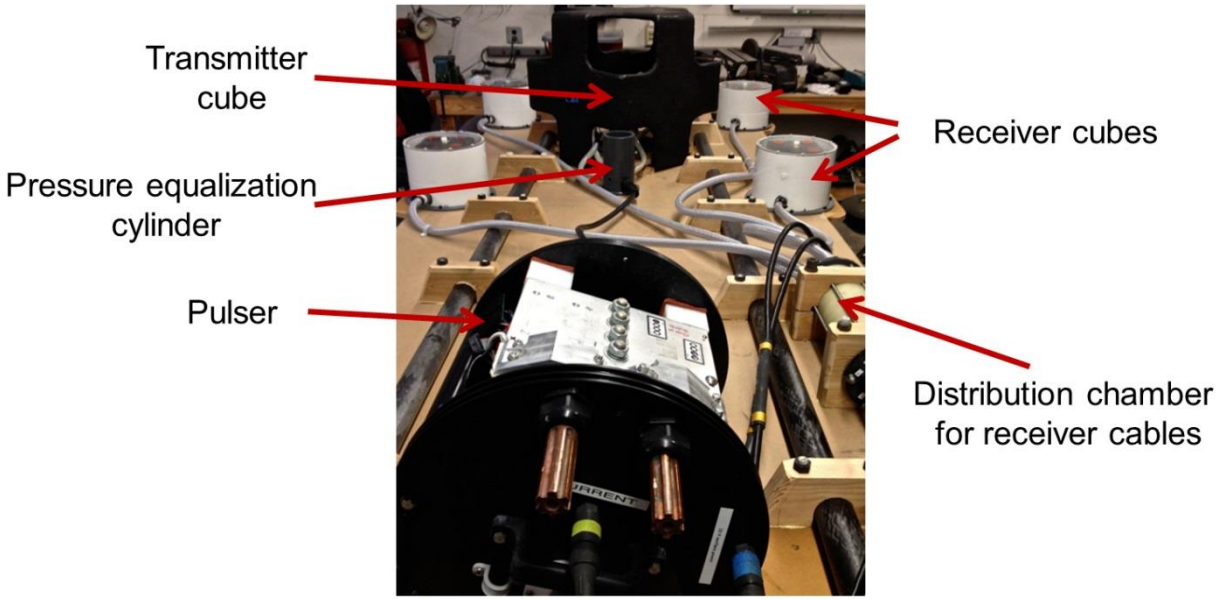

Figure 2b. Assembled MBUD2 prototype system.

The orthogonal transmitter antenna system is completely encased in epoxy glass composite (an average thickness of 4 mm) to avoid any possibility of creating a contact between seawater and the three windings. The cable connections to the receiver windings are made through tubing fittings and the cables are surrounded with reinforced plastic tubing. To further prevent any seawater intrusion, the tubing enclosing the cables and any space around the receiver wiring are oil filled.

This oil filling system is of the pressure-compensating type: the receiver cables with their surrounding tubing are inserted into a pressure-compensating vessel. This vessel includes a piston separating the external seawater from the oil: the piston equalizes the water pressure with the internal pressure preventing any leaks, caused by the water pressure at depth, between the windings and cables connections. The output cable of the antennas is connected to the pulser pressure casing through a deep sea connector (SeaCon 16-pins smk-ccp attachable). The space for the connections between the cable wires and the connector pins is also oil filled in a small custom casing. The main power cable feeding the pulser from the surface vessel enters the pulser pressure casing through a 6-pin wet pluggable high pressure connector.

The control system of the SCR multi-bridge transmitter pulser was implemented using a FPGA (BMB7) and custom isolation boards. The MBUD2 system comprises components from the earlier version of MBUD (MBUD1) which were modified for integration with LBNL electronics. MBUD2 configuration has one BMB7 board and a custom isolation board that sends an acquisition sequence to the pulser which resides in the pulser pressure casing. The BMB7 board was encased in a metal box to shield the high EM fields generated by the power switching from interfering with acquisition board operation. A new SCR control system is mounted inside the modified pulser pressure casing which has also been internally rewired. All power and signal connectors entering the pulser pressure casing are through wet mating high pressure, deep sea connectors. A second BMB7 board performing data acquisition is on the surface vessel with the receivers' outputs connected to the BMB7 channels through a connection box.

Each three-component receiver and amplifier system is housed in a plastic cube 6-in on a side. In order to prevent any possibility of contact between seawater and the receiver terminals and

grounded shields, four plastic pressure cases have been constructed. The signal and power cables to the receivers' casings are inside tubing that are connected from the casings to a pressure-compensating cylinder described above.

The acquisition and discrimination software that was initially developed for the BUD systems (e.g., Gasperikova et al., 2009; Gasperikova et al., 2012), and modified for seawater environment under MR-2228 and MR-2321 (Morrison, 2014), has been further modified for the current MBUD2 configuration. It has been demonstrated that a satisfactory classification scheme is one that determines the principal dipole polarizabilities of a target – a near intact UXO displays a single major polarizability coincident with the long axis of the object and two equal transverse polarizabilities. The induced moment of a target depends on the strength of the transmitted inducing field. The moment normalized by the inducing field is the polarizability. This description of the inherent polarizabilities of a target is a key in discriminating UXO from irregular scrap metal. Figure 3 illustrates a discrimination capability of the system for UXO and scrap metal, respectively. While UXO objects have a single major polarizability coincident with the long axis of the object and two equal transverse polarizabilities (Figure 3a), scrap metal exhibits three distinct principal polarizabilities (Figure 3b). There are clear distinctions between symmetric intact UXO and irregular scrap metal. Moreover, UXOs have unique polarizability signatures, and thus distinctions can be made among various UXOs. These polarizability responses are independent of the target position and orientation when the object is far enough from the system such that it can be assumed to have uniform field illumination and valid dipole approximation. For large objects close to the system, the principal polarizability curves vary, depending on the orientation of the object. Object orientation estimates and equivalent dipole polarizability estimates for large and shallow objects are affected by higher-order (non-dipole) terms induced in objects as a result of source-field gradients along the length of the objects.

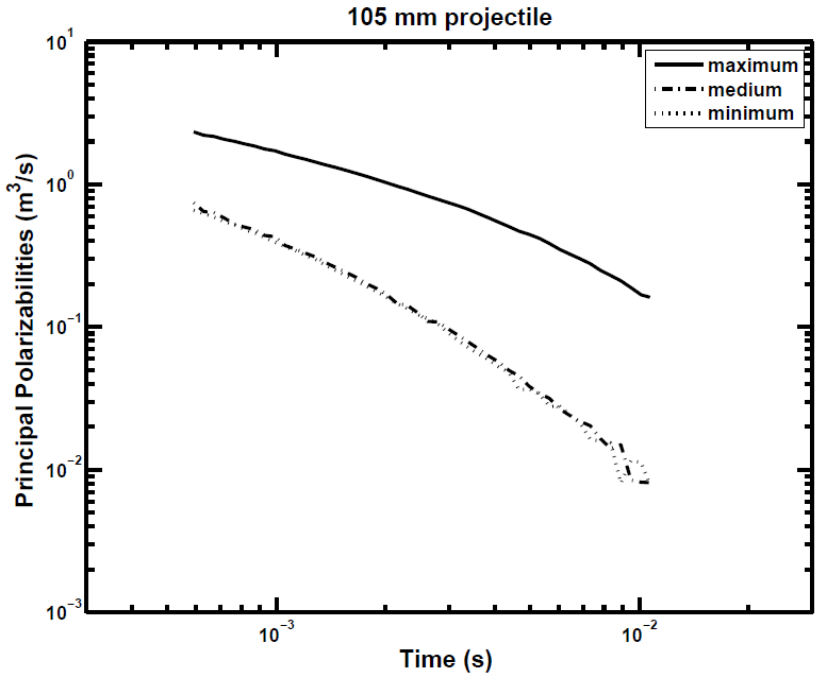

Figure 3a. Inversion results for the principal polarizabilities of 105 mm projectile.

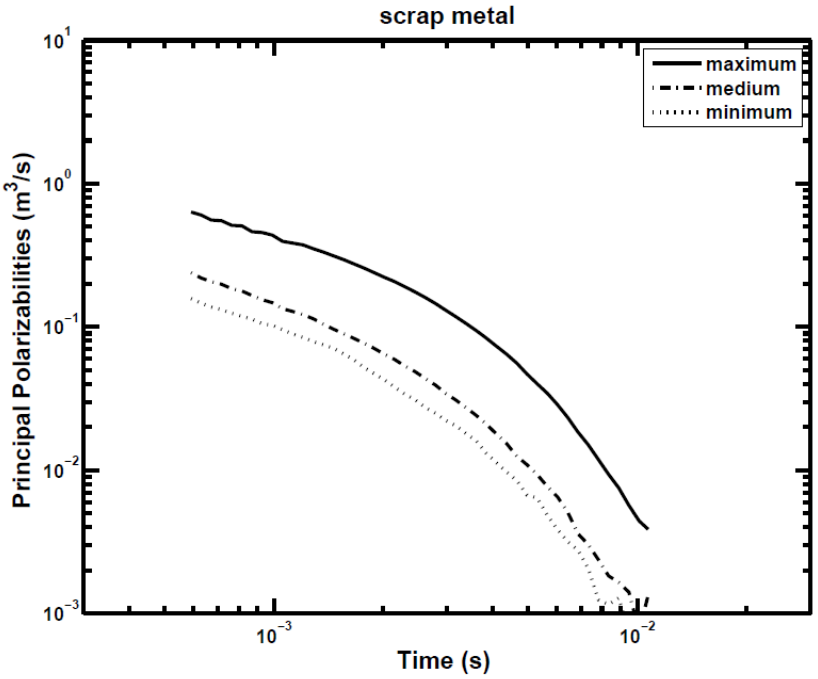

Figure 3b. Inversion results for the principal polarizabilities of scrap metal.

3. LAND TESTS

Two major land tests were performed. The first one at an early stage of the project to test the performance of new hardware and software components, and the second one after the system was sealed and oil-filed before the underwater tests.

Figure 4 shows a collection of targets used both during the land and underwater tests -- 6-in shotput, steel and aluminum 9-in spheroids, 60-mm mortar, 2.75-in rocket, 105-mm projectile, two different types of anchors, two different size propellers, a chain, and a piece of scrap metal.

Figure 4. Test targets.

Figure 5 shows the system during the land tests. The tests were done at the Richmond Field Station, CA. MBUD2 system components are mounted on the top platform. The support structure with six legs extends one meter below the system platform to allow for the object placement to a specific location and orientation. The system is easily handled by four people.

Two nonconductive plates with 6 x 6 4.5-in holes separated by 6-in are centered below the transmitter cube center. The height of the intermediate plate is adjustable. The combination of two plates and a uniform holes distribution allows for an accurate object position with respect to the center of the system even in low-visibility conditions that might be encountered during surveys.

Figure 5. MBUD2 for a cued mode operation.

Figure 6 shows background responses at the start (Figure 6a) and at the end (Figure 6b) of the test, respectively. The figure illustrates that the system was stable, measurements were repeatable, and that the noise level was much lower than the target response shown in Figure 7. Upper, middle, and lower panels show responses measured on 12 channels (ch1 - ch12) for X, Y, and Z transmitters, respectively. For the background response, all channels show more-or-less random variation at a very low value that defines the noise level. This background response is considered as the system and the site calibration response that is subtracted from the measured response allowing 1:1 comparison of the measurements and results from different field sites. This was especially important for the measurements at the Richmond Field Station, where variable high-level cultural noise was present. When a target is present (Figure 7) the response is

an order of magnitude larger and shows a typical response decay, that enables reliable object characterization.

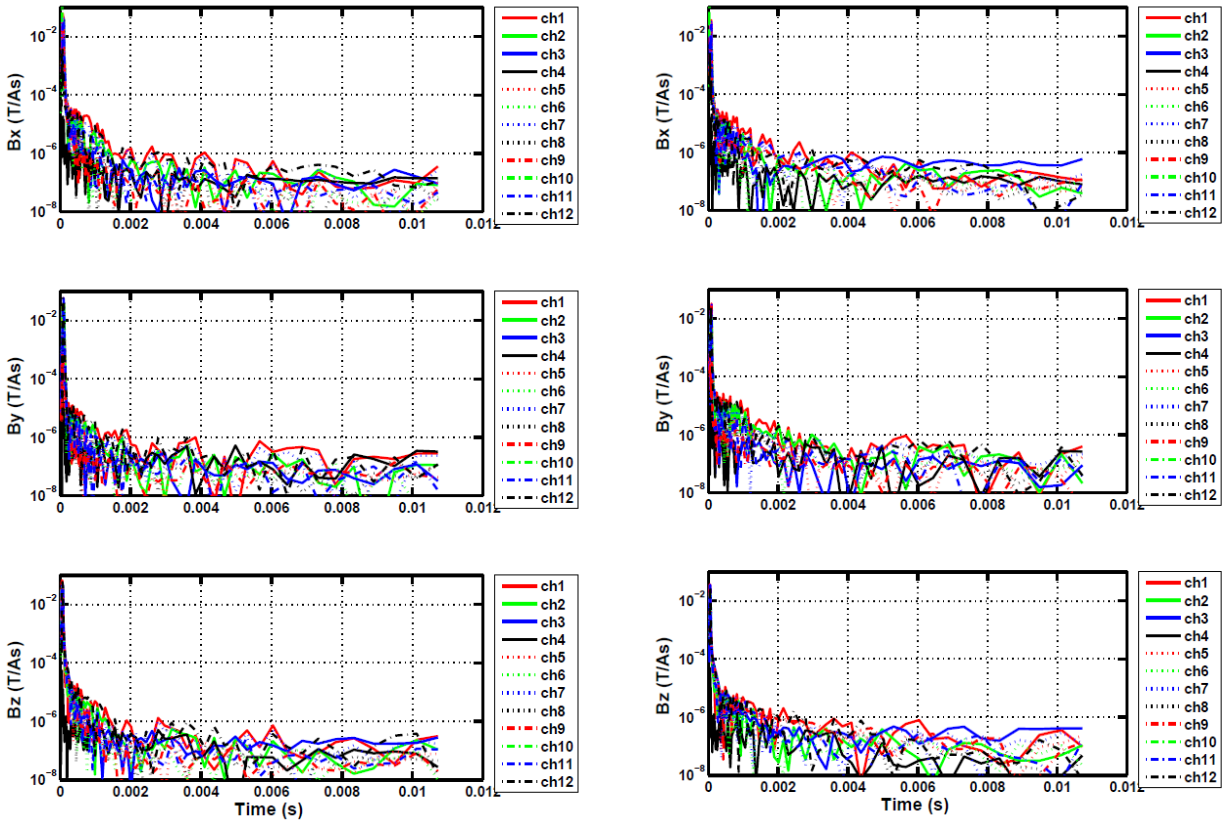

(a) (b)

Figure 6. Background responses at the test (a) start and (b) end. Each panel represents one transmitter (x, y, or z) and responses are measured on 12 channels (ch1 - ch12).

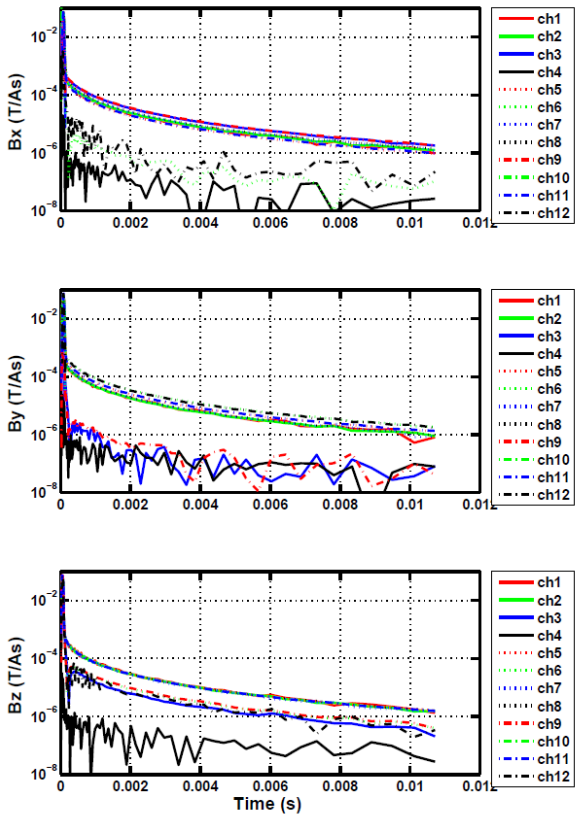

Figure 7. Target response. Each panel represents one transmitter (x, y, or z) and responses are measured on 12 channels (ch1 - ch12).

Following Gasperikova et al. (2009), estimating the principal dipole polarizabilities of a target was done using 33 channels of normalized induction responses computed at 46 logarithmically spaced times between 0.0005 and 0.013 s after turnoff. Soundings for each object and position were differenced with the background reference sounding taken within 30-40 minutes of the measurement, without any object present, and inversion results were displayed on the computer screen. Intrinsic polarizability responses of symmetric test targets, UXOs, and non-UXO targets are shown in Figures 8, 9, and 10, respectively. Appendix 1 contains responses and parameters of all targets used in the land tests. Table 1 in Appendix 1 shows that each object location and orientation were estimated within a few centimeters and degrees, respectively, of the actual values. Excellent performance and discrimination capabilities of the system are illustrated by the 2.75-in rocket and 6-in steel shotput, both clearly characterized down to 0.7 m, with the 105–mm projectile characterized down to a depth of 1.0 m, and both 2.75-in rocket and 105–mm projectile correctly characterized even when located outside of the system footprint.

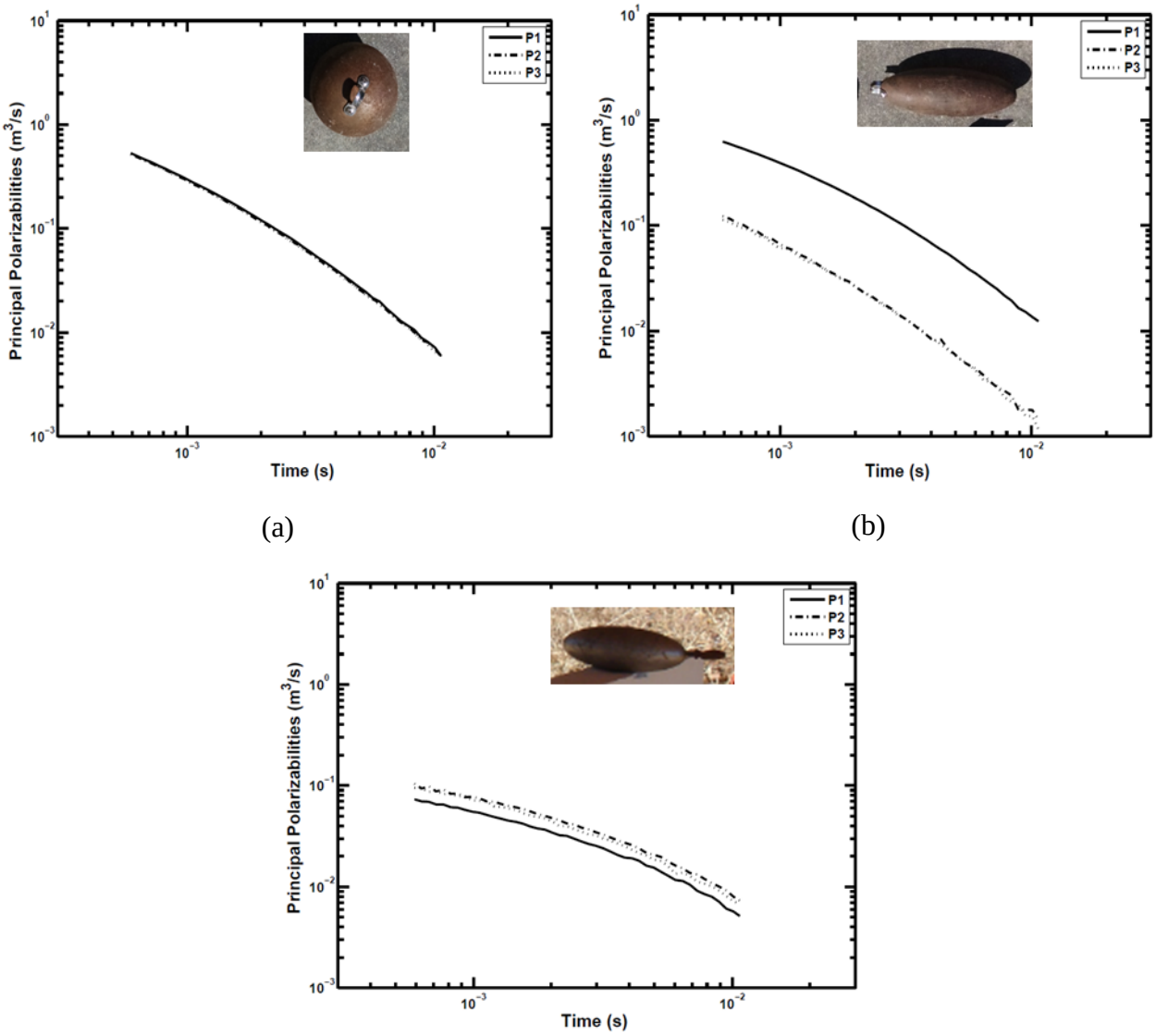

Figure 8. Principal polarizabilities as a function of time for symmetric test targets - (a) 6-in shotput, (b) 9-in steel spheroid, and (c) 9-in aluminum spheroid.

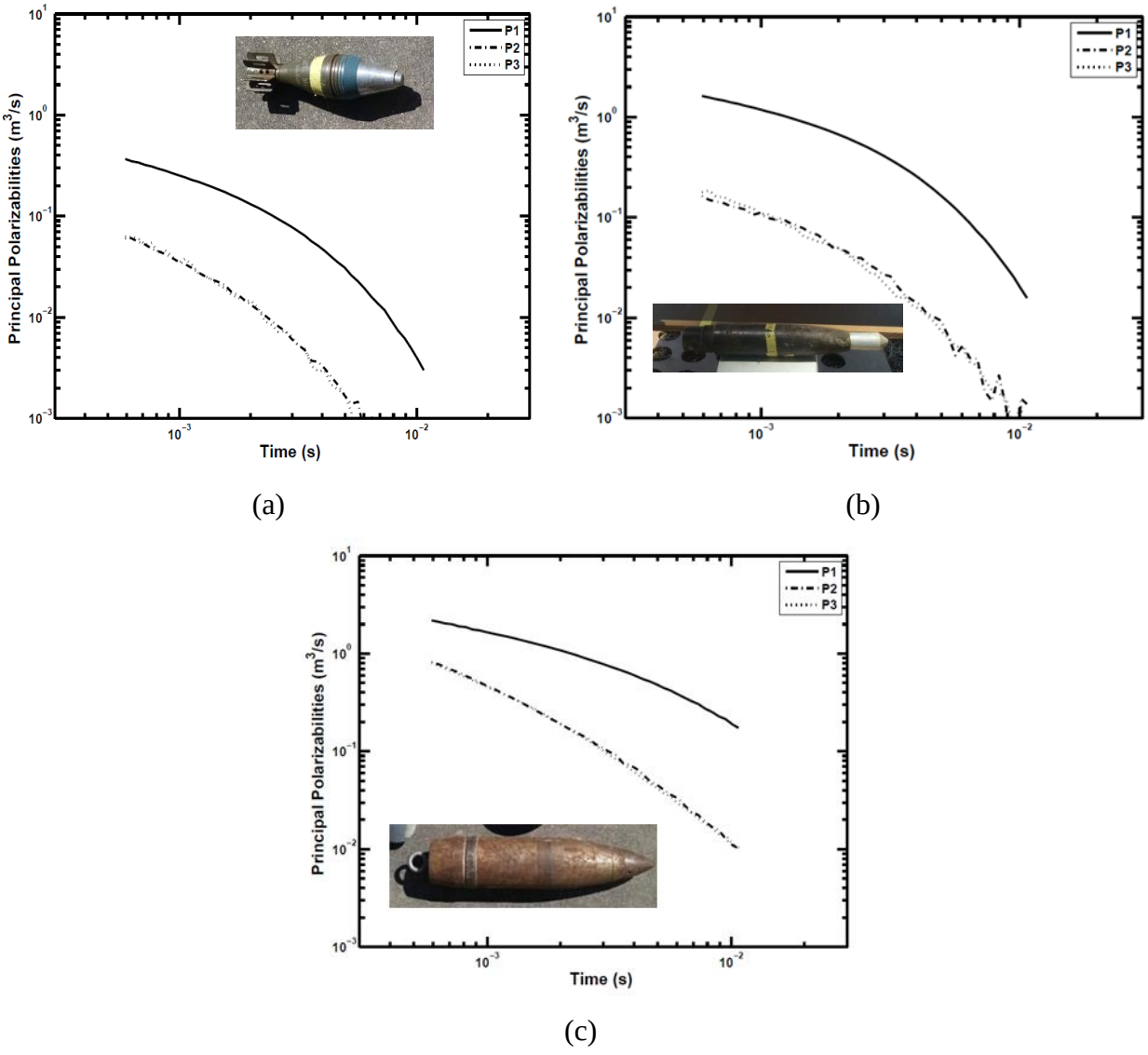

Figure 9. Principal polarizabilities as a function of time for selected UXOs - (a) 60-mm mortar, (b) 2.75-in rocket, and (c) 105-mm projectile.

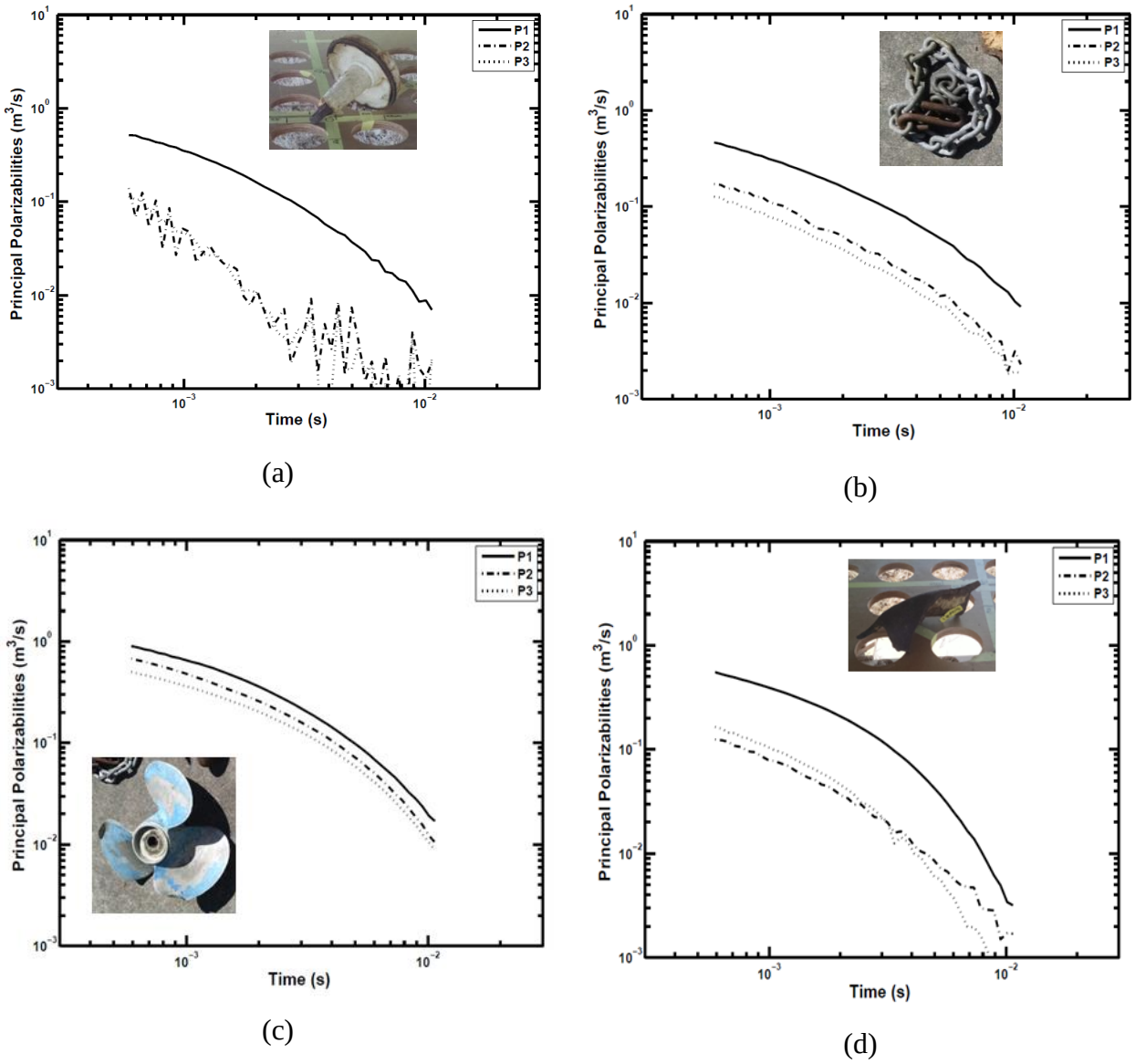

Figure 10. Principal polarizabilities as a function of time for non-UXO targets - (a) anchor, (b) chain, (c) propeller, and (d) scrap metal.

4. UNDERWATER TESTS

The underwater tests were done in Richmond Marina Bay Yacht Harbor (Figure 11). The area is filled with 'bay mud', which is a soft unconsolidated silty clay. The water depth in the marina varies from 3 to 20 feet (1-6 m). The measurements were done in the area with a water depth of 6 m.

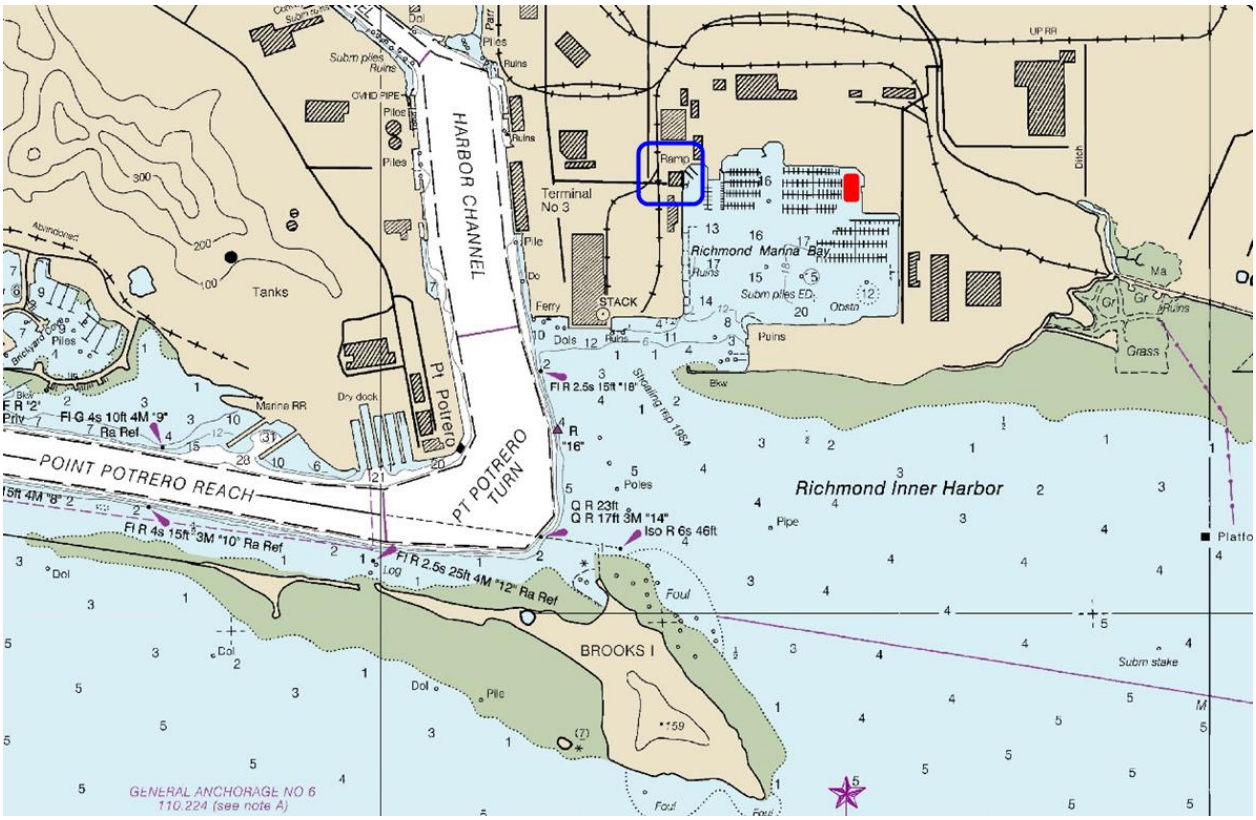

Figure 11. Richmond Marina map with the loading ramp (dark blue rectangle) in the north-west corner of the marina and the test location (red rectangle). The NOAA nautical chart indicates the average water depth (in feet).

The MBUD2 system was towed to the marina on a trailer (Figure 12a). The carrier boat (Figure 12b) was designed specifically for this project during MBUD1 project, and it is capable of delivering payloads, i.e., MBUD2, between the hulls with a gantry crane system that is suitable for shallow or deep water work. The carrier boat with its load (MBUD2) was then lowered into the water using the marina boat ramp (Figure 12b).

(a)

(b)

(c)

Figure 12. Transport and deployment of MBUD2 in Richmond marina – (a) carrier boat and MBUD2 on a trailer towed behind an SUV, (b) carrier boat and MBUD2, (c) service boat Aria.

The service boat, Aria, (Figure 12c) was used to ferry the carrier boat with MBUD2 to and from the test location (Figure 13) either towed behind Aria (Figure 13a) or on the side of Aria (Figure 13b). At the test location, the MBUD2 system was lowered into the water (Figure 14a) after a preliminary noise test in air. The system was designed for easy underwater handling by the diver as the apparent weight is reduced by the buoyancy of the system. With the MBUD2 on the bottom, the diver detached the winch cables (Figure 14a), and the carrier boat was moved away from the test site. A bundle of signal and power cables connected the underwater system with the

service boat Aria, where the high current, low voltage DC source for the pulser, data acquisition system and computer were located (Figure 15b).

(a) (b)

Figure 13. MBUD2 transportation between the dock to the test site – (a) MBUD2 towed behind Aria, (b) MBUD2 towed on the side of Aria.

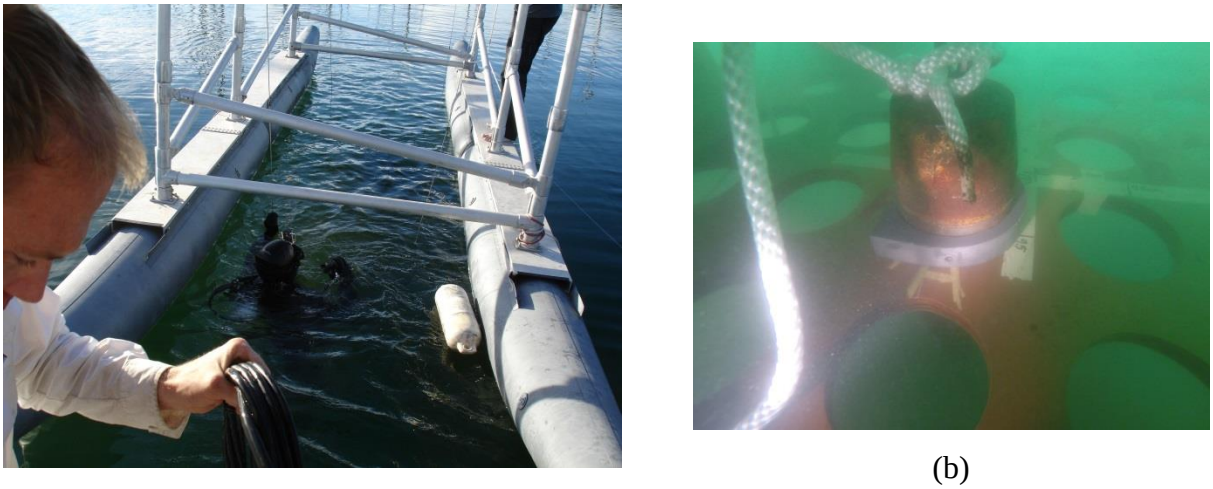

(a) (b)

Figure 14. MBUD2 underwater deployment – (a) MBUD2 maneuvered by the diver, (b) UXO under MBUD2.

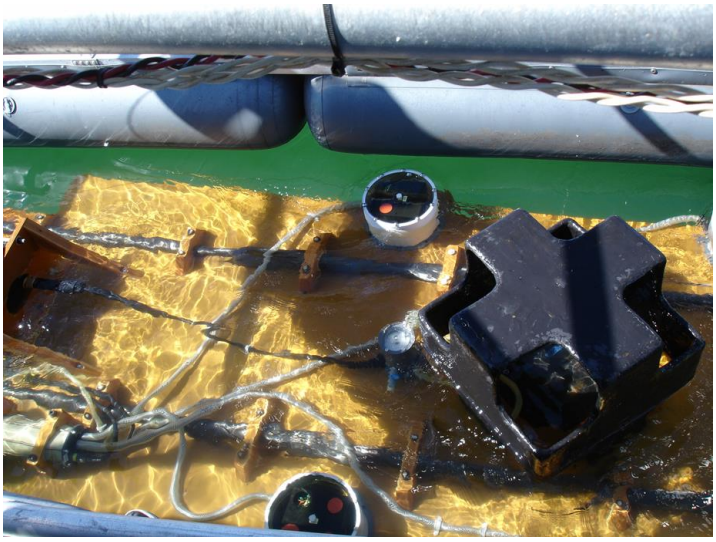

(a)

(b)

Figure 15. MBUD2 underwater field experiment – (a) MBUD2 underwater, (b) data acquisition on Aria.

Figure 16 shows the background responses at the start (Figure 16a) and at the end (Figure 16b) of the test, respectively. Like the land tests, the figure illustrates that the system was stable, measurements were repeatable and that the noise level was much lower than the target response shown in Figure 17. Again, the upper, middle, and lower panels show responses measured on 12 channels (ch1 - ch12) for X, Y, and Z transmitters. For the background response, all channels are within the noise level, which was actually lower than during our land tests (Figure 6), as there was no industrial/cultural noise present as encountered at the Richmond Field Station. When the target is present (Figure 17) the response is an order of magnitude larger, and again shows the characteristic response decay.

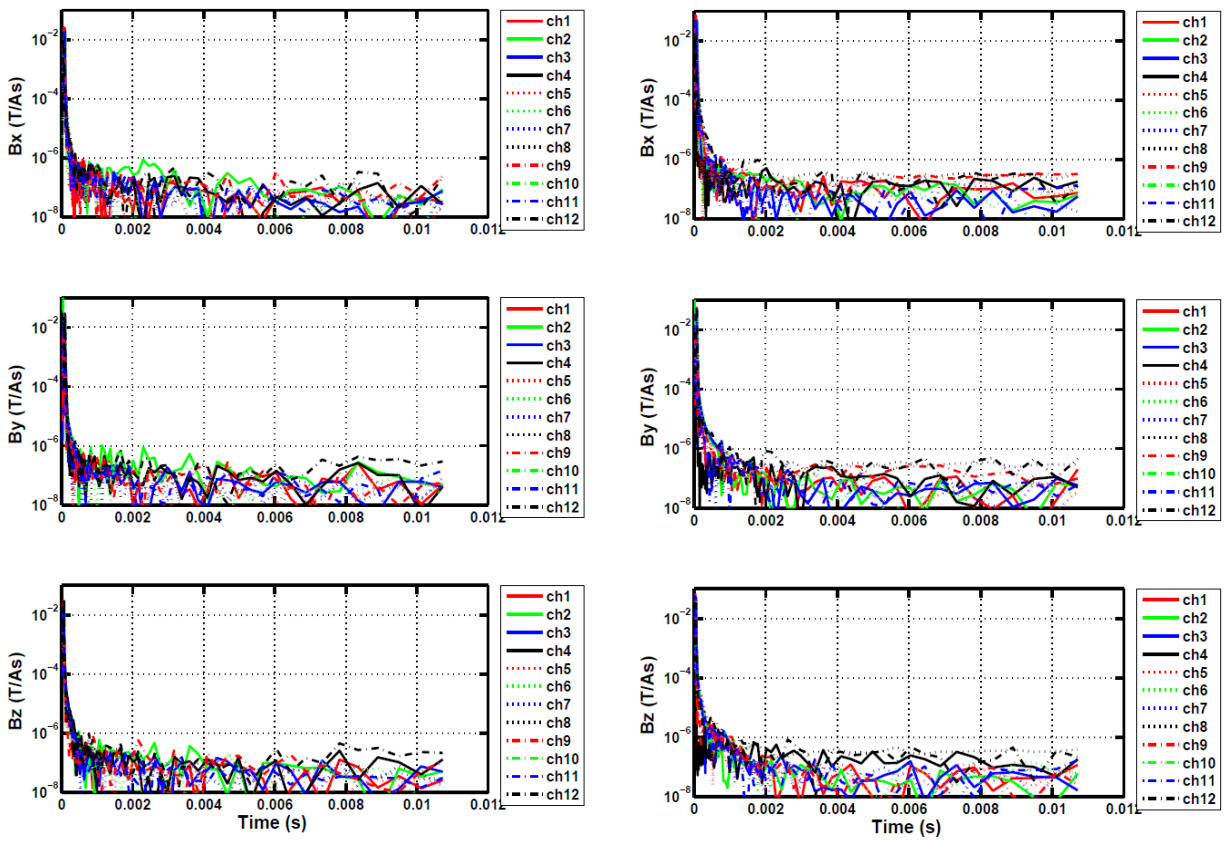

(a) (b)

Figure 16. Background responses at the test (a) start and (b) end. Each panel represents one transmitter (x, y, or z) and responses are measured on 12 channels (ch1 - ch12).

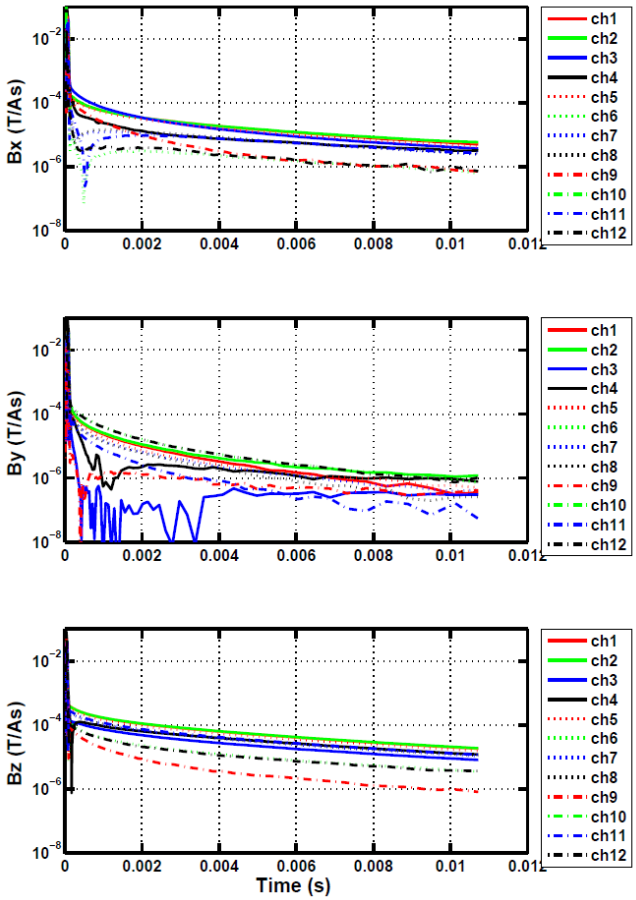

Figure 17. Target response. Each panel represents one transmitter (x, y, or z) and responses are measured on 12 channels (ch1 - ch12).

MBUD2 was operated in the cued mode. The system was tested over typical marine UXO targets and scrap – a 6-in shotput, 9-in steel and aluminum spheroids, 60-mm mortar, 2.75-in rocket, 105-mm projectile, anchor, and a piece of scrap that were placed at multiple positions and orientations. The MBUD2 support structure described above allowed the diver to accurately place the object into a specified position and orientation with respect to the center of the system (Figure 14b). Soundings were collected for each object and position, differenced with background reference soundings taken within 30-40 minutes of the measurement, without any object present, and inversion results were displayed on the computer screen. While this was still a two-step process – the data acquisition was separate from the data processing and inversion, it allowed for data quality checks on the service boat. Estimating the principal dipole polarizabilities of a target was done using 33 channels of normalized induction responses computed at 46 logarithmically spaced times between 0.0005 and 0.013 s after transient shutoff.

The three discriminating polarizability responses along with the object depth and horizontal location with respect to the center of the transmitter cube, orientation, and polarizability index were recorded (Table 2 in Appendix 2). The polarizability index is an average value of the product of time (in seconds) and polarizability rate (in m^3/s). Responses of all targets used during the underwater tests are included in Appendix 2.

Intrinsic polarizability responses of selected test targets and UXOs are shown in Figures 18 and 19 respectively. Figure 18b demonstrates that the 9-in shotput can be characterized 1.0 m away from the system, although the response is noisier (compared to Figure 18a). Figures 18c and 18d demonstrate the system discrimination capability based on a metal type using 9-in steel (Figure 18c) and aluminum (Figure 18d) spheroids -- polarizability responses produced by an object of the same size and shape, but made from different materials are characteristically different. Figure 19c illustrates that 105-mm projectile polarizabilities, depth and orientation were accurately estimated by the inversion.

The results from underwater tests compare very well with the land test results. Figure 20 shows responses from both tests for the 60-mm mortar (Figure 20a), 2.75-in rocket (Figure 20b), 105-mm projectile (Figure 20c) and 9-in steel spheroid (Figure 20d). The results from underwater tests are plotted in blue, while the land results are plotted in red. Target responses estimated from marine measurements are within 10% of those from land measurements. The largest discrepancies and noise are present at late times when signals are small.

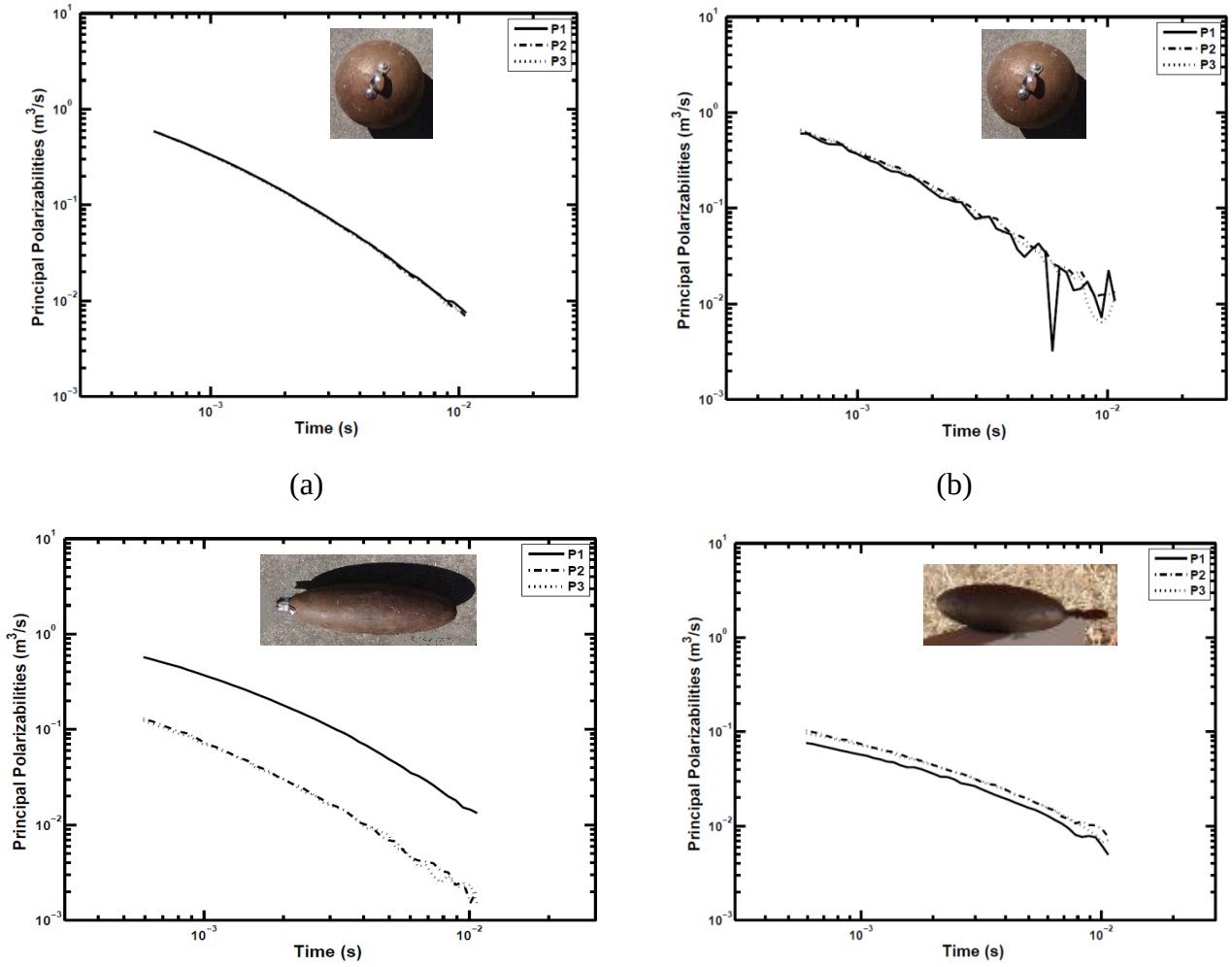

Figure 18. Principal polarizabilities as a function of time for test targets - (a) 6-in shotput, (b) 6-in shotput at the depth of 1.0 m, (c) 9-in steel spheroid, and (d) 9-in aluminum spheroid.

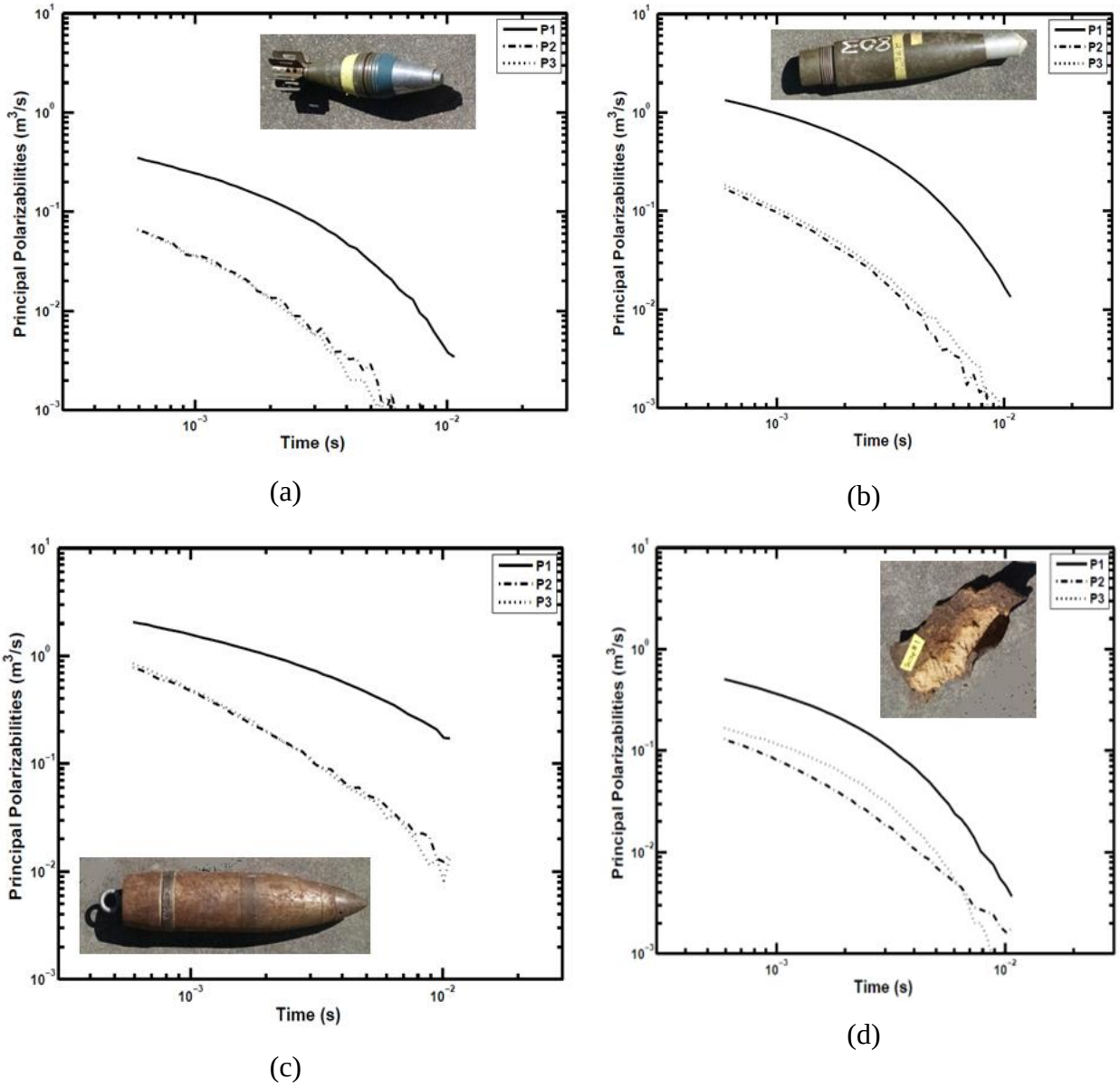

Figure 19. Principal polarizabilities as a function of time for (a) 60-mm mortar, (b) 2.75-in rocket, (c) 105-mm projectile at the depth of 1.0 m at 45°, and (d) scrap metal.

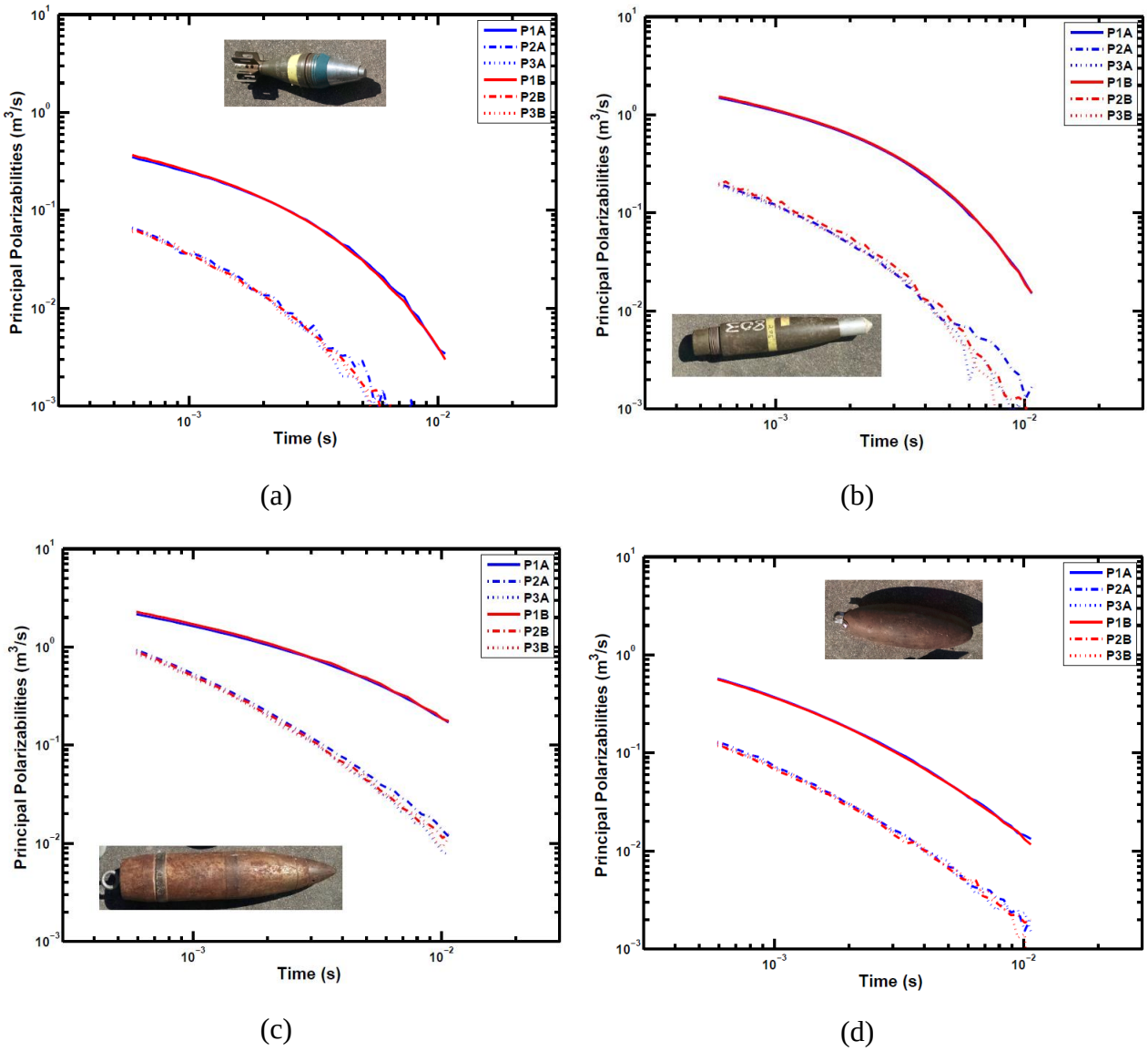

Figure 20. Comparison of principal polarizabilities for (a) 60-mm mortar, (b) 2.75-in rocket, (c) 105-mm projectile, and (d) 9-in steel spheroid from land (red curves) and underwater tests (blue curves).

5. SUMMARY AND CONCLUSIONS

The MBUD2 system was operated in the cued mode, and tested on land and in San Francisco Bay at water depth of 6 m. The tests in San Francisco Bay demonstrated that the system performed according to the design, and the response of the system to enclosing seawater, and to the response of the air-sea interface for shallow deployments, is cancelled. This prototype was properly sealed, and there were no water leaks. The carrier boat used in this experiment is suitable for shallow or deep water deployments. The acquired data also demonstrated MBUD2 stability and measurements repeatability. The results from underwater tests were compared with the results from land tests, and target responses estimated from marine measurements were identical to those from land measurements. The inversion accurately estimates the depth, horizontal location, and orientation of the target. Each target is characterized by a unique set of principal polarizabilities. Furthermore, results of 9-in steel and aluminum spheroids demonstrate that the current system is able to classify a detected object not only on the basis of its size, depth, orientation, shape but also the metal content.

6. ACKNOWLEDGMENTS

This research has been supported by the Office of Management, Budget, and Evaluation, of the U.S. Department of Energy under Contract No. DE-AC02-05CH11231, and the U.S. Department of Defense under the SERDP Project MR-2321. We thank Aria crew: Mark Gundersen (diver), Thomas Dwyer, and Kurt diSessa for their help during the underwater deployment. We thank Edward Nichols (LBNL) for a careful and constructive internal review.

7. REFERENCES

DiMarco, R., Keiswetter, D., and Bell, T., 2010, Deep Water Munitions Detection System, Final Report, ESTCP Project MM-0739, http://www.serdp.org/Program-Areas/Munitions-Response/Underwater-Environments/MR-200739.

Gasperikova, E., Smith, J.T., Morrison, H.F., Becker, A., and Kappler, K, 2009, UXO detection and identification based on intrinsic target polarizabilities: Geophysics,74, B1-B8.

Gasperikova, E., V. Vytla, T. Jobe, L. Kennedy, and X. Zhu, 2012, Cued survey with a hand-held UXO discriminator at Camp Beale, CA: ESTCP Demonstration Report, MR-201166.

Morrison, H.F., 2013, Development and Testing of an Engineering Prototype for a Marine Version of the Berkeley Unexploded Ordnance Discriminator (BUD), Final report, SERDP MR-2228.

Morrison, H.F., 2014, Development and Testing of an Engineering Prototype for a Marine Version of the Berkeley Unexploded Ordnance Discriminator: Phase II, Final report, SERDP MR-2321.

SERDP/Office of Naval Research Workshop on Acoustic Detection and Classification of UXO in the Underwater Environment, Final Report, September 2013.

8. LIST OF ACRONYMS

BUD	Berkeley Unexploded Ordnance Discriminator
EM	ElectroMagnetic
EMI	Electromagnetic Induction
FPGA	Field-Programmable Gate Array
LBNL	Lawrence Berkeley National Laboratory
MAR	Marine Advanced Research
MBUD	Marine UXO characterization system
ROV	Remotely Operated underwater Vehicle
SCR	Silicon Controlled Rectifier
SERDP	Strategic Environmental Research and Development Program
UXO	Unexploded Ordnance

APPENDIX 1

Land tests were carried out at the Richmond Field Station, CA with the following layout. The intermediate plate of the support structure is used to describe target locations. The coordinate system is shown in grey, and (0, 0) is the center of the transmitter cube. The accuracy of targets' positioning to a certain location was within a few centimeters.

P1 = (0.0; 0.0) m	P5 = (0.0; 0.70) m
P2 = (-0.23; 0.0) m	P22 = (-0.23; 0.23) m
P3 = (-0.15; 0.15) m	P33 = (-0.08; 0.08) m
P4 = (-0.15, 0.70) m	P44 = (0.08; -0.08) m

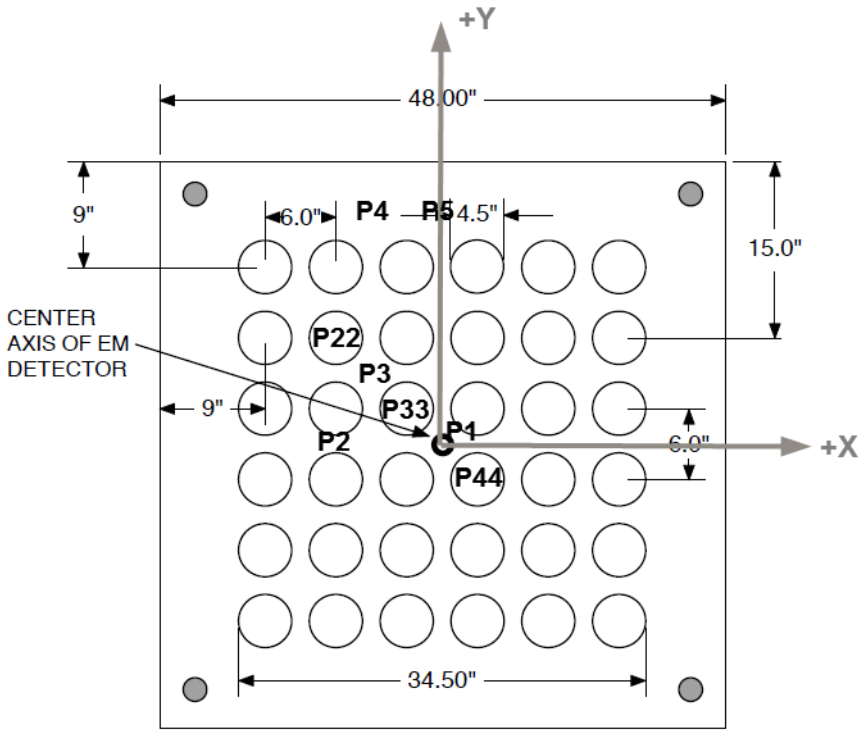

The target vertical orientation (orient-v) is given with respect to positive z (down), i.e., horizontal is 90° and vertical is 0°. The target horizontal orientation (orient-xy) is given with respect to positive x, i.e., +x direction is 0°, +y direction is 90°, –x direction is ±180°, and –y direction is -90°.

Note: To be consistent with the inversion, which estimates the depth to the center of the object, the actual depth of known objects is also given to the object center. For irregular objects or scrap a distance to the plate holding the target is given instead, which results in a larger discrepancy between actual and estimated depths.

Table 1. Land tests – actual targets placements, and inversion estimated horizontal position, depth, orientation, and polarizability index of the targets. Polarizability responses are plotted in Figures listed in the first column.

Figure number	Target	Actual				Inversion Estimates					
		Position	Depth (m)	Orient-v	Orient-xy	X (m)	Y(m)	Depth (m)	Pindex	Orient-v	Orient-xy
Figure A1-1	anchor 1	P22	0.7*	N/A	N/A	-0.19	0.2	0.61	101	114	136
Figure A1-2	anchor 1	P33	0.4*	N/A	N/A	-0.03	0.03	0.33	118	112	131
Figure A1-3	anchor 1	P33	0.4*	N/A	N/A	-0.04	0.03	0.33	115	112	130
Figure A1-4	anchor 1	P33	0.4*	N/A	N/A	-0.03	0.03	0.33	117	112	130
Figure A1-5	chain	P3	0.4*	N/A	N/A	-0.15	0.16	0.39	98	59	11
Figure A1-6	propeller large	P1	0.7*	N/A	N/A	-0.01	-0.01	0.62	429	1	143
Figure A1-7	propeller large	P3	0.7*	N/A	N/A	-0.18	0.18	0.62	419	4	-136
Figure A1-8	propeller large	P1	0.4*	N/A	N/A	0.04	0.01	0.32	403	5	161
Figure A1-9	propeller large	P3	0.4*	N/A	N/A	-0.15	0.2	0.32	426	21	-120
Figure A1-10	propeller small	P1	0.4*	N/A	N/A	0.01	0	0.31	129	3	-166
Figure A1-11	propeller small	P3	0.4*	N/A	N/A	-0.15	0.21	0.31	123	4	-87
Figure A1-12	scrap of metal	P3	0.4*	N/A	N/A	-0.18	0.15	0.35	141	78	105
Figure A1-13	6-in shotput	P1	0.32	N/A	N/A	0	0.01	0.31	201	119	-39
Figure A1-14	6-in shotput	P1	0.62	N/A	N/A	0	0.02	0.62	239	123	73
Figure A1-15	6-in shotput	P22	0.32	N/A	N/A	-0.22	0.24	0.33	205	18	-115
Figure A1-16	6-in shotput	P22	0.62	N/A	N/A	-0.22	0.26	0.63	231	106	49
Figure A1-17	6-in shotput	P2	0.32	N/A	N/A	-0.28	0.03	0.31	202	84	48
Figure A1-18	6-in shotput	P3	0.32	N/A	N/A	-0.18	0.18	0.31	200	36	76
Figure A1-19	9-in steel spheroid	P1	0.35	90	90	0	-0.01	0.35	131	90	90
Figure A1-20	9-in steel spheroid	P2	0.35	90	90	-0.27	0.02	0.37	139	93	90
Figure A1-21	9-in steel spheroid	P3	0.35	90	90	-0.17	0.19	0.35	131	93	91
Figure A1-22	9-in steel spheroid	P3	0.2	90	90	-0.17	0.17	0.19	123	91	90

* distance to the plate holding the target

Figure number	Target	Actual				Inversion Estimates					
		Position	Depth (m)	Orient-v	Orient-xy	X (m)	Y(m)	Depth (m)	Pindex	Orient-v	Orient-xy
Figure A1-23	9-in steel spheroid	P3	0.2	90	135	-0.19	0.17	0.19	127	91	131
Figure A1-24	9-in steel spheroid	P3	0.2	90	135	-0.19	0.17	0.19	132	91	131
Figure A1-25	105-mm projectile	P1	0.35	90	90	0	0.01	0.36	938	91	89
Figure A1-26	105-mm projectile	P1	0.65	90	90	0.01	-0.02	0.64	860	90	89
Figure A1-27	105-mm projectile	P22	0.4	0	N/A	-0.24	0.24	0.44	814	2	165
Figure A1-28	105-mm projectile	P22	0.7	0	N/A	-0.24	0.24	0.74	857	2	102
Figure A1-29	105-mm projectile	P2	0.35	90	90	-0.27	-0.01	0.36	912	92	91
Figure A1-30	105-mm projectile	P2	0.65	90	90	-0.24	-0.01	0.65	925	90	89
Figure A1-31	105-mm projectile	P3	0.35	90	90	-0.16	0.17	0.35	966	92	91
Figure A1-32	105-mm projectile	P3	0.95	90	90	-0.14	0.18	0.94	964	89	89
Figure A1-33	105-mm projectile	P3	0.65	90	90	-0.14	0.15	0.65	921	89	88
Figure A1-34	105-mm projectile	P3	0.73	90	90	-0.13	0.21	0.73	907	89	89
Figure A1-35	105-mm projectile	P3	0.35	90	135	-0.13	0.15	0.35	923	90	133
Figure A1-36	105-mm projectile	P3	0.75	45	N/A	-0.1	0.29	0.83	960	47	85
Figure A1-37	105-mm projectile	P44	0.4	0	N/A	0.08	-0.07	0.46	888	3	-8
Figure A1-38	105-mm projectile	P44	0.7	90	N/A	0.08	-0.06	0.73	916	4	109
Figure A1-39	105-mm projectile	P4	0.35	90	0	-0.17	0.64	0.35	951	91	-1
Figure A1-40	105-mm projectile	P4	0.75	60	N/A	-0.16	0.87	0.74	818	63	94
Figure A1-41	105-mm projectile	P4	0.75	60	N/A	-0.16	0.83	0.75	780	56	96
Figure A1-42	2.75-in rocket	P1	0.36	90	90	0.01	-0.02	0.36	362	90	90
Figure A1-43	2.75-in rocket	P1	0.66	90	90	0	-0.02	0.63	299	90	89
Figure A1-44	2.75-in rocket	P22	0.7	0	N/A	-0.24	0.25	0.76	324	7	165
Figure A1-45	2.75-in rocket	P2	0.36	90	90	-0.28	0	0.37	365	92	92
Figure A1-46	2.75-in rocket	P2	0.36	90	90	-0.28	0	0.37	359	94	94
Figure A1-47	2.75-in rocket	P2	0.66	90	90	-0.24	-0.01	0.65	342	91	91
Figure A1-48	2.75-in rocket	P3	0.36	90	90	-0.15	0.18	0.36	358	91	91
Figure A1-49	2.75-in rocket	P3	0.66	90	90	-0.17	0.17	0.67	378	90	91
Figure A1-50	2.75-in rocket	P3	0.36	-30	N/A	-0.15	0.23	0.3	349	125	64
* distance to the plate holding the target											

Figure number	Target	Actual				Inversion Estimates					
		Position	Depth (m)	Orient-v	Orient-xy	X (m)	Y(m)	Depth (m)	Pindex	Orient-v	Orient-xy
Figure A1-51	2.75-in rocket	P3	0.36	120	N/A	-0.15	0.19	0.33	360	122	58
Figure A1-52	2.75-in rocket	P3	0.36	90	-135	-0.15	0.2	0.37	382	91	50
Figure A1-53	2.75-in rocket	P44	0.7	0	N/A	0.09	-0.03	0.77	362	2	-35
Figure A1-54	2.75-in rocket	P4	0.36	90	0	-0.12	0.71	0.36	374	88	-1
Figure A1-55	2.75-in rocket	P4	0.36	90	0	-0.11	0.7	0.35	364	88	0
Figure A1-56	2.75-in rocket	P5	0.36	90	0	0.02	0.7	0.33	322	88	-1
Figure A1-57	60-mm mortar	P3	0.37	90	90	-0.16	0.19	0.35	73	95	94
Figure A1-58	60-mm mortar	P3	0.37	-30	N/A	-0.12	0.23	0.32	81	119	57
Figure A1-59	60-mm mortar	P3	0.37	120	N/A	-0.14	0.19	0.32	79	120	55
Figure A1-60	60-mm mortar	P3	0.37	90	180	-0.14	0.17	0.36	81	89	-1
Figure A1-61	60-mm mortar	P3	0.37	90	0	-0.17	0.21	0.36	79	90	90
Figure A1-62	60-mm mortar	P3	0.37	90	-90	-0.17	0.21	0.36	79	90	90
* distance to the plate holding the target											

Figure A1−1: Principal polarizabilities as a function of time − anchor1, position = P22, depth = 0.7 m, orient−v = N/A,orient−xy = N/A

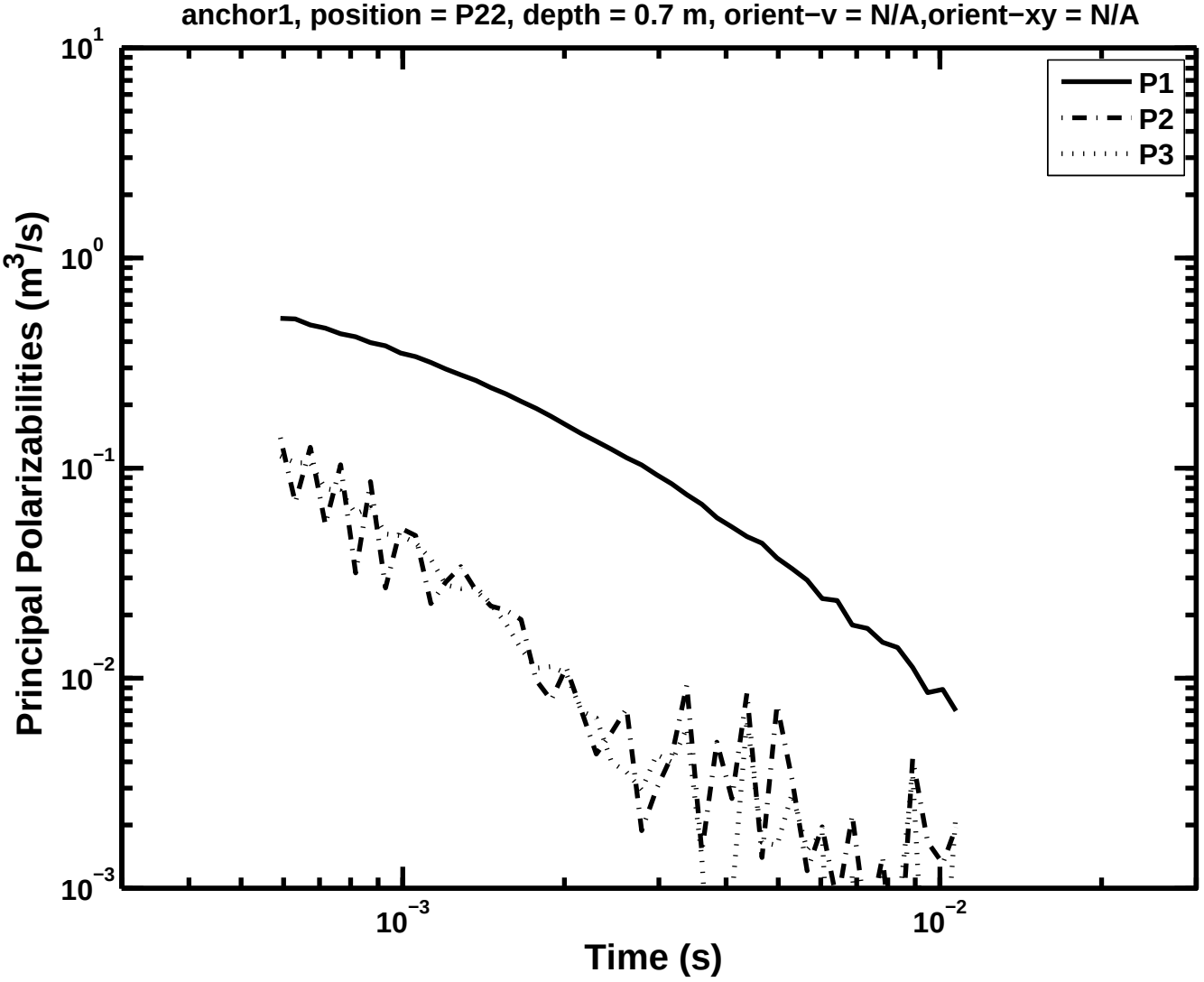

Figure A1−2: Principal polarizabilities as a function of time − anchor1, position = P33, depth = 0.4 m, orient−v = N/A,orient−xy = N/A

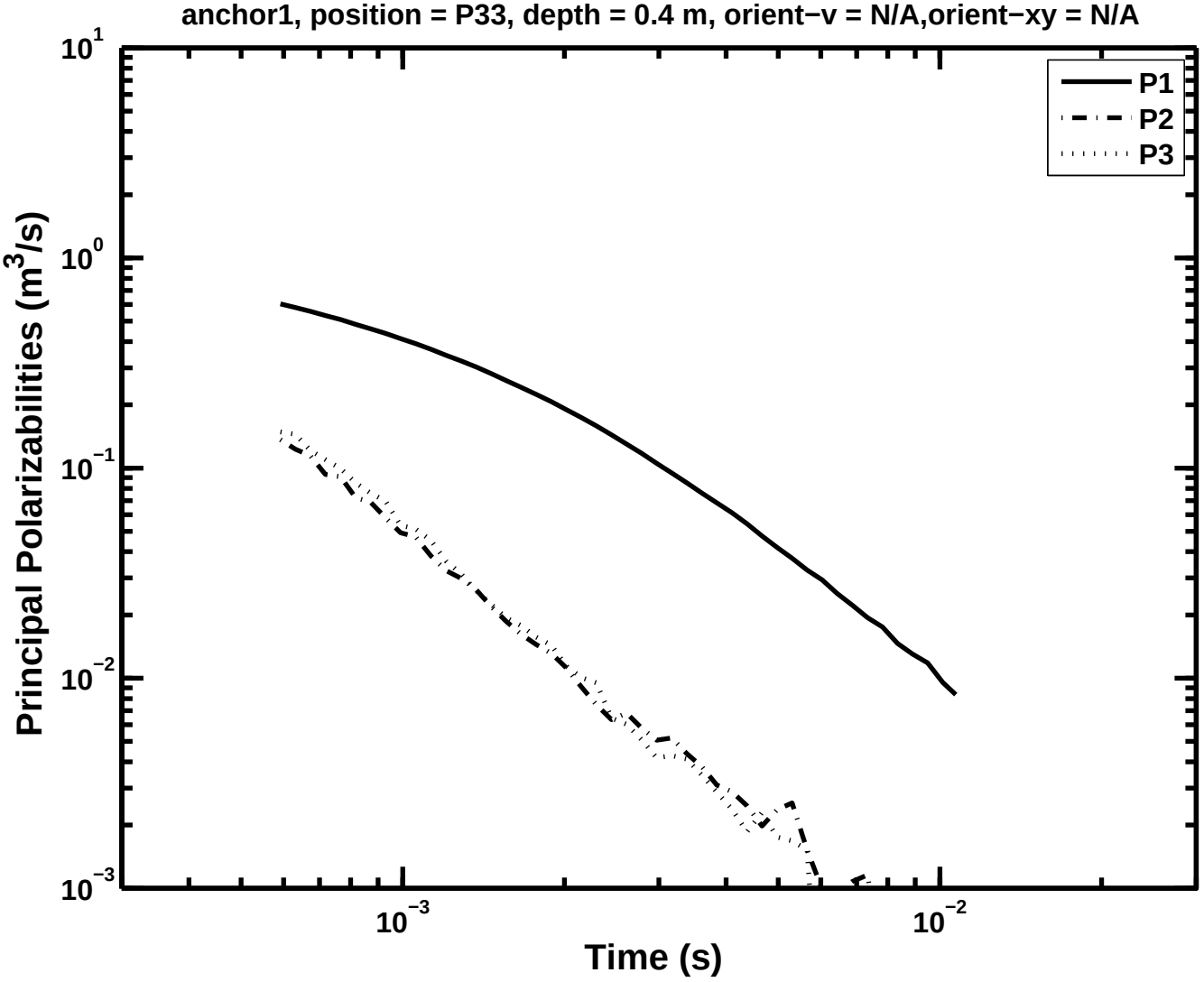

Figure A1−3: Principal polarizabilities as a function of time − anchor1−r2, position = P33, depth = 0.4 m, orient−v = N/A,orient−xy = N/A

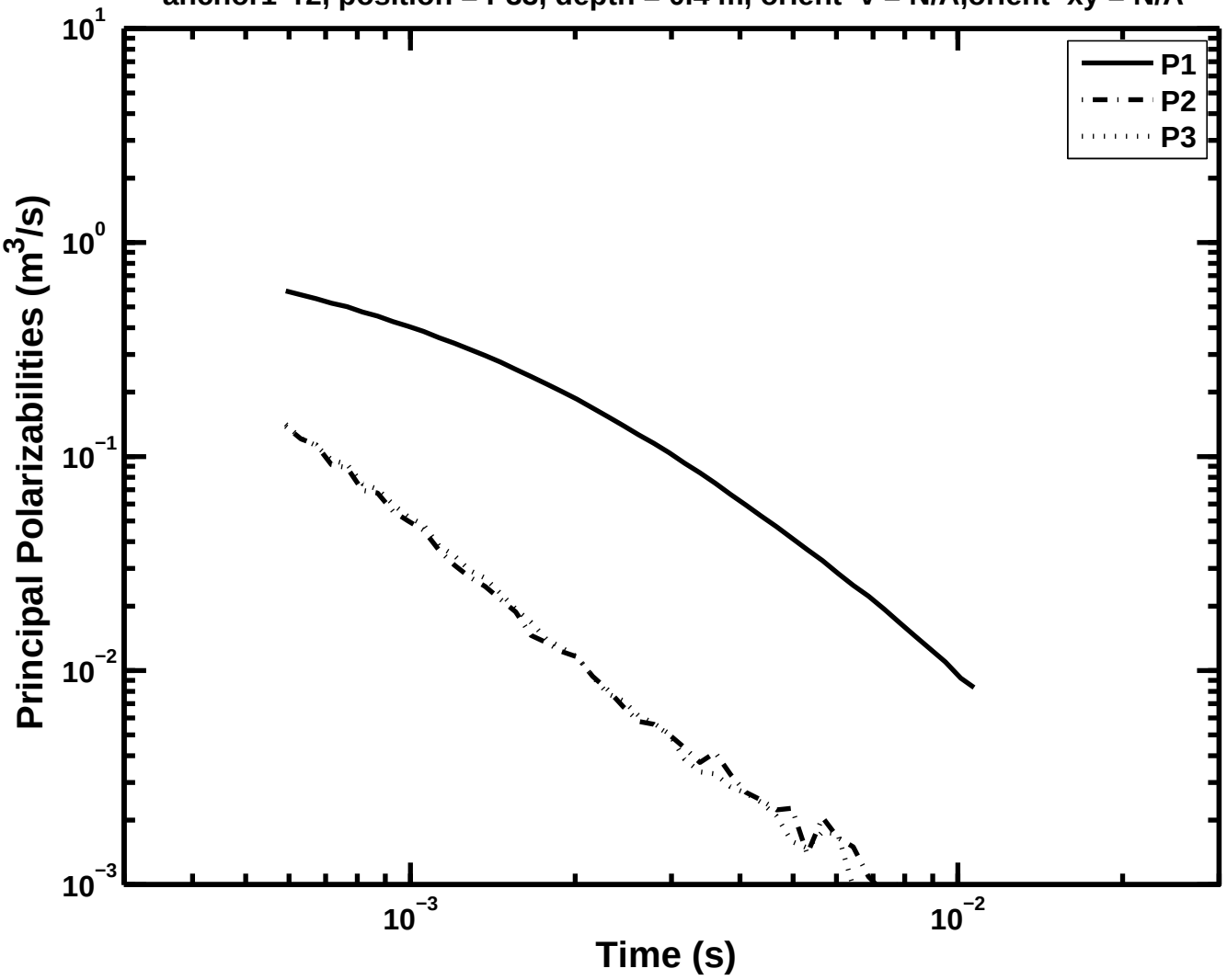

Figure A1−4: Principal polarizabilities as a function of time − anchor1−r3, position = P33, depth = 0.4 m, orient−v = N/A,orient−xy = N/A

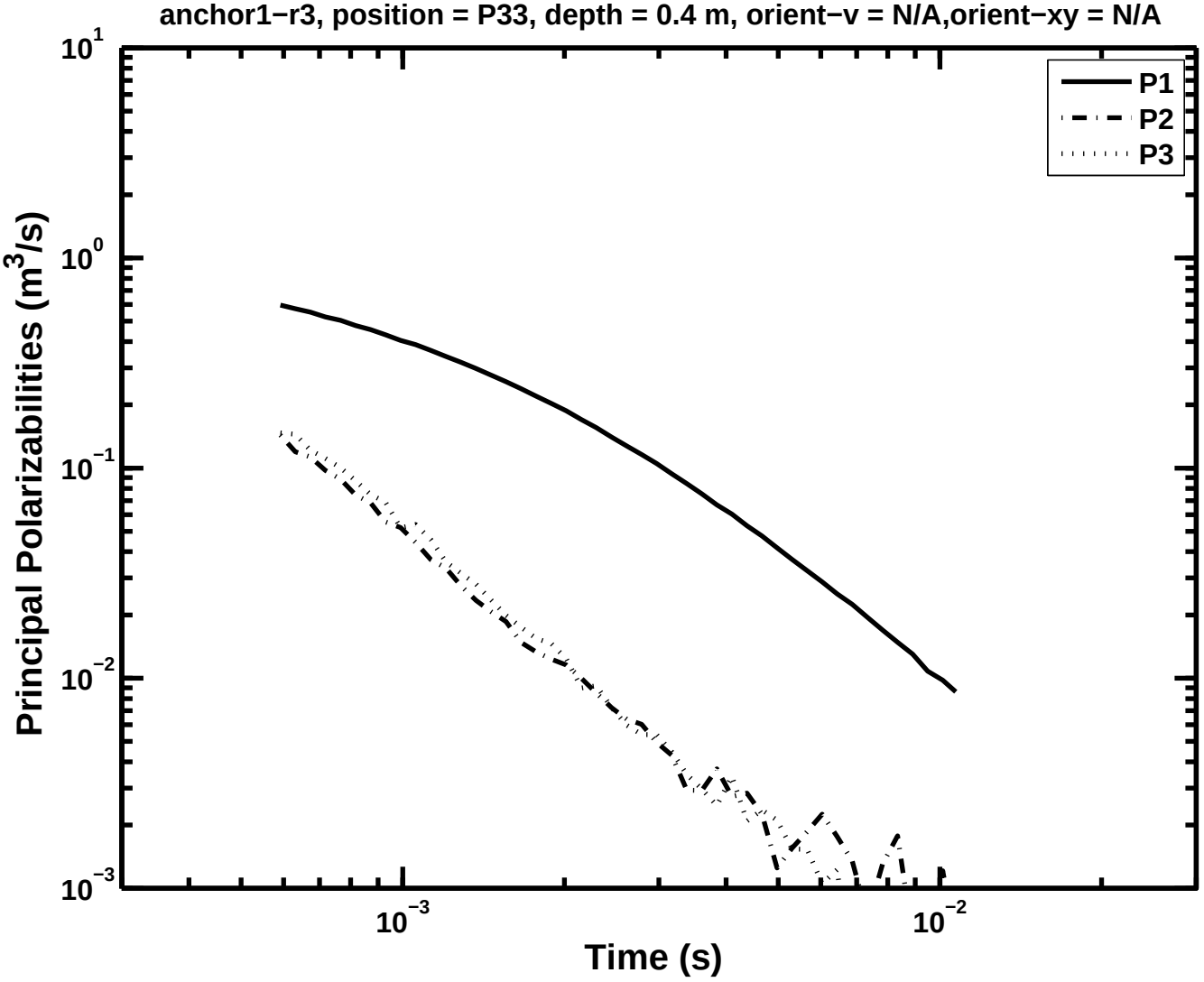

Figure A1−5: Principal polarizabilities as a function of time − chain, position = P3, depth = 0.4 m, orient−v = N/A,orient−xy = N/A

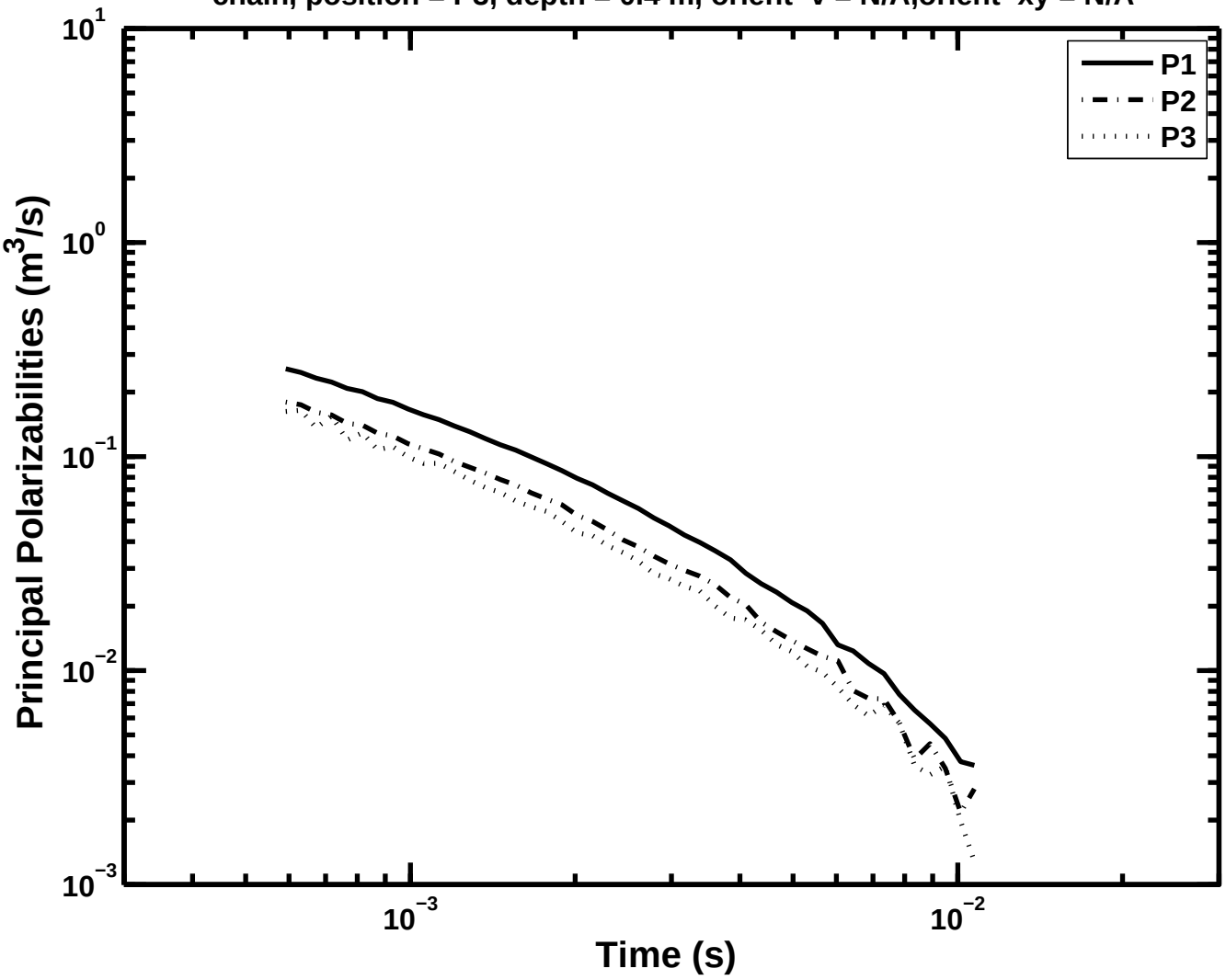

Figure A1−6: Principal polarizabilities as a function of time − propeller−lg, position = P1, depth = 0.7 m, orient−v = N/A,orient−xy = N/A

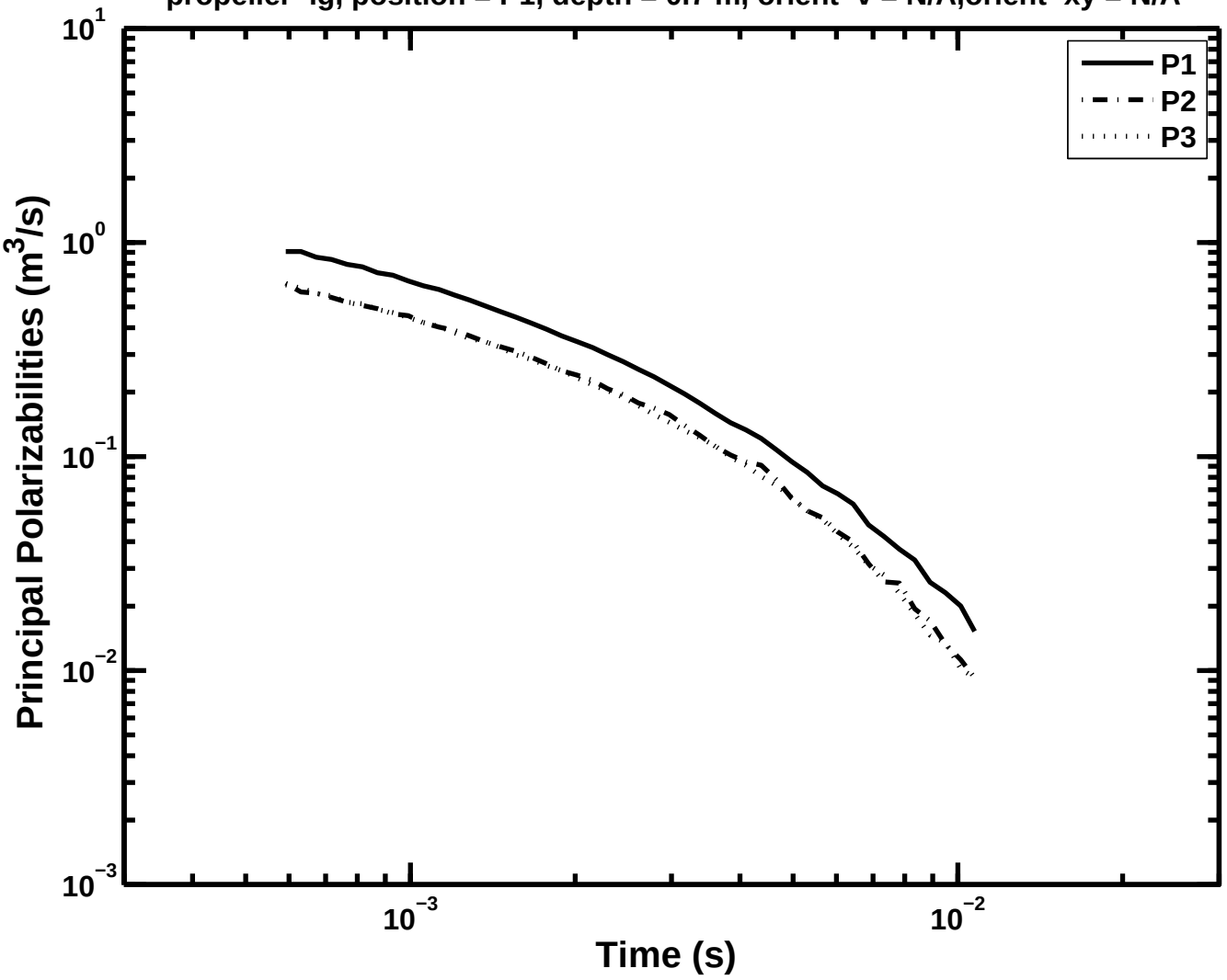

Figure A1−7: Principal polarizabilities as a function of time − propeller−lg, position = P3, depth = 0.7 m, orient−v = N/A,orient−xy = N/A

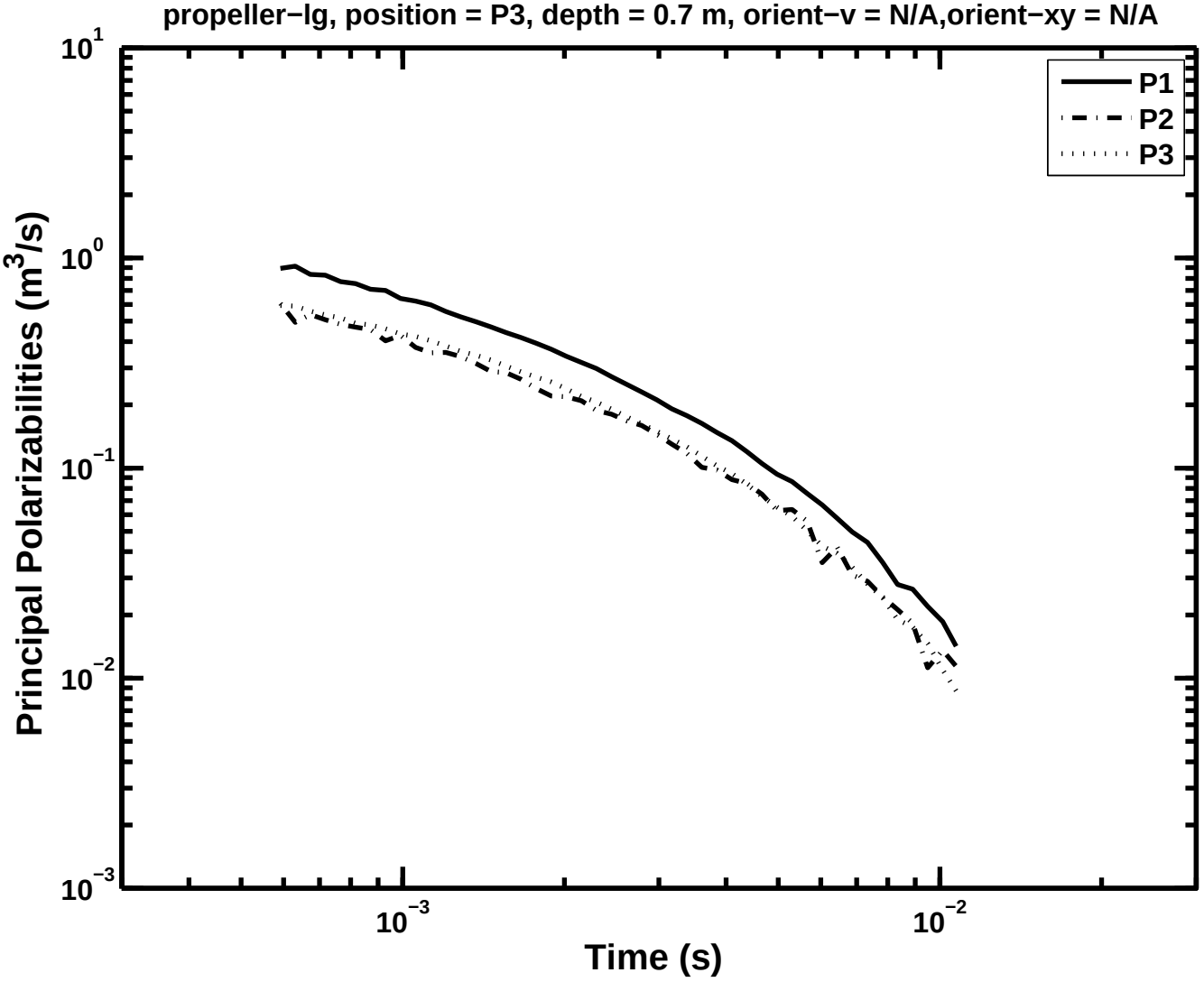

Figure A1−8: Principal polarizabilities as a function of time − propeller−lg, position = P1, depth = 0.4 m, orient−v = N/A,orient−xy = N/A

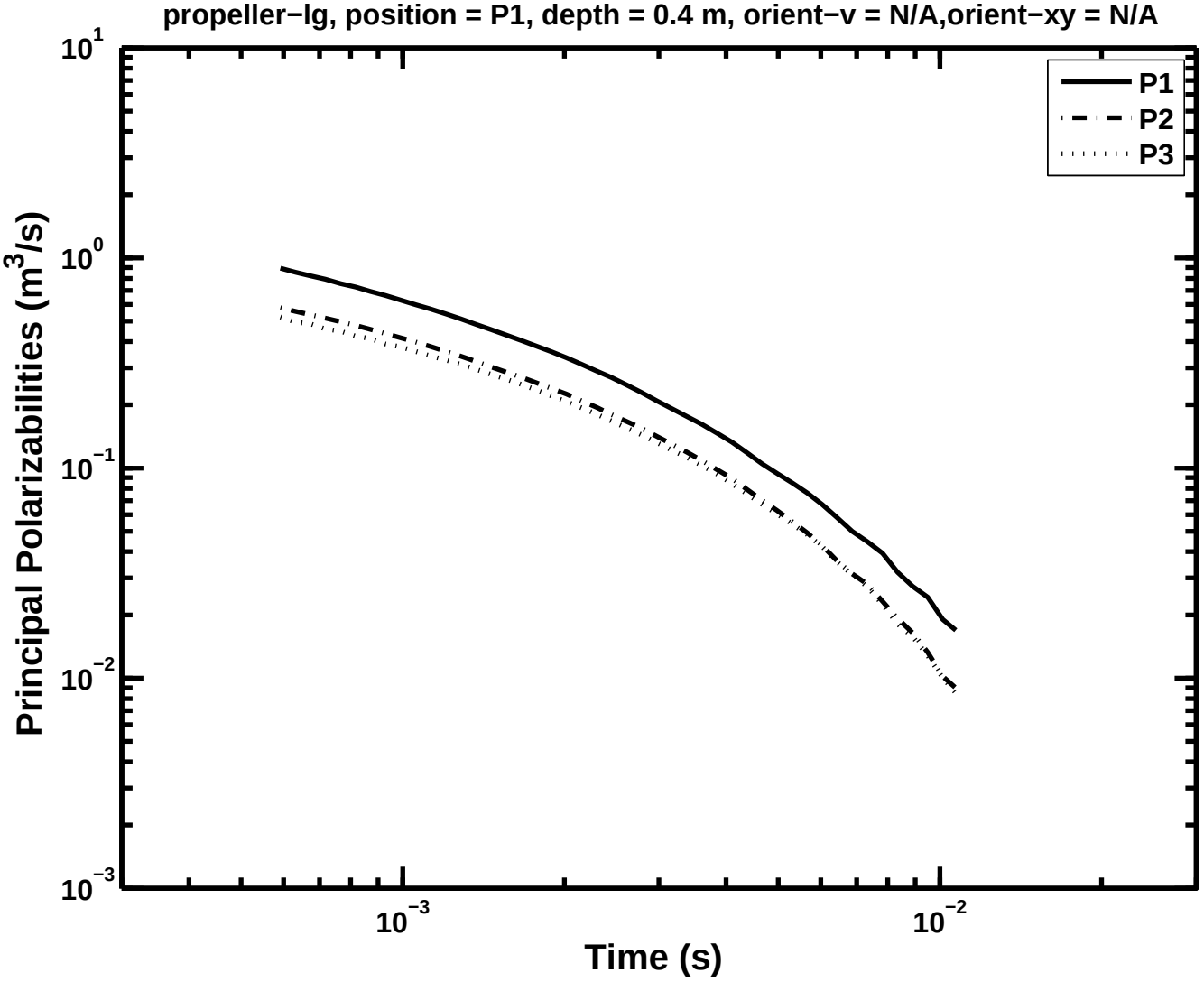

Figure A1−9: Principal polarizabilities as a function of time − propeller−lg, position = P3, depth = 0.4 m, orient−v = N/A,orient−xy = N/A

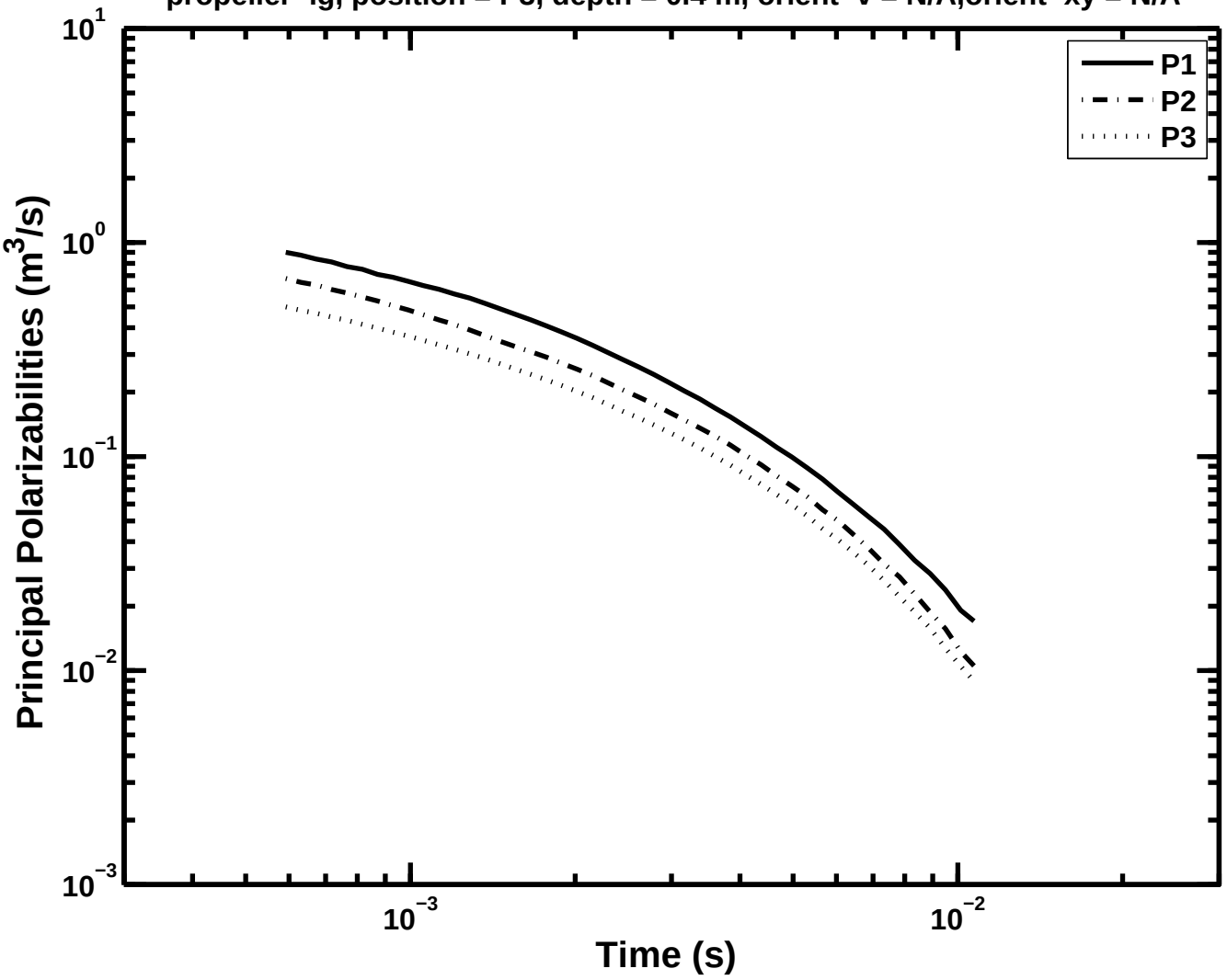

Figure A1−10: Principal polarizabilities as a function of time − propeller−sm, position = P1, depth = 0.4 m, orient−v = N/A,orient−xy = N/A

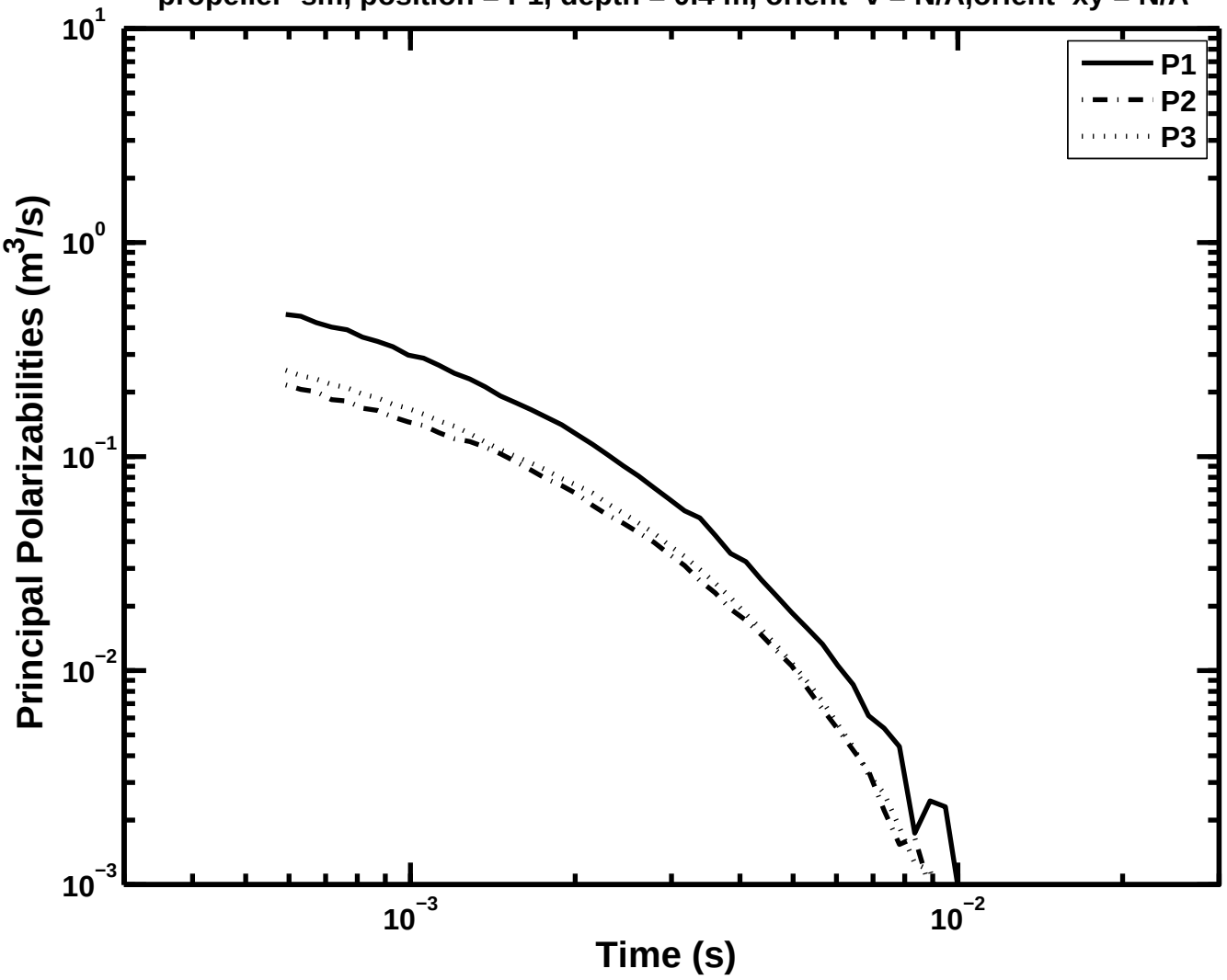

Figure A1−11: Principal polarizabilities as a function of time − propeller−sm, position = P3, depth = 0.4 m, orient−v = N/A,orient−xy = N/A

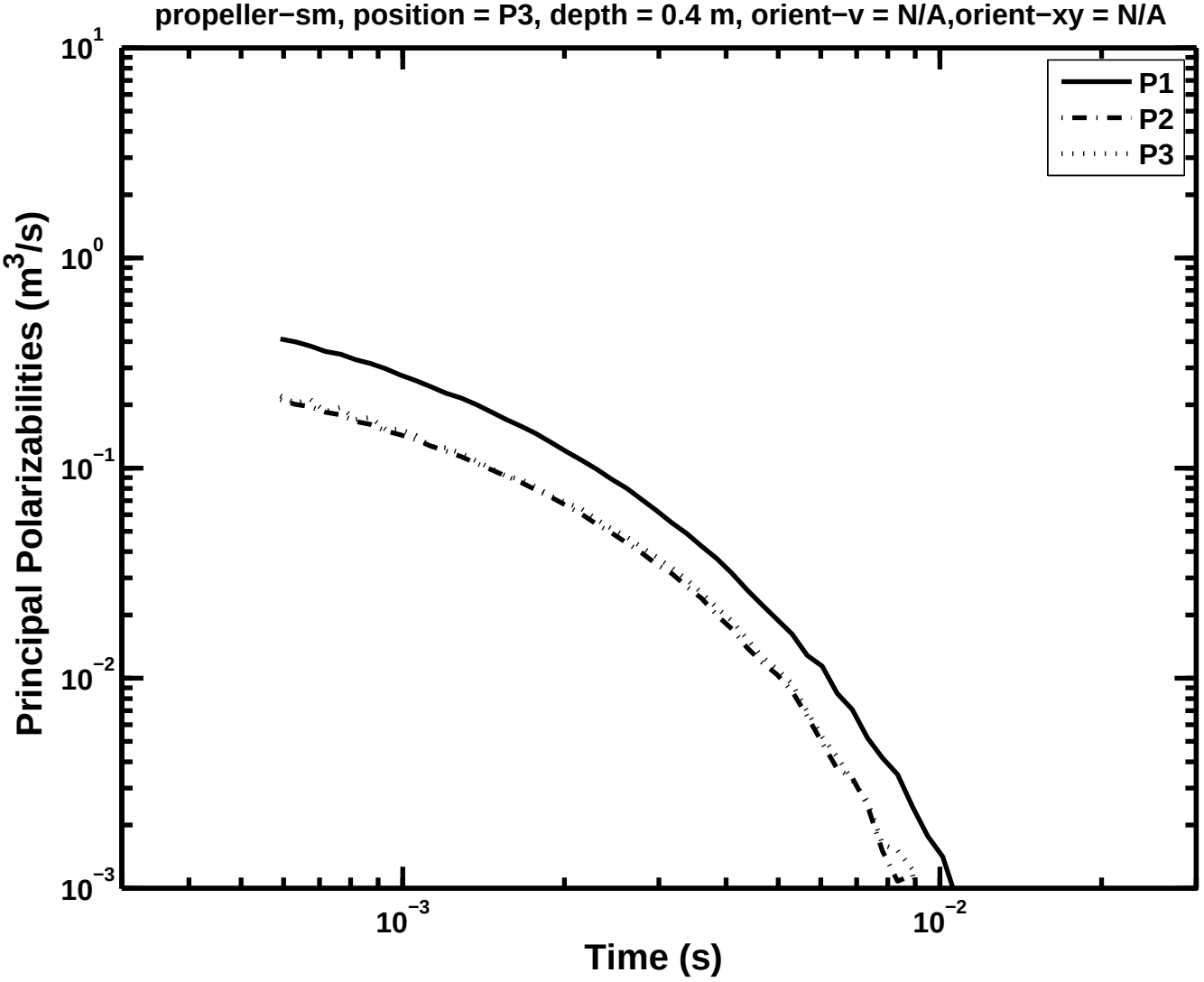

Figure A1−12: Principal polarizabilities as a function of time − scrap, position = P3, depth = 0.4 m, orient−v = N/A,orient−xy = N/A

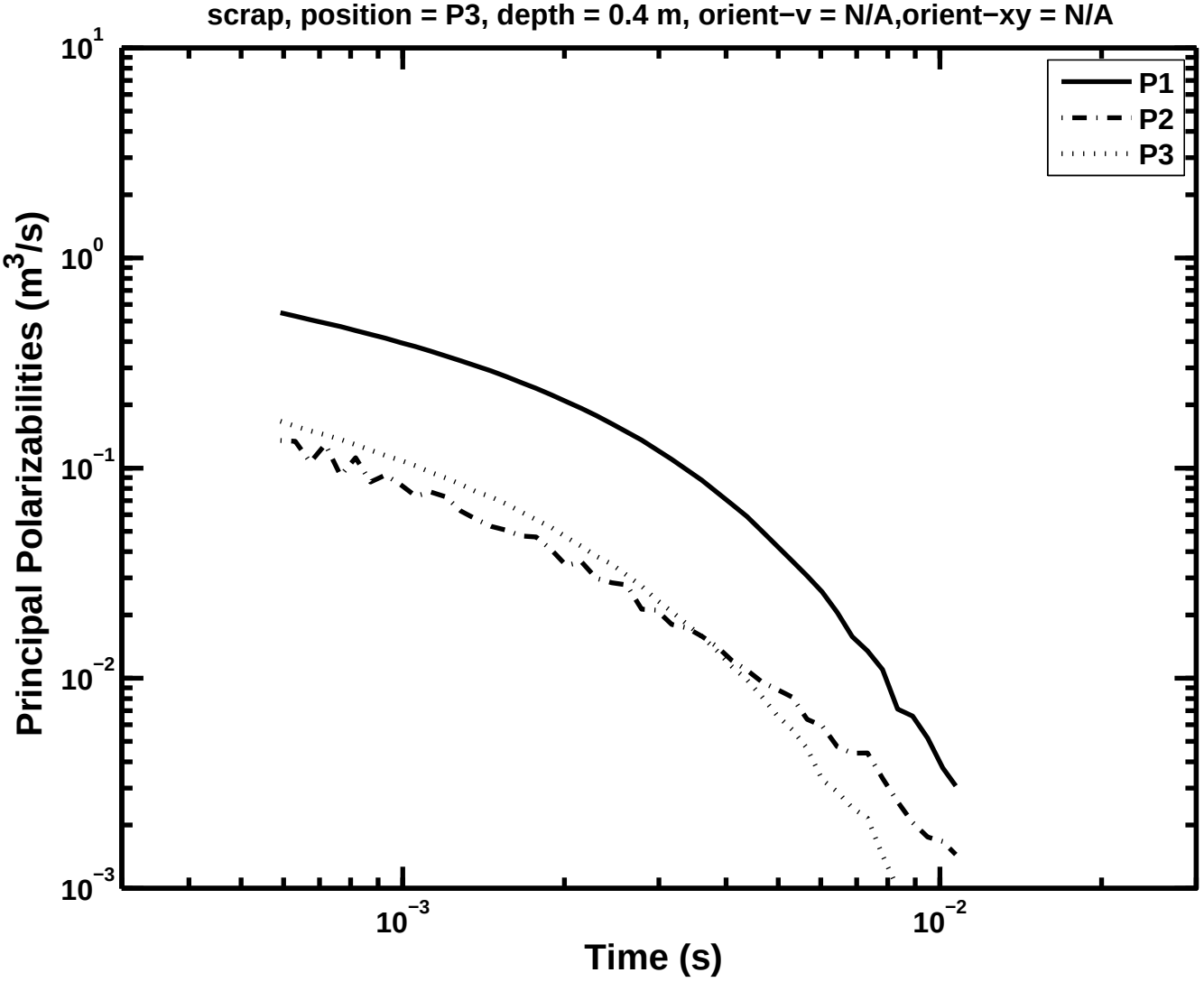

Figure A1−13: Principal polarizabilities as a function of time − 6−in shotput, position = P1, depth = 0.32 m, orient−v = N/A,orient−xy = N/A

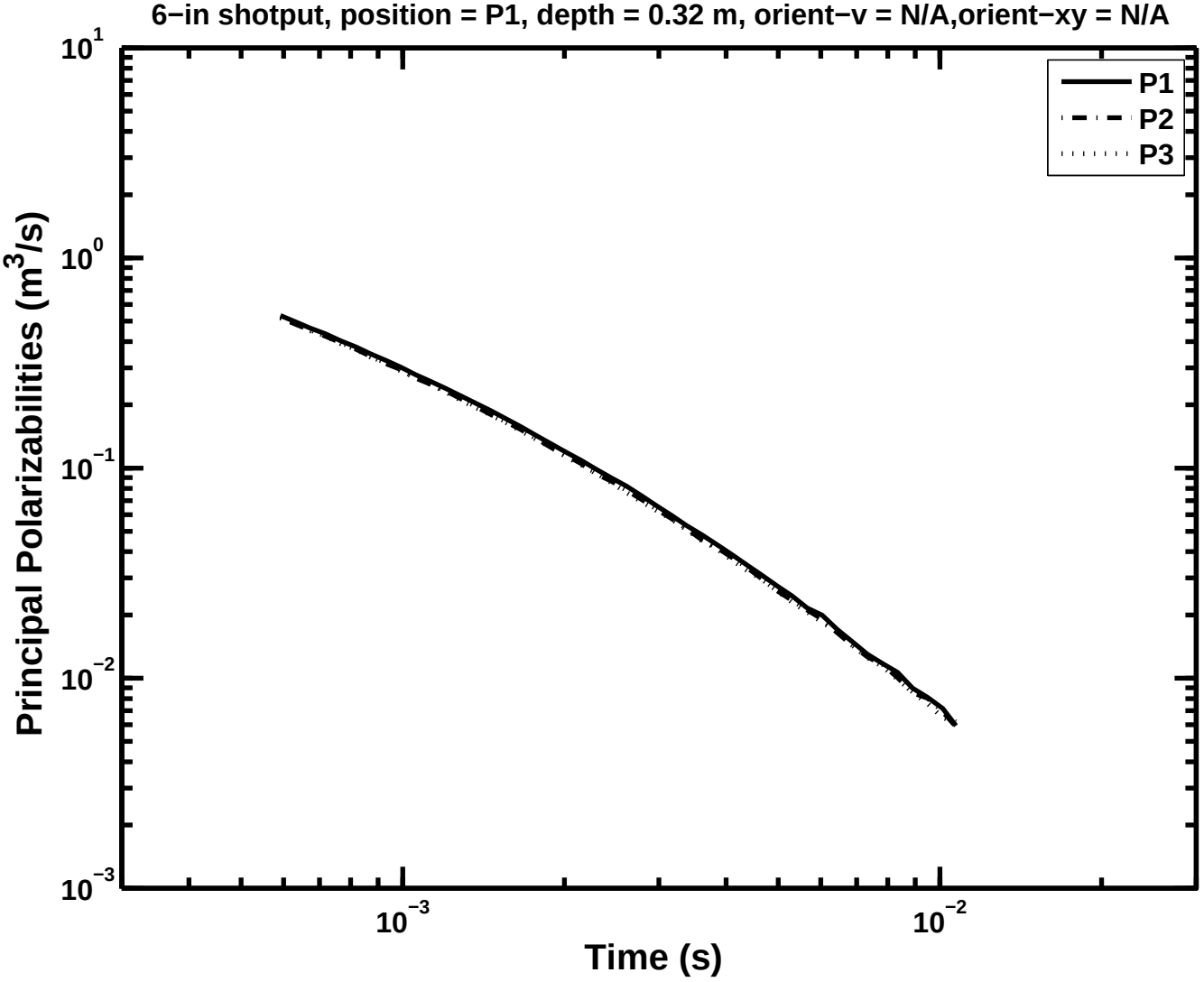

Figure A1−14: Principal polarizabilities as a function of time − 6−in shotput, position = P1, depth = 0.62 m, orient−v = N/A,orient−xy = N/A

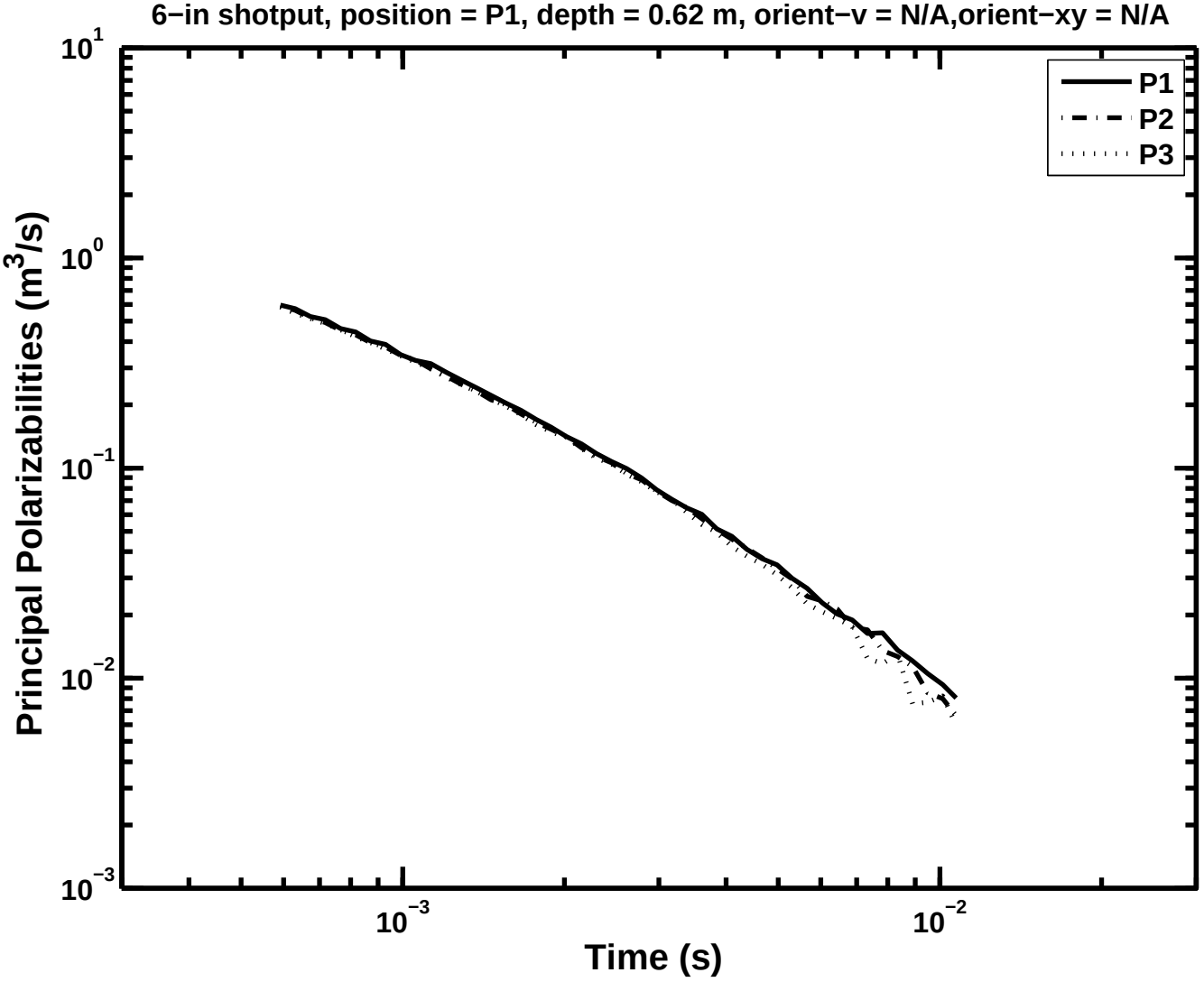

Figure A1−15: Principal polarizabilities as a function of time − 6−in shotput, position = P22, depth = 0.32 m, orient−v = N/A,orient−xy = N/A

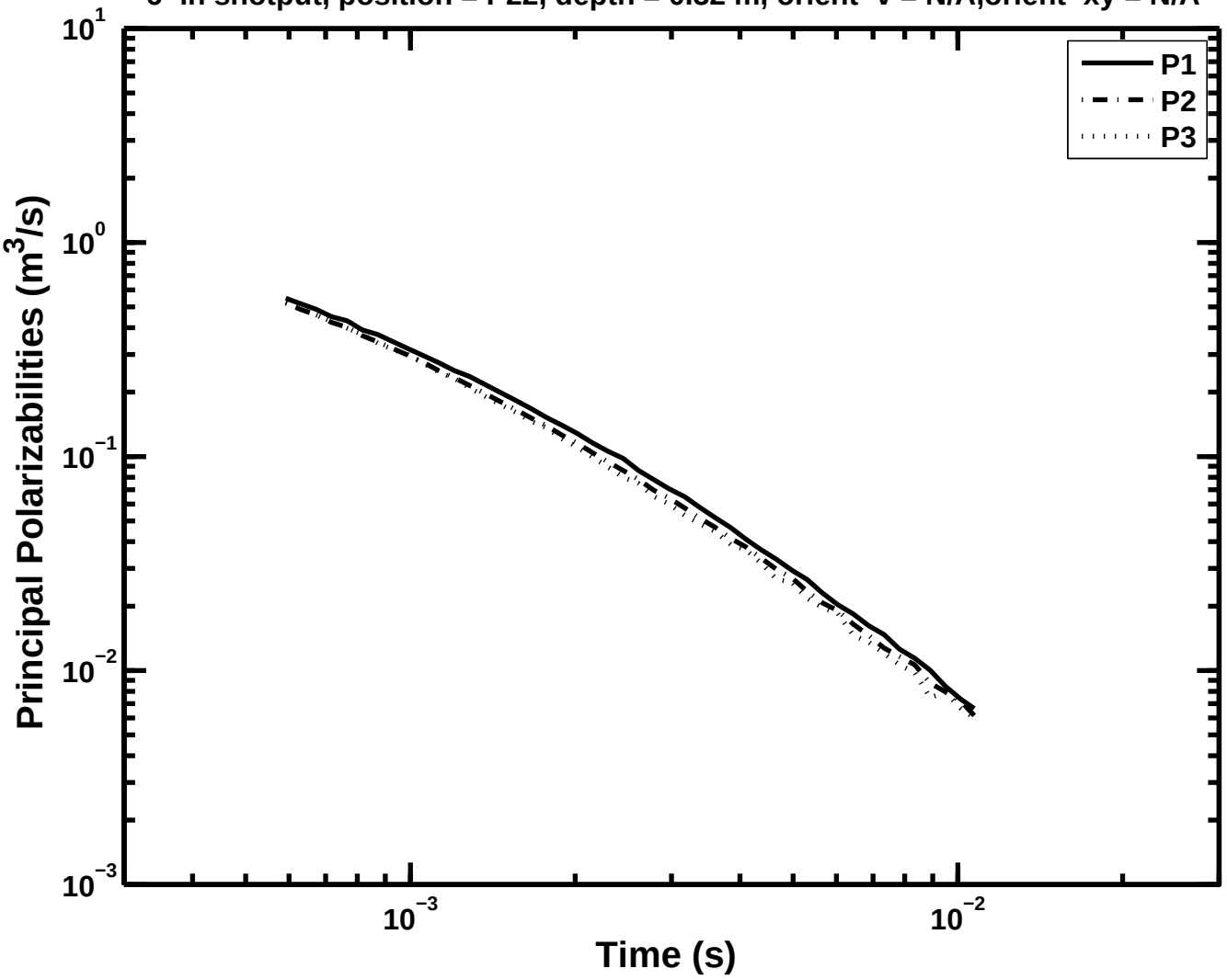

Figure A1−16: Principal polarizabilities as a function of time − 6−in shotput, position = P22, depth = 0.62 m, orient−v = N/A,orient−xy = N/A

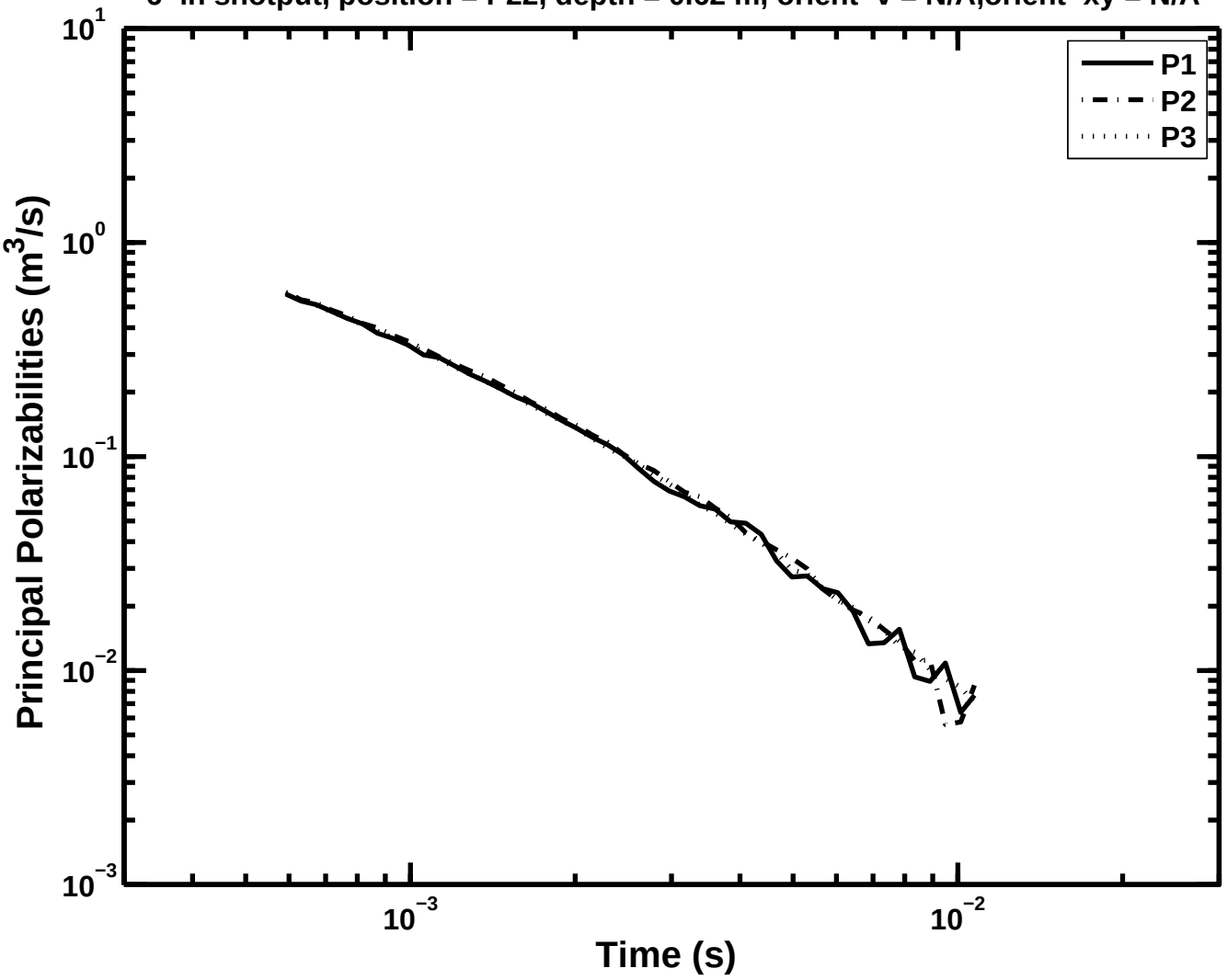

Figure A1−17: Principal polarizabilities as a function of time − 6−in shotput, position = P2, depth = 0.32 m, orient−v = N/A,orient−xy = N/A

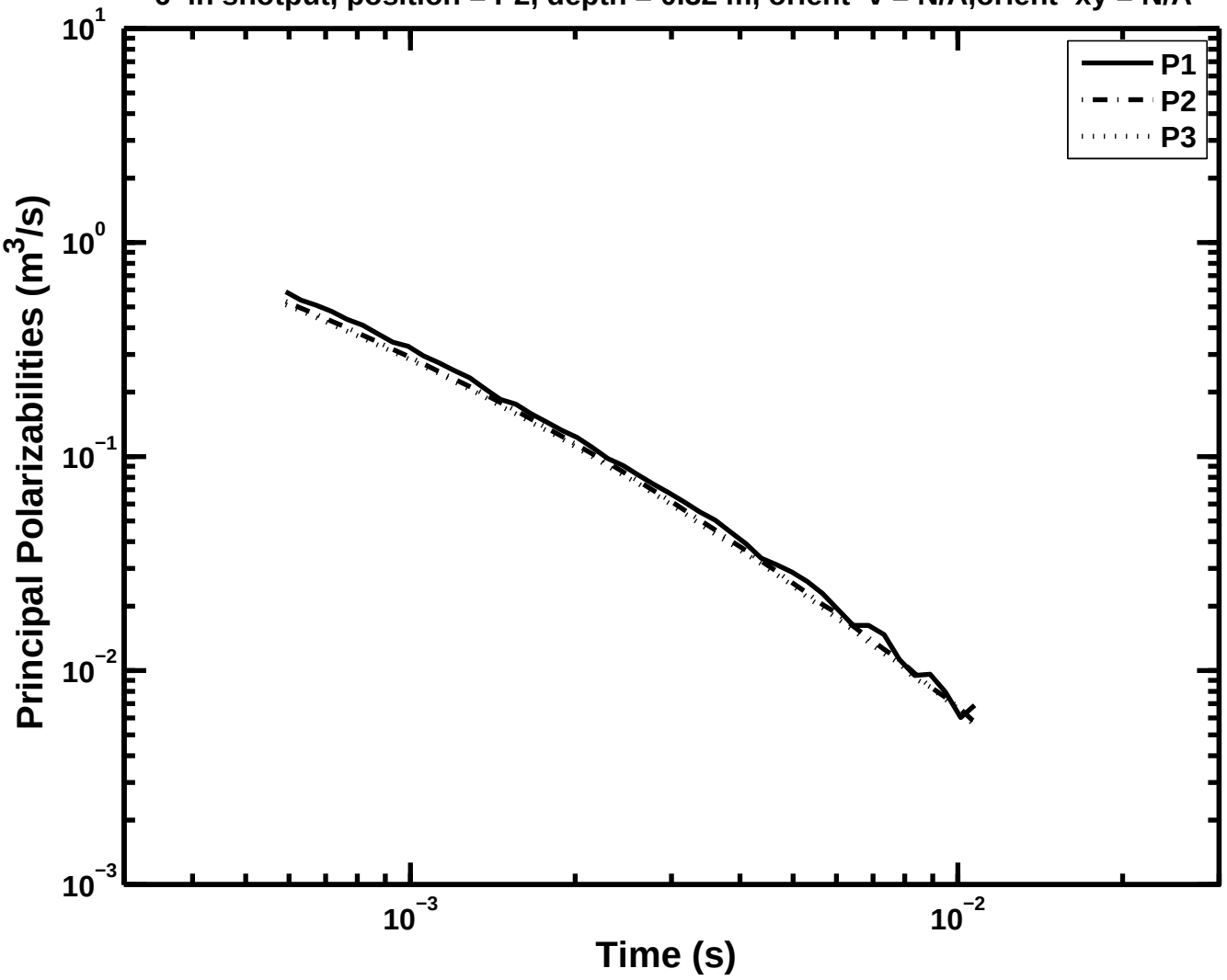

Figure A1−18: Principal polarizabilities as a function of time − 6−in shotput, position = P3, depth = 0.32 m, orient−v = N/A,orient−xy = N/A

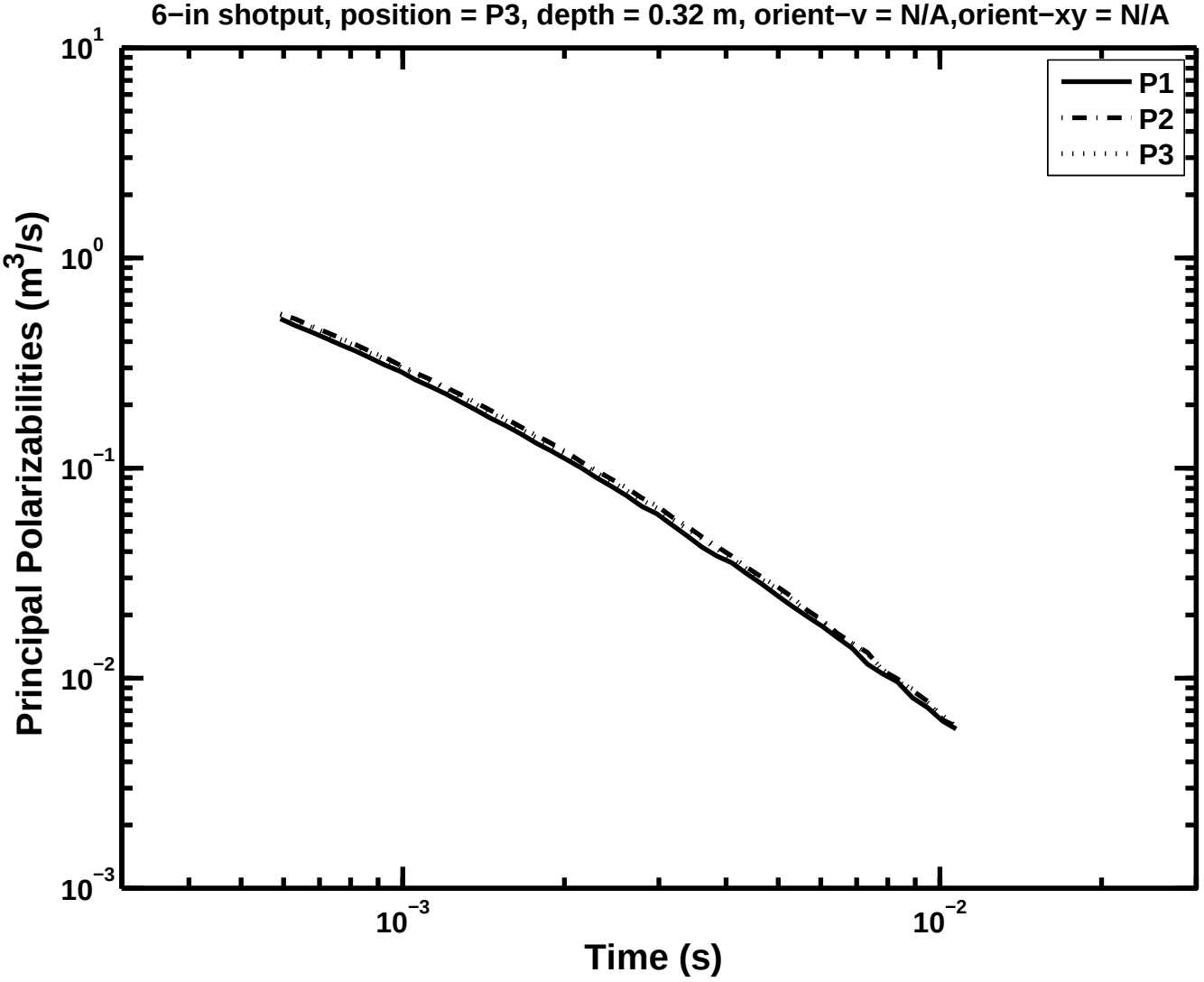

Figure A1−19: Principal polarizabilities as a function of time − 9−in steel spheroid, position = P1, depth = 0.4 m, orient−v = 90,orient−xy = 90

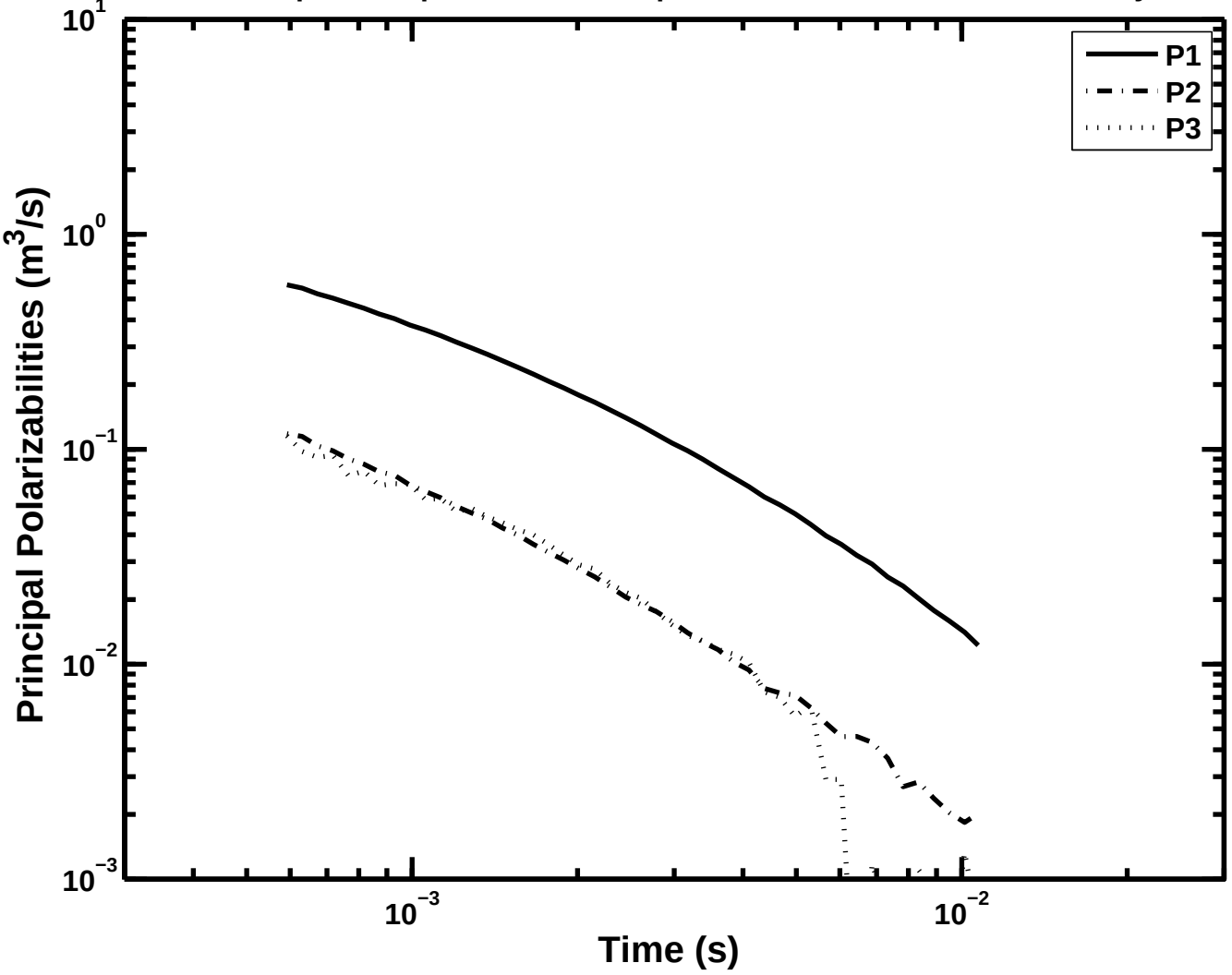

Figure A1−20: Principal polarizabilities as a function of time − 9−in steel spheroid, position = P2, depth = 0.4 m, orient−v = 90,orient−xy = 90

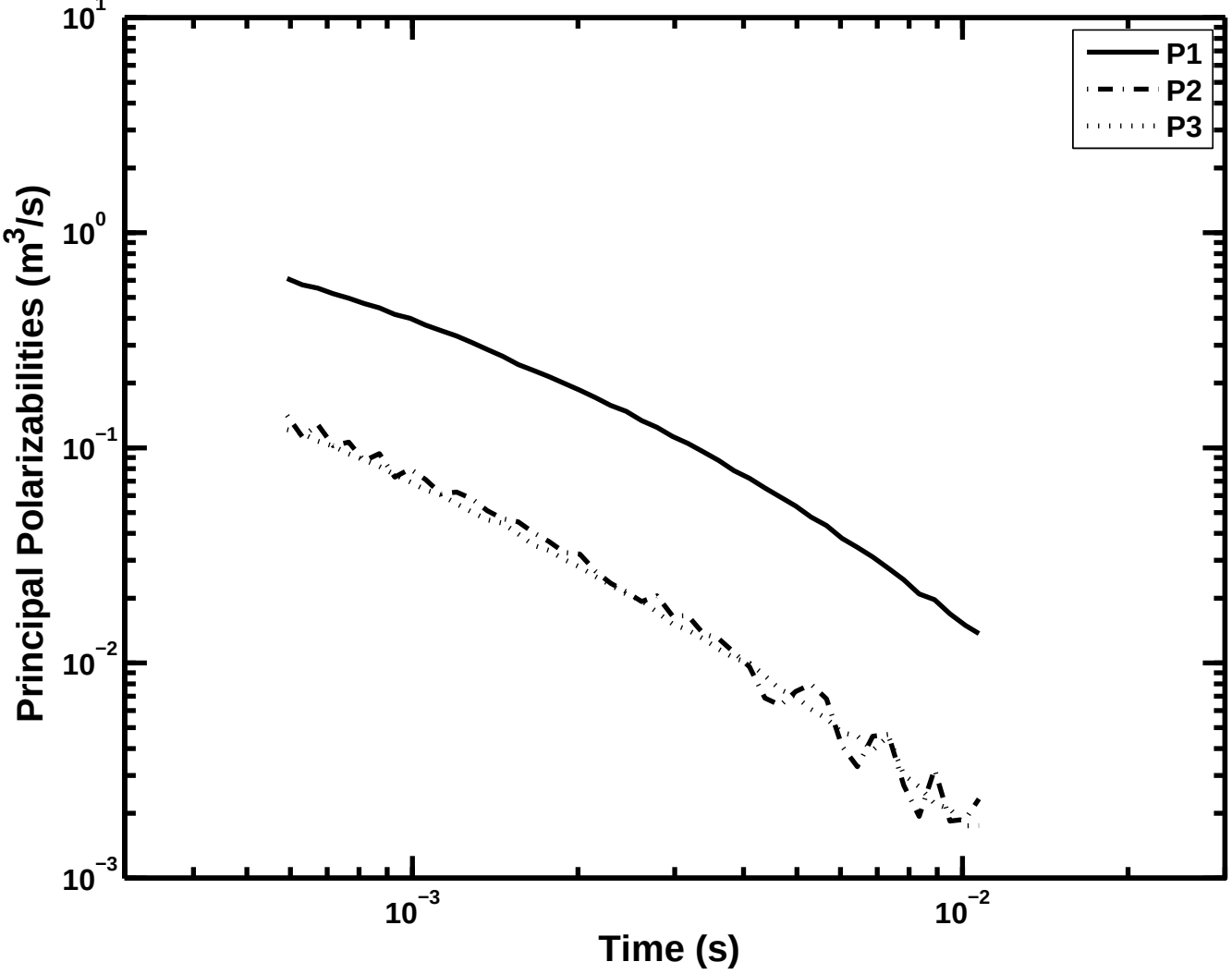

Figure A1−21: Principal polarizabilities as a function of time − 9−in steel spheroid, position = P3, depth = 0.4 m, orient−v = 90,orient−xy = 90

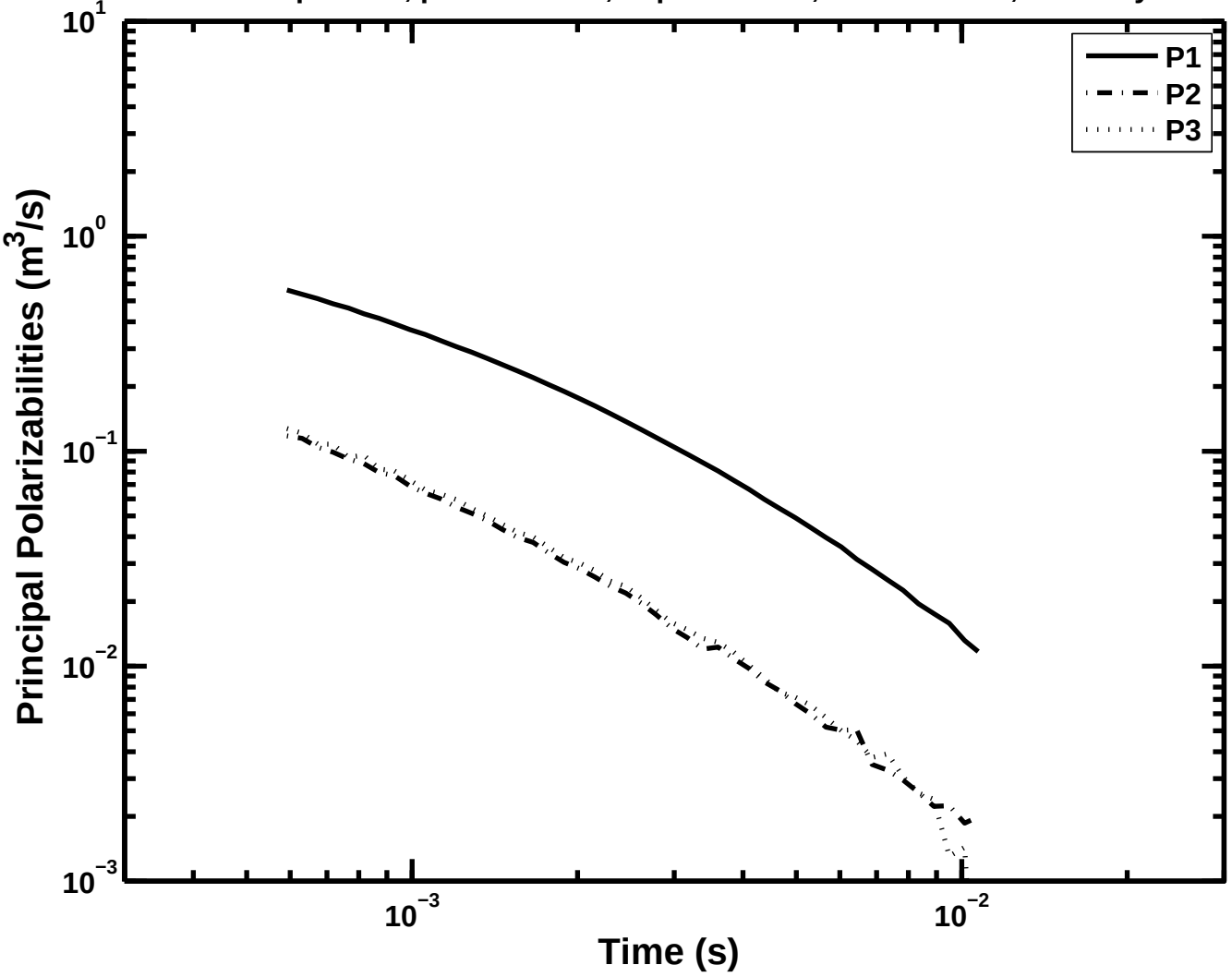

Figure A1−22: Principal polarizabilities as a function of time − 9−in steel spheroid, position = P3, depth = 0.2 m, orient−v = 90,orient−xy = 90

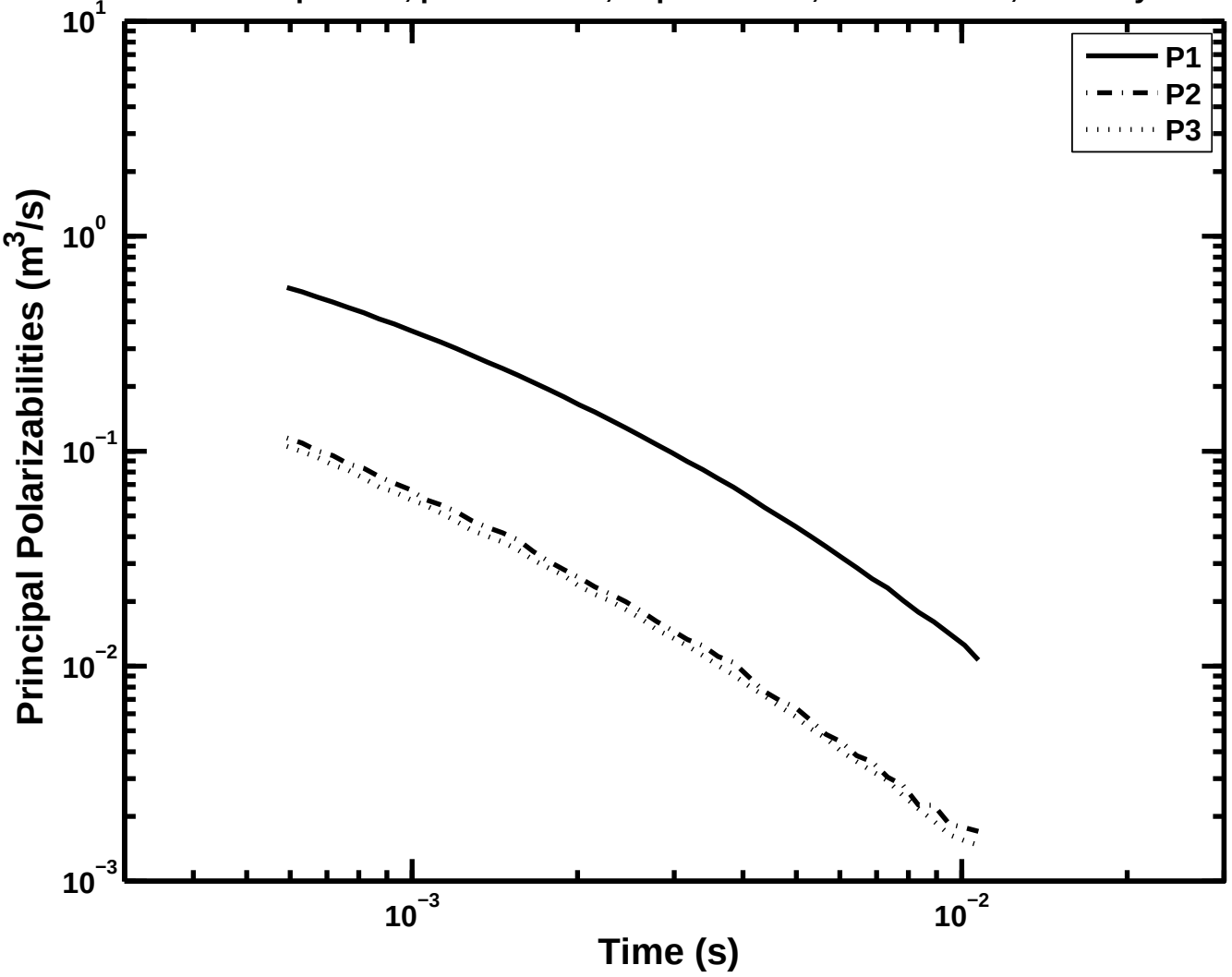

Figure A1−23: Principal polarizabilities as a function of time − 9−in steel spheroid, position = P3, depth = 0.2 m, orient−v = 90,orient−xy = 135

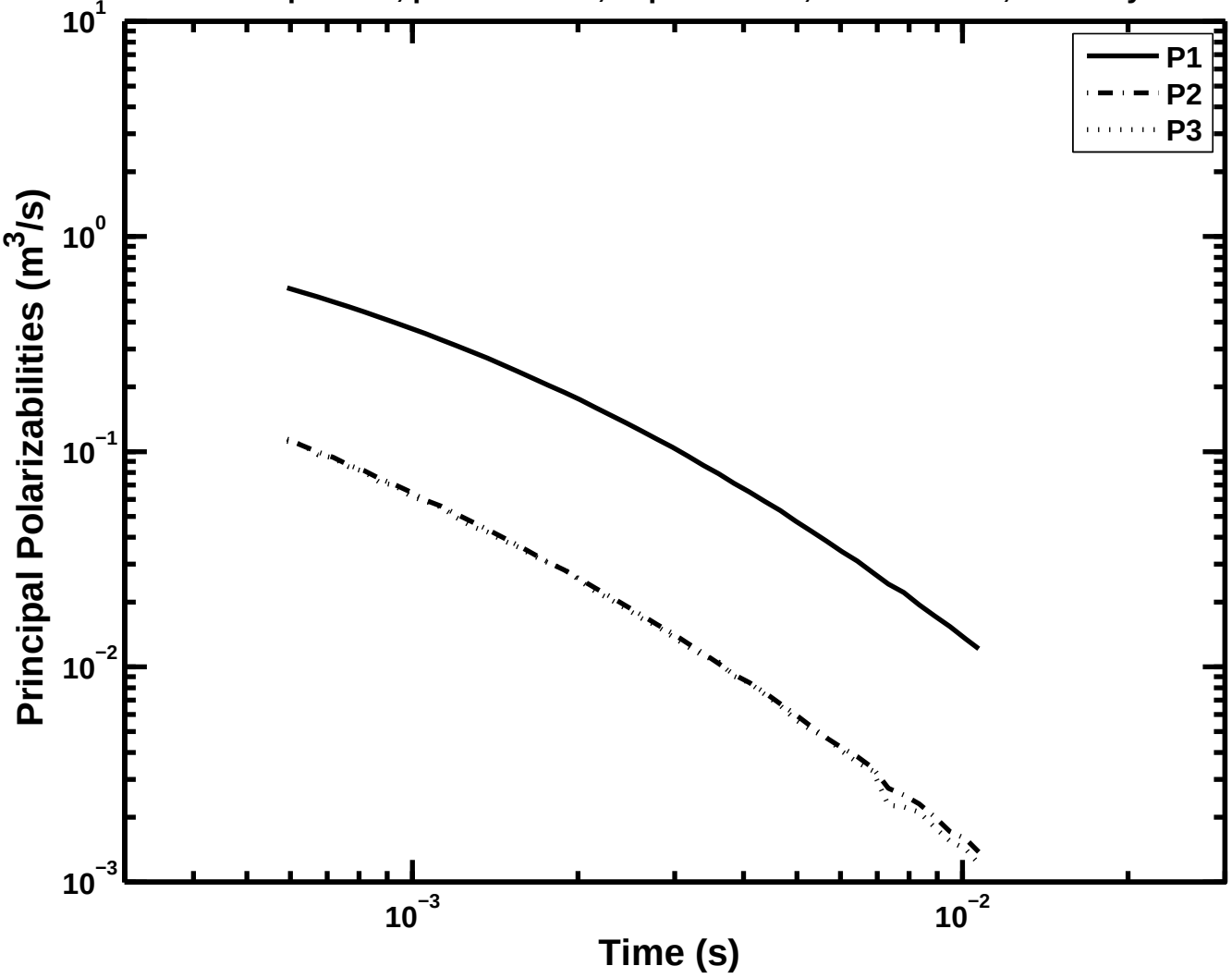

Figure A1−24: Principal polarizabilities as a function of time − 9−in steel spheroid, position = P3, depth = 0.2 m, orient−v = 90,orient−xy = 135

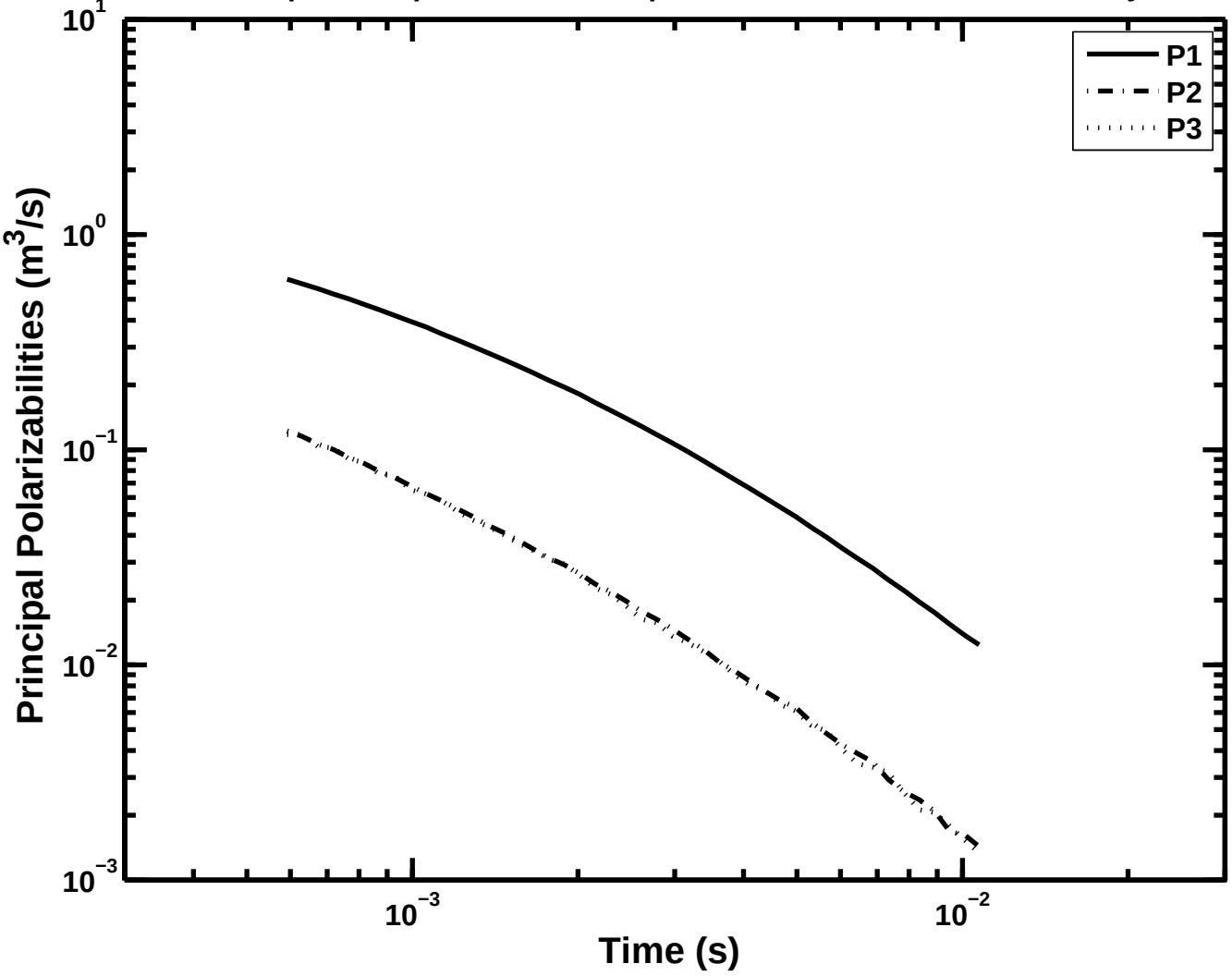

Figure A1−25: Principal polarizabilities as a function of time − 105−mm projectile, position = P1, depth = 0.35 m, orient−v = 90,orient−xy = 90

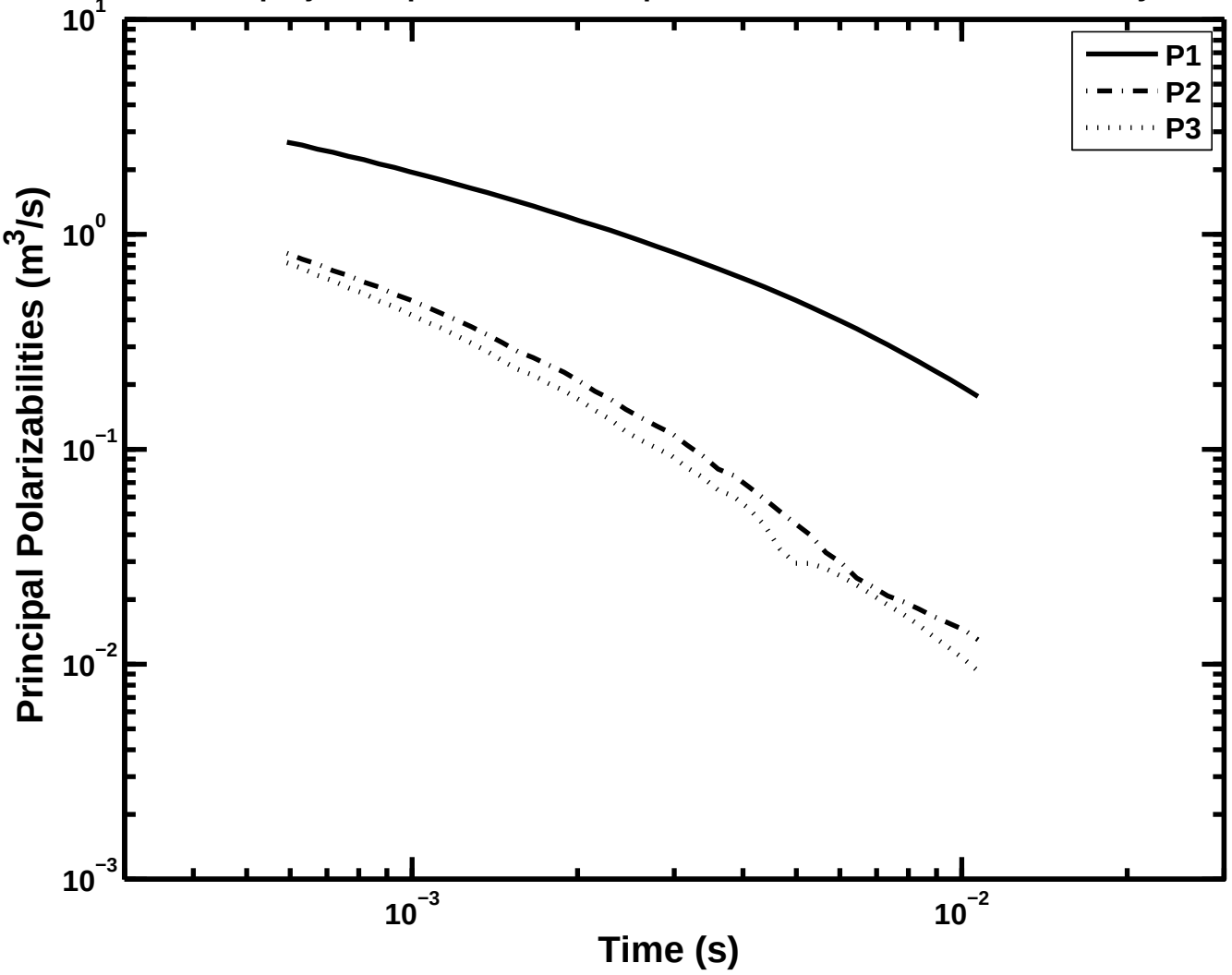

Figure A1−26: Principal polarizabilities as a function of time − 105−mm projectile, position = P1, depth = 0.65 m, orient−v = 90,orient−xy = 90

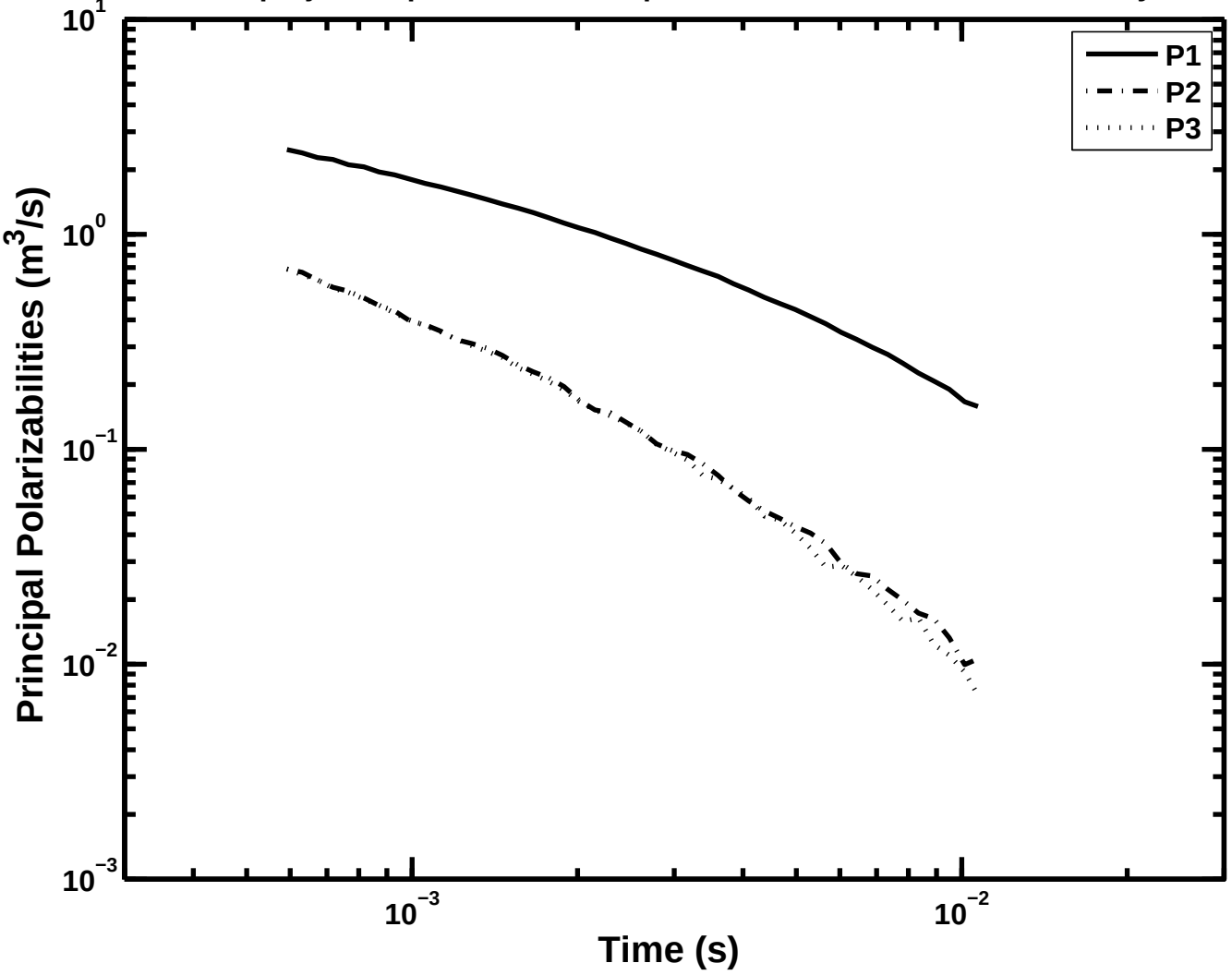

Figure A1−27: Principal polarizabilities as a function of time − 105−mm projectile, position = P22, depth = 0.4 m, orient−v = 0,orient−xy = N/A

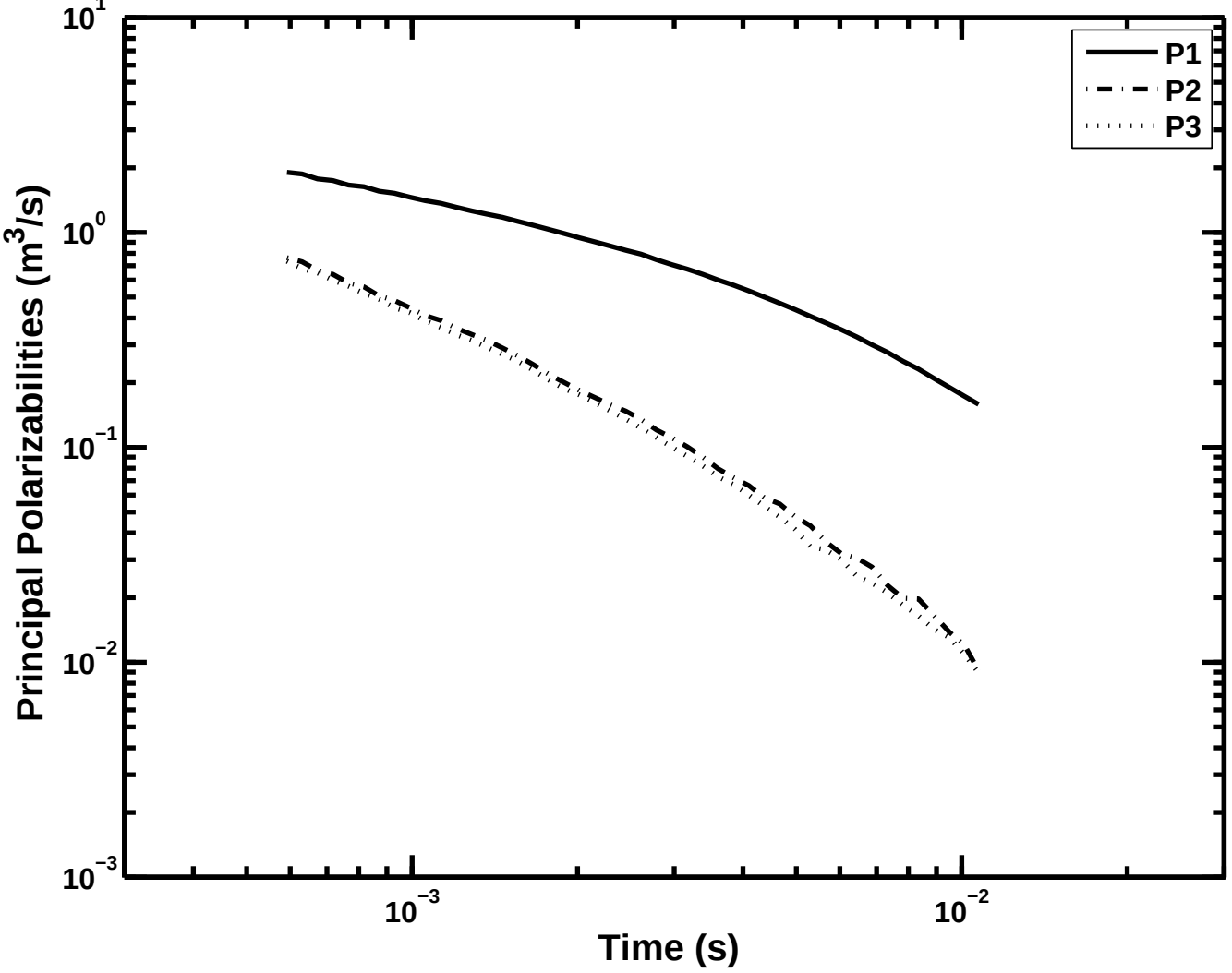

Figure A1−28: Principal polarizabilities as a function of time − 105−mm projectile, position = P22, depth = 0.7 m, orient−v = 0,orient−xy = N/A

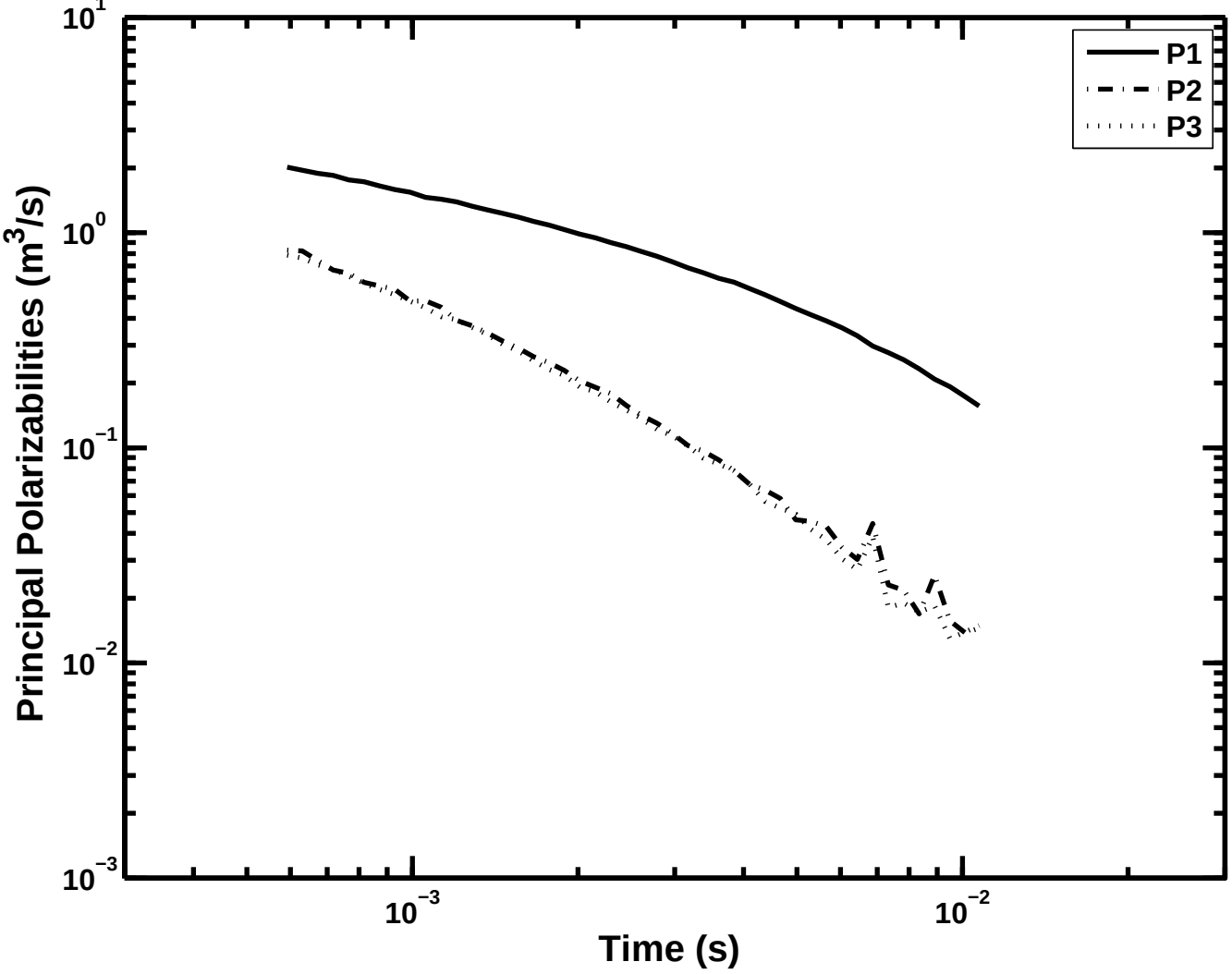

Figure A1−29: Principal polarizabilities as a function of time − 105−mm projectile, position = P2, depth = 0.35 m, orient−v = 90,orient−xy = 90

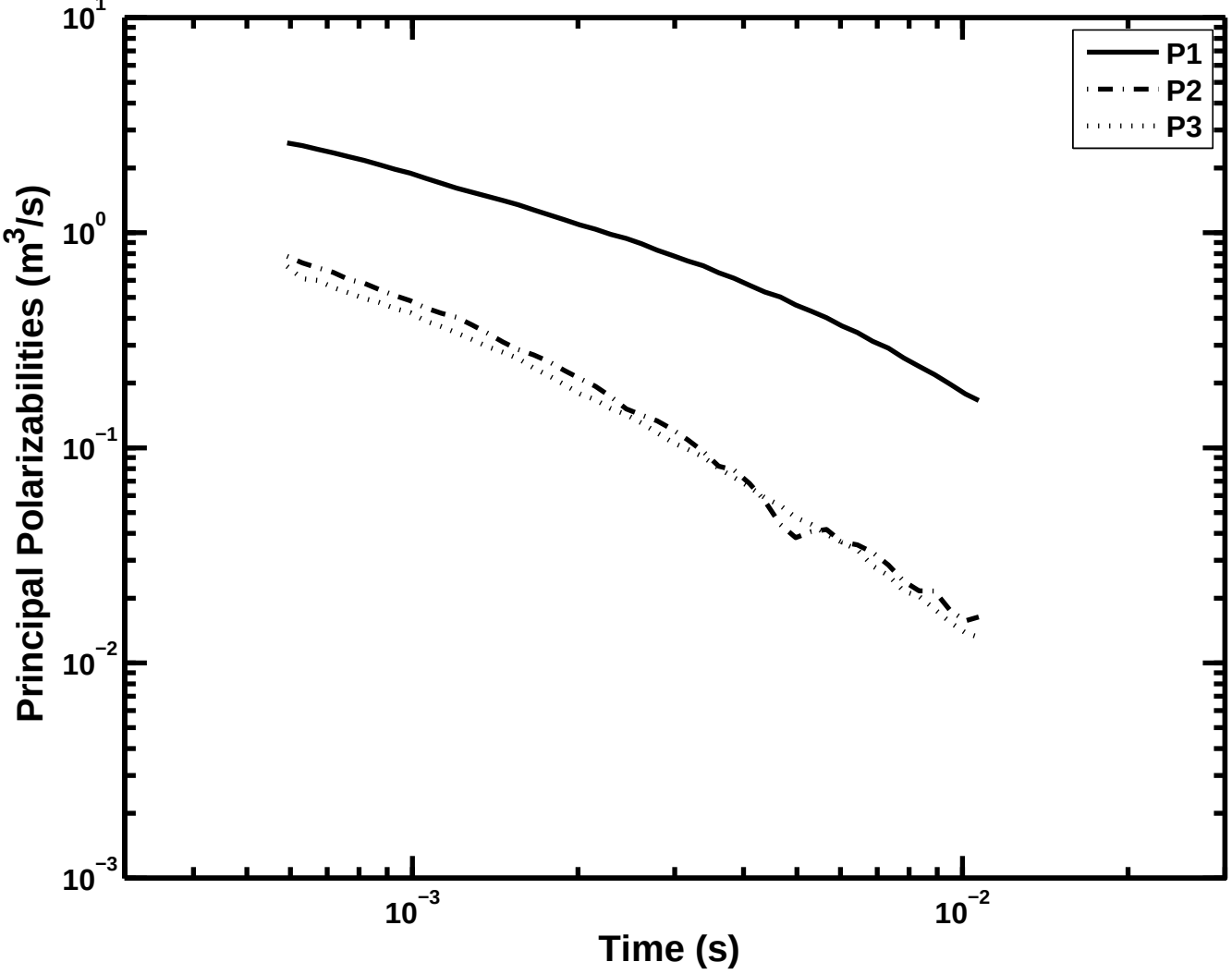

Figure A1−30: Principal polarizabilities as a function of time − 105−mm projectile, position = P2, depth = 0.65 m, orient−v = 90,orient−xy = 90

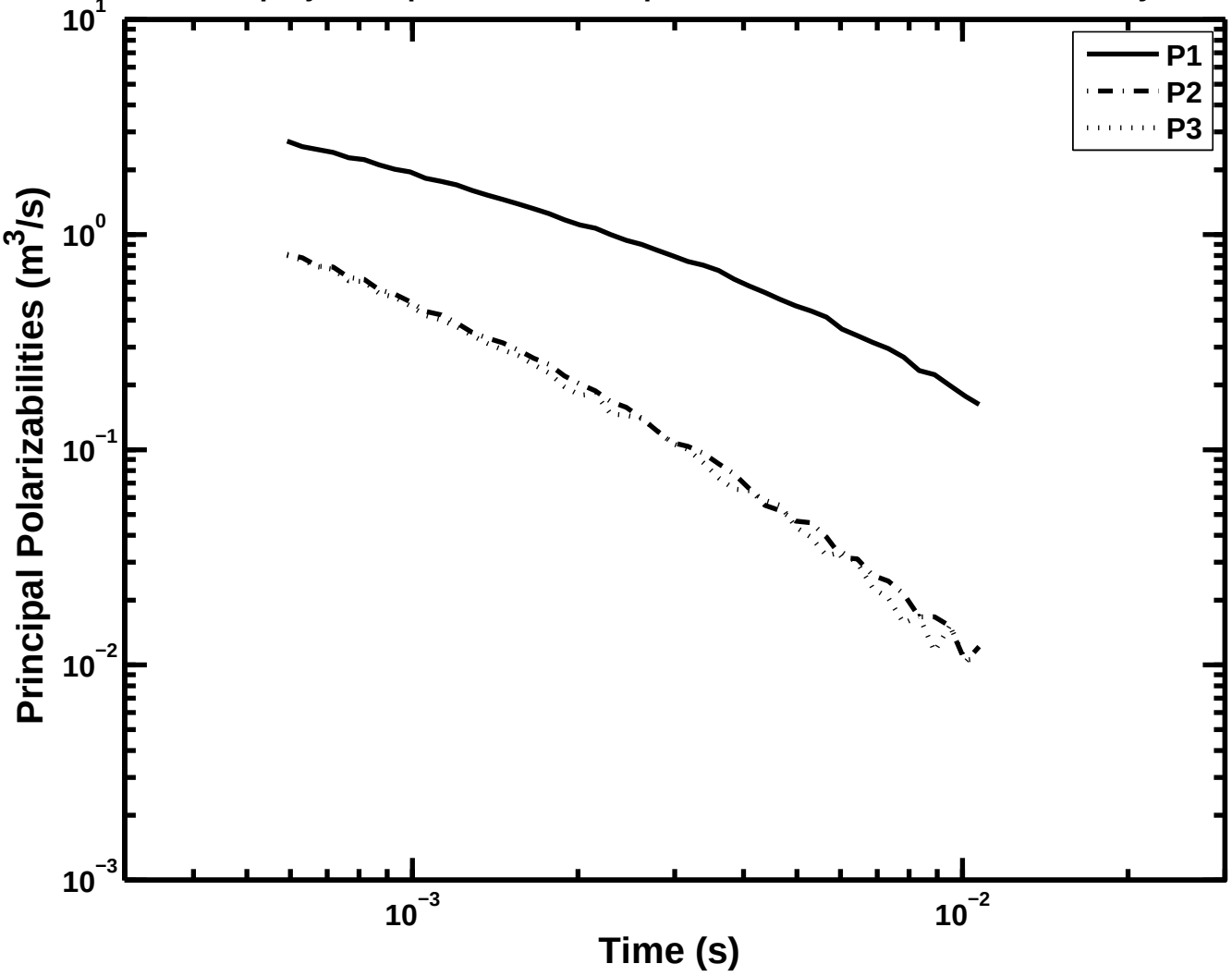

Figure A1−31: Principal polarizabilities as a function of time − 105−mm projectile, position = P3, depth = 0.35 m, orient−v = 90,orient−xy = 90

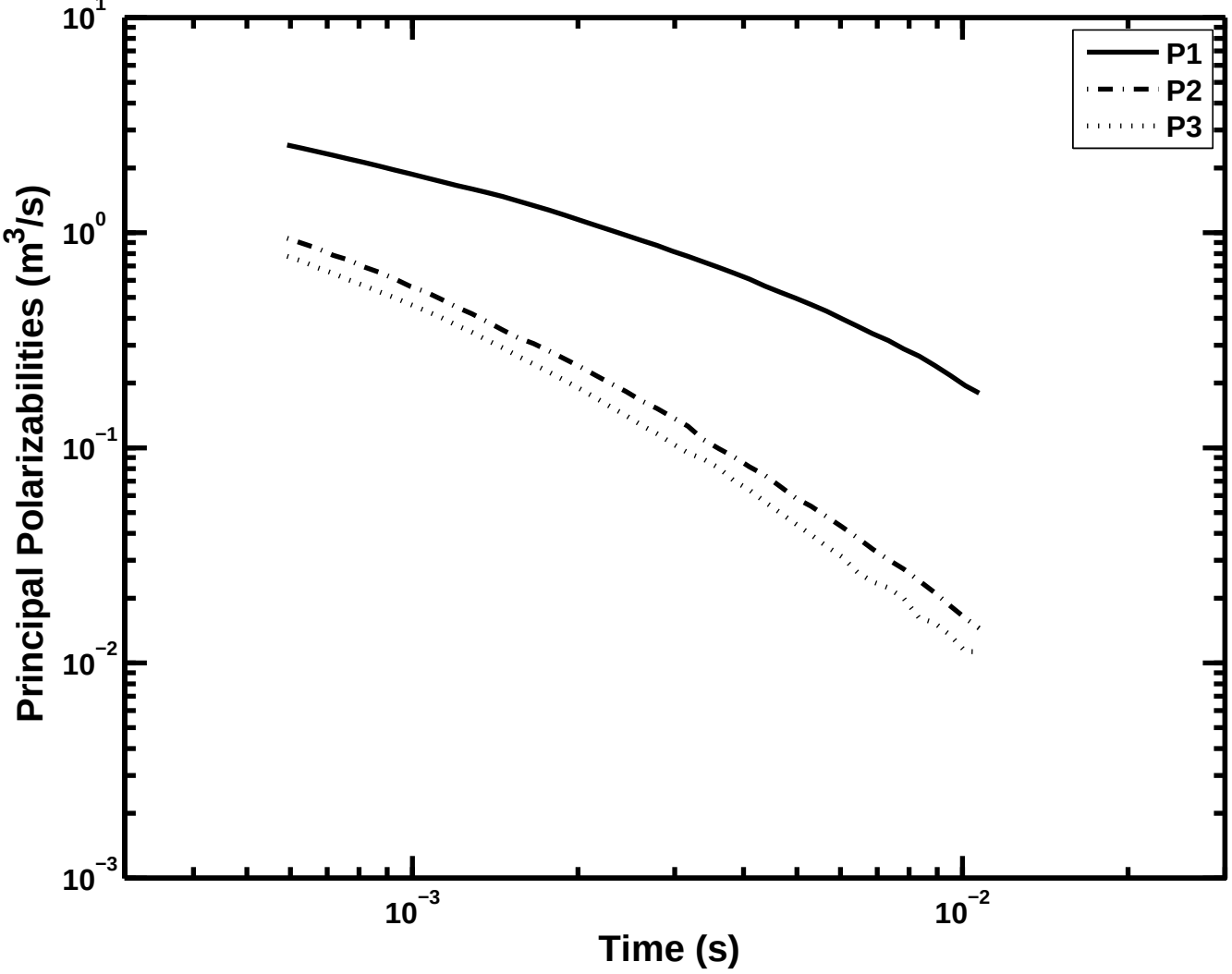

Figure A1−32: Principal polarizabilities as a function of time − 105−mm projectile, position = P3, depth = 0.95 m, orient−v = 90,orient−xy = 90

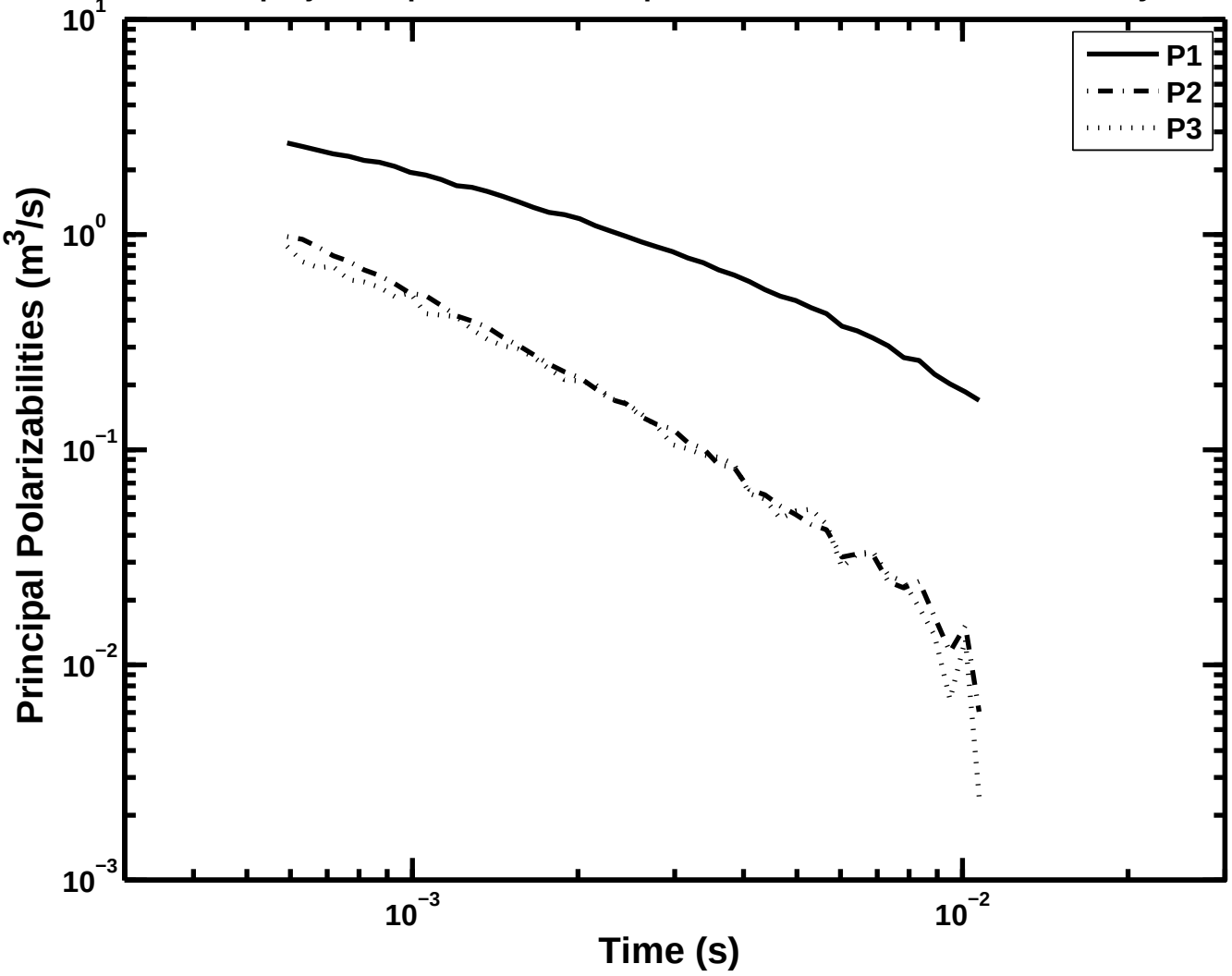

Figure A1−33: Principal polarizabilities as a function of time − 105−mm projectile, position = P3, depth = 0.65 m, orient−v = 90,orient−xy = 90

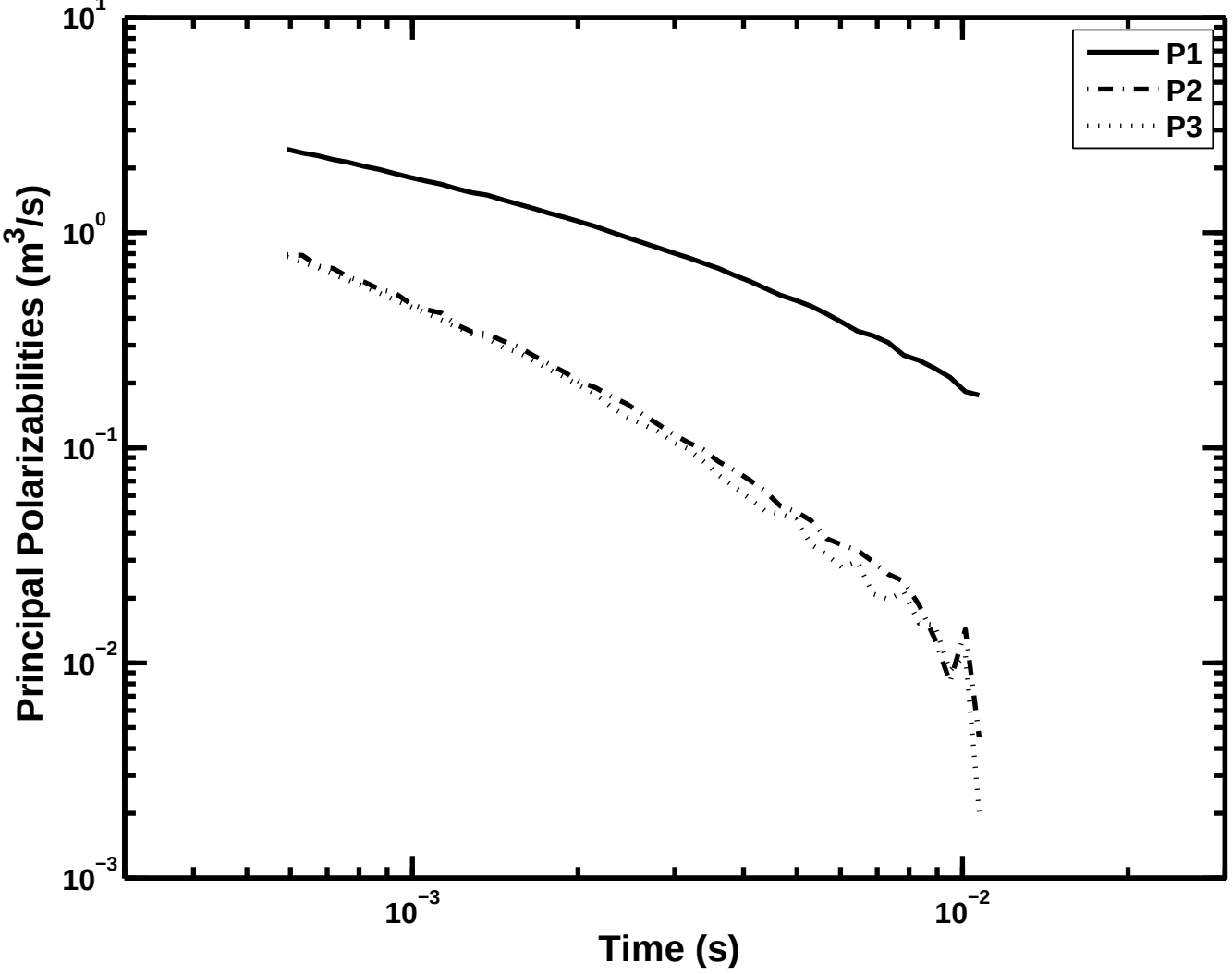

Figure A1−34: Principal polarizabilities as a function of time − 105−mm projectile, position = P3, depth = 0.73 m, orient−v = 90,orient−xy = 90

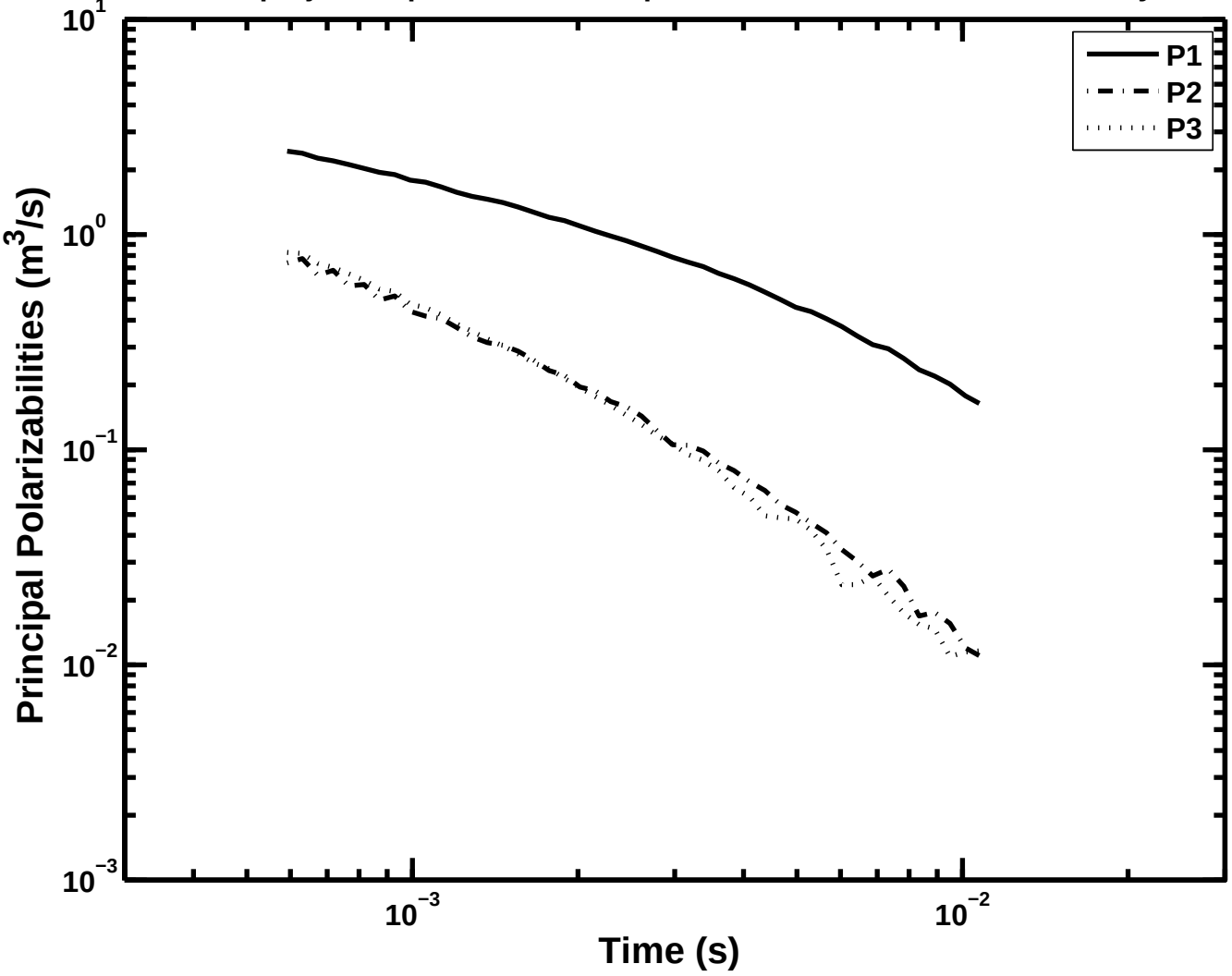

Figure A1−35: Principal polarizabilities as a function of time − 105−mm projectile, position = P3, depth = 0.35 m, orient−v = 90,orient−xy = 135

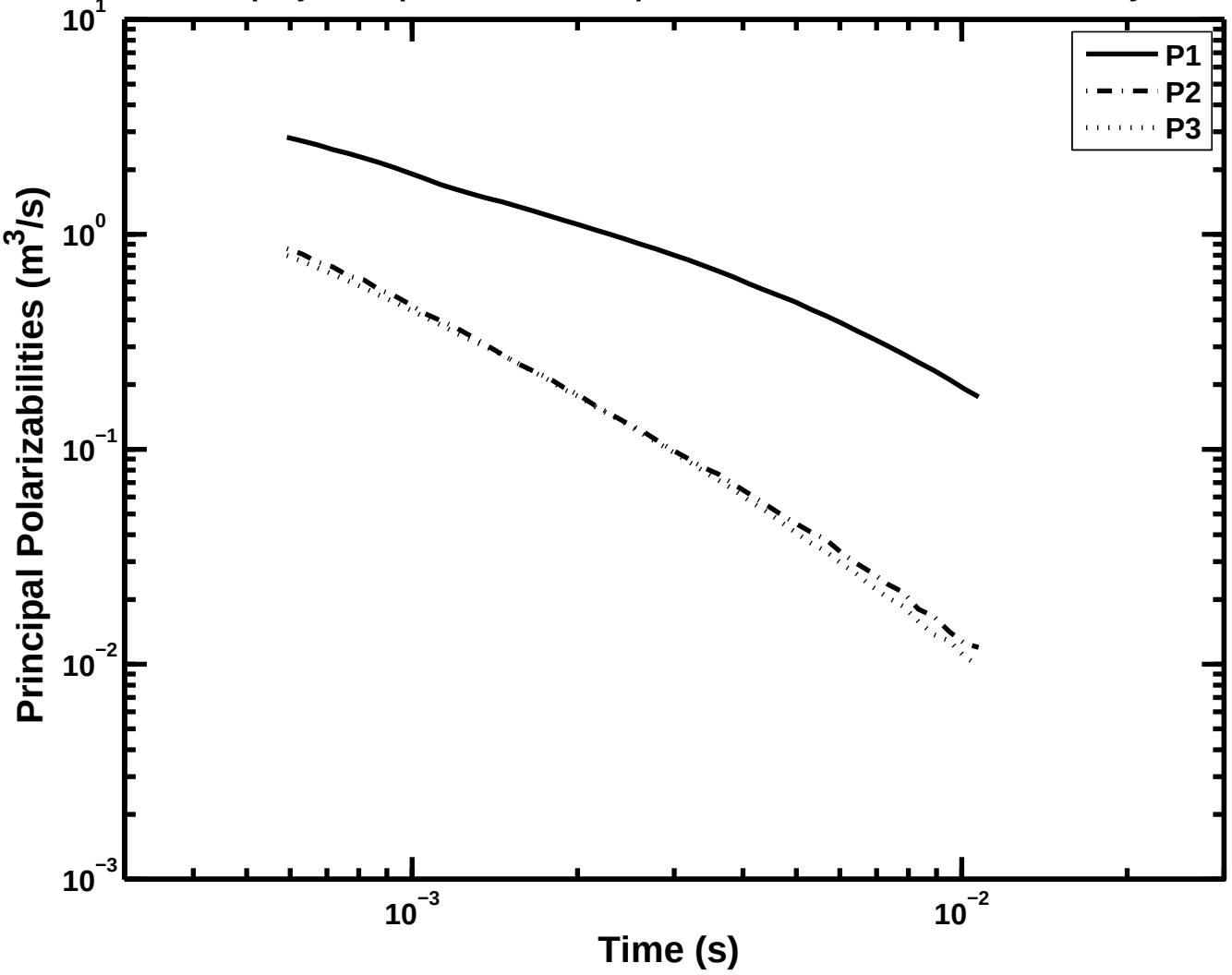

Figure A1−36: Principal polarizabilities as a function of time − 105−mm projectile, position = P3, depth = 0.75 m, orient−v = 45,orient−xy = N/A

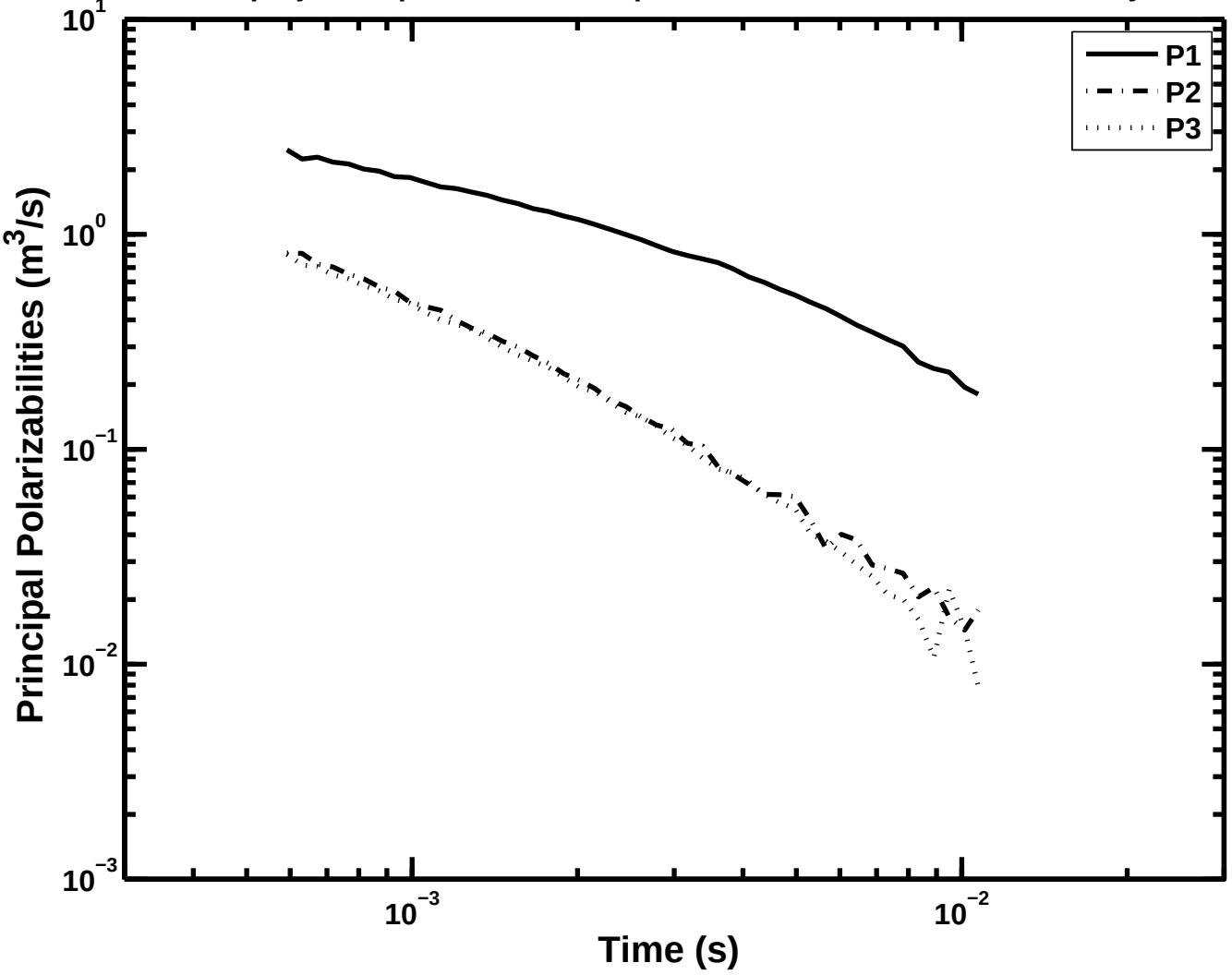

Figure A1−37: Principal polarizabilities as a function of time − 105−mm projectile, position = P44, depth = 0.4 m, orient−v = 0,orient−xy = N/A

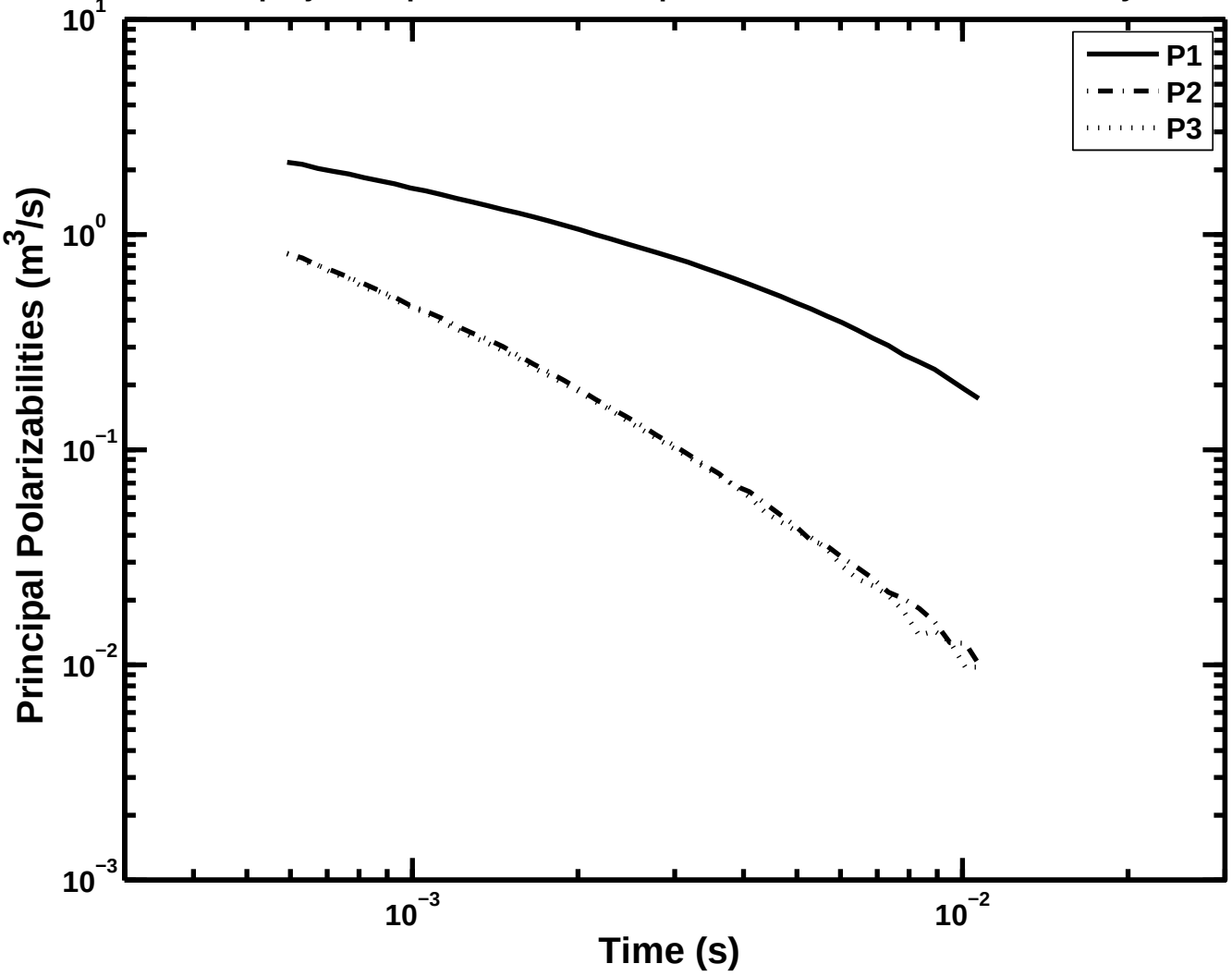

Figure A1−38: Principal polarizabilities as a function of time − 105−mm projectile, position = P44, depth = 0.7 m, orient−v = 90,orient−xy = N/A

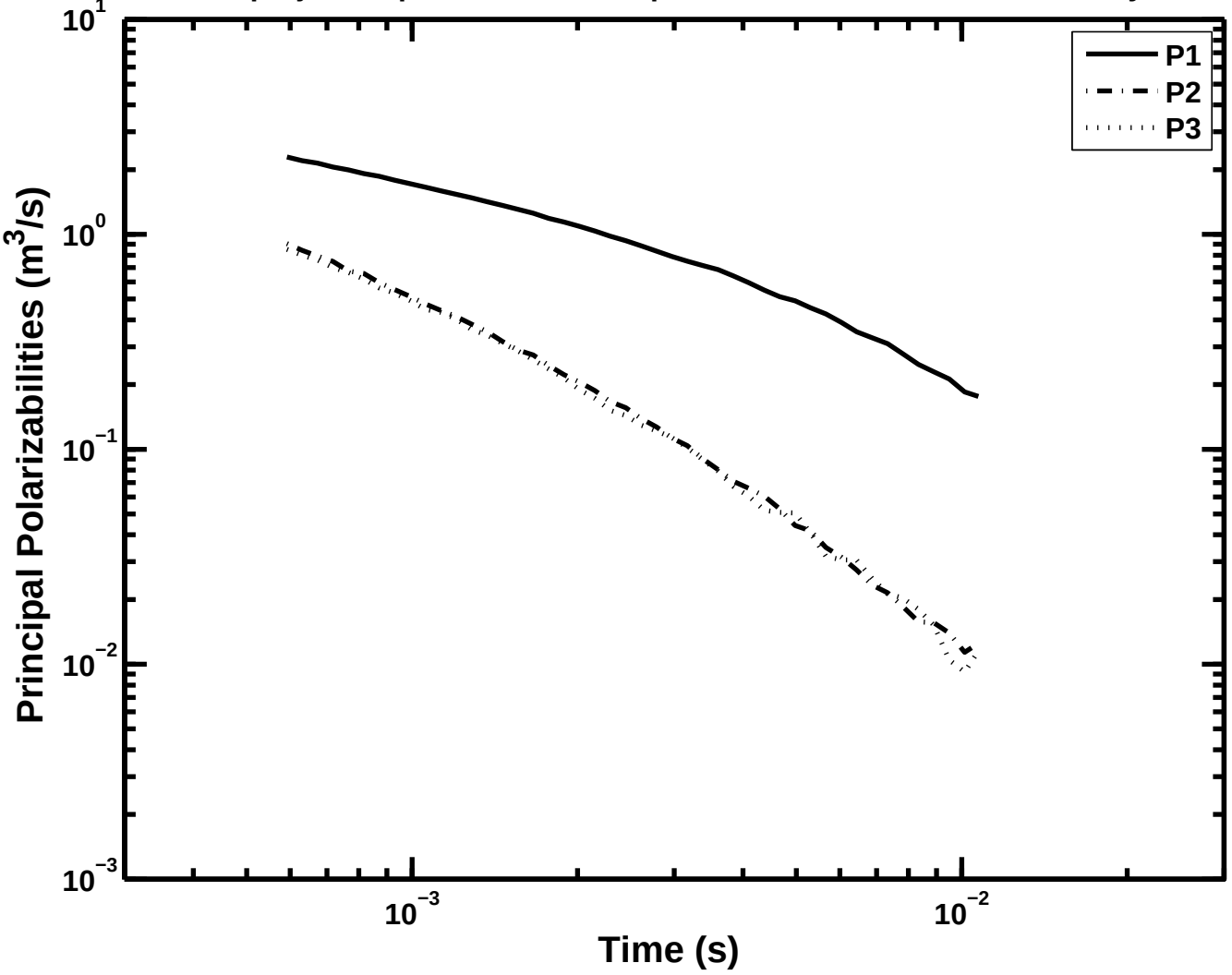

Figure A1−39: Principal polarizabilities as a function of time − 105−mm projectile, position = P4, depth = 0.35 m, orient−v = 90,orient−xy = 0

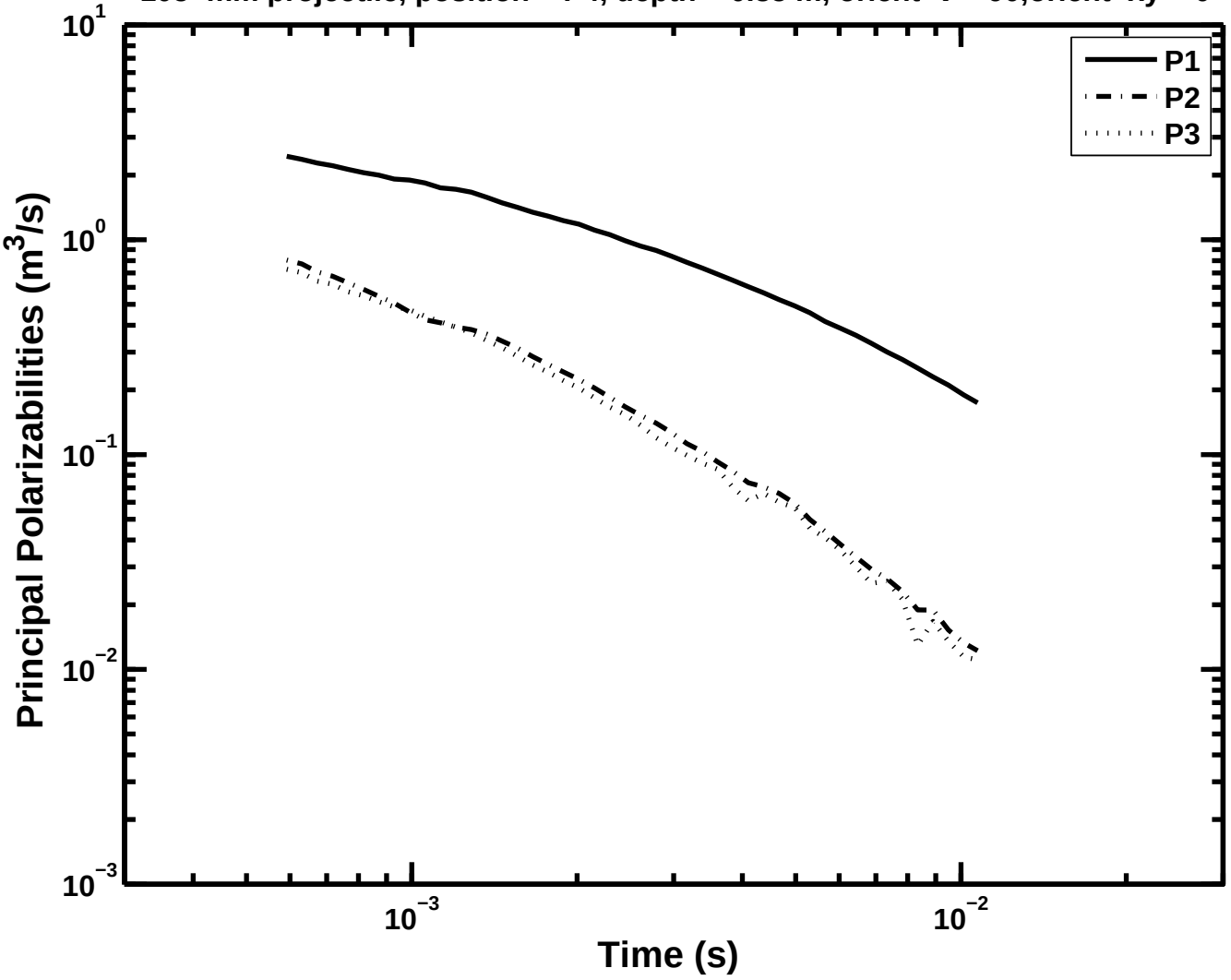

Figure A1−40: Principal polarizabilities as a function of time − 105−mm projectile, position = P4, depth = 0.75 m, orient−v = 60,orient−xy = N/A

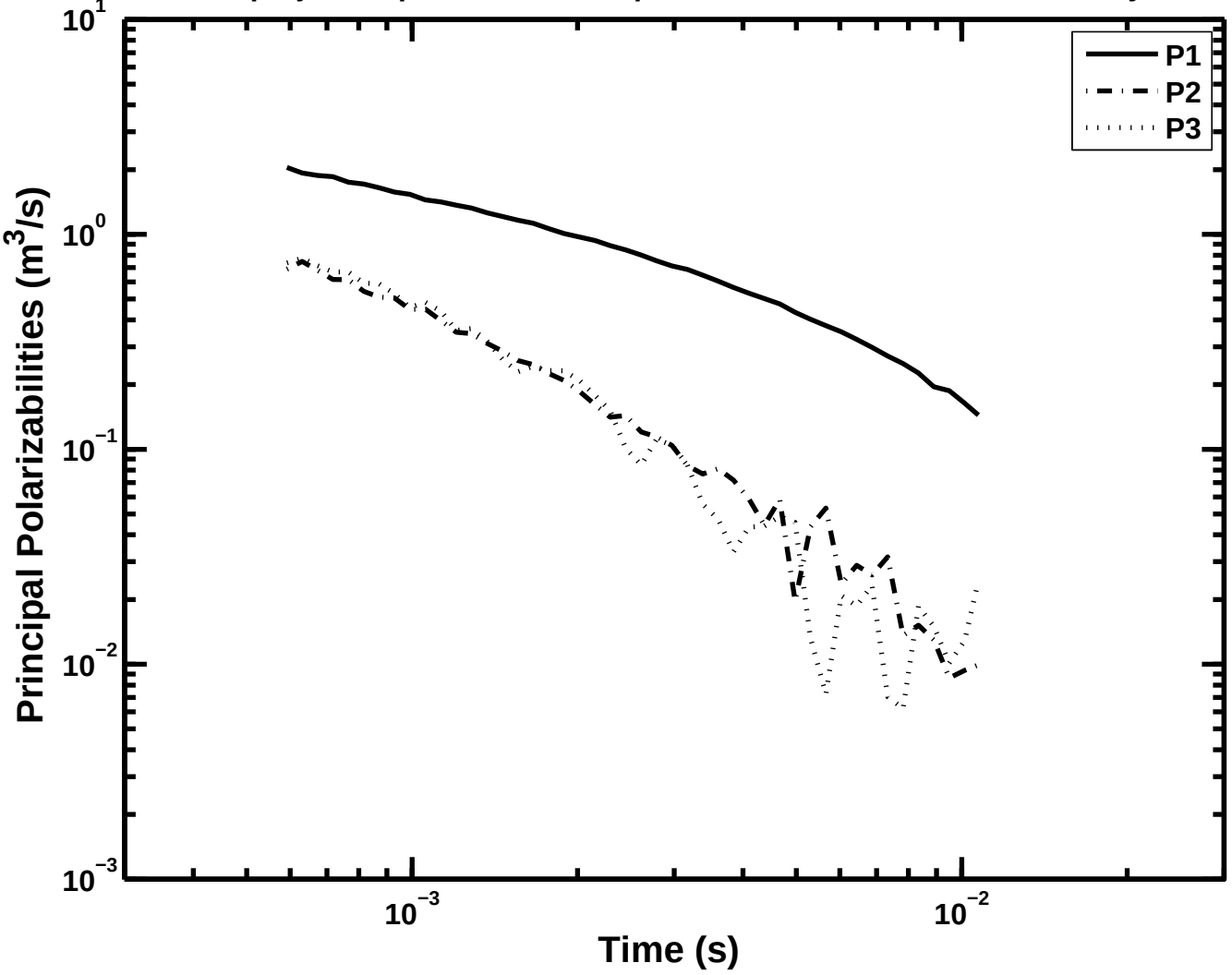

Figure A1−41: Principal polarizabilities as a function of time − 105−mm projectile, position = P4, depth = 0.75 m, orient−v = 60,orient−xy = N/A

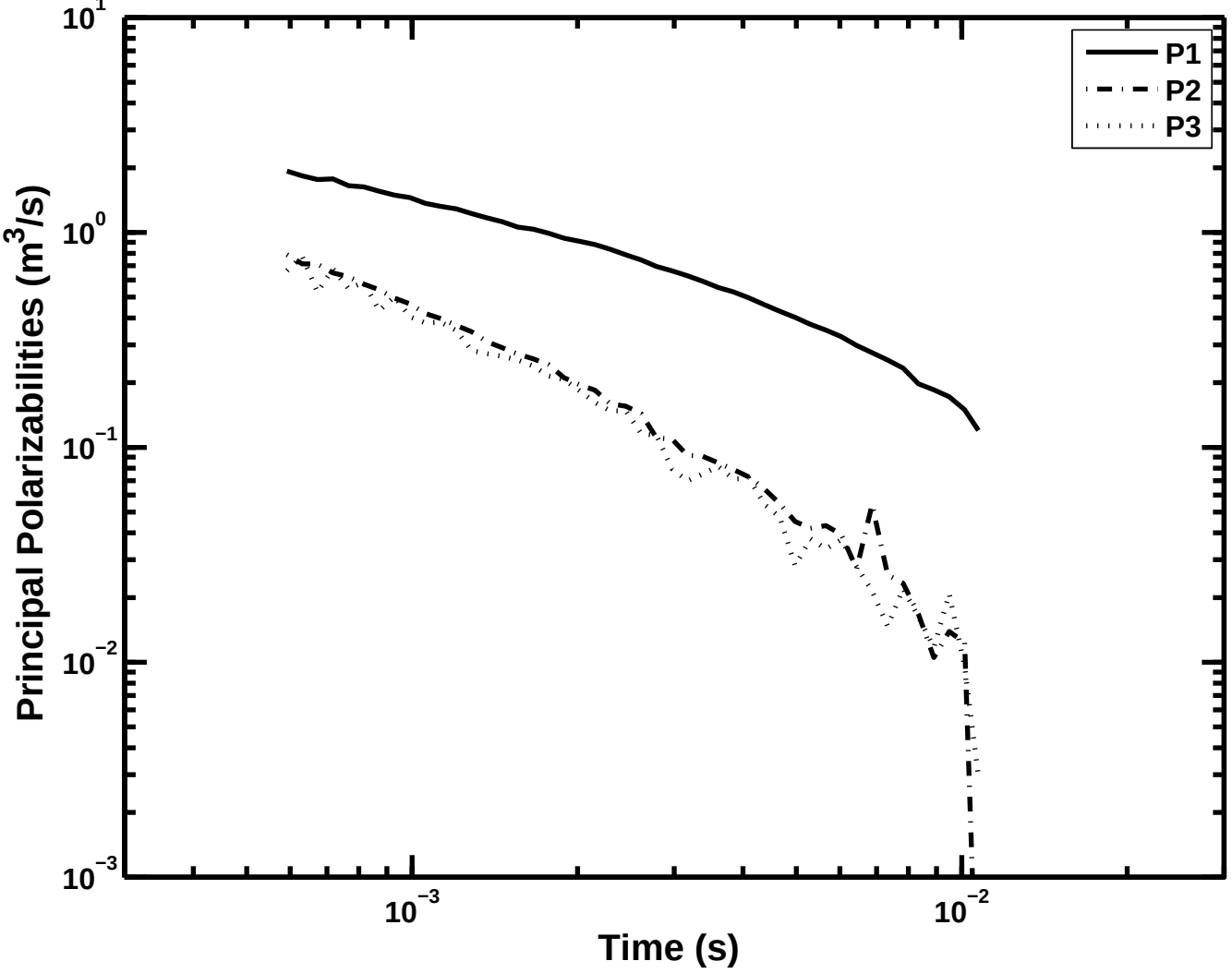

Figure A1−42: Principal polarizabilities as a function of time − 2.75−in rocket, position = P1, depth = 0.36 m, orient−v = 90,orient−xy = 90

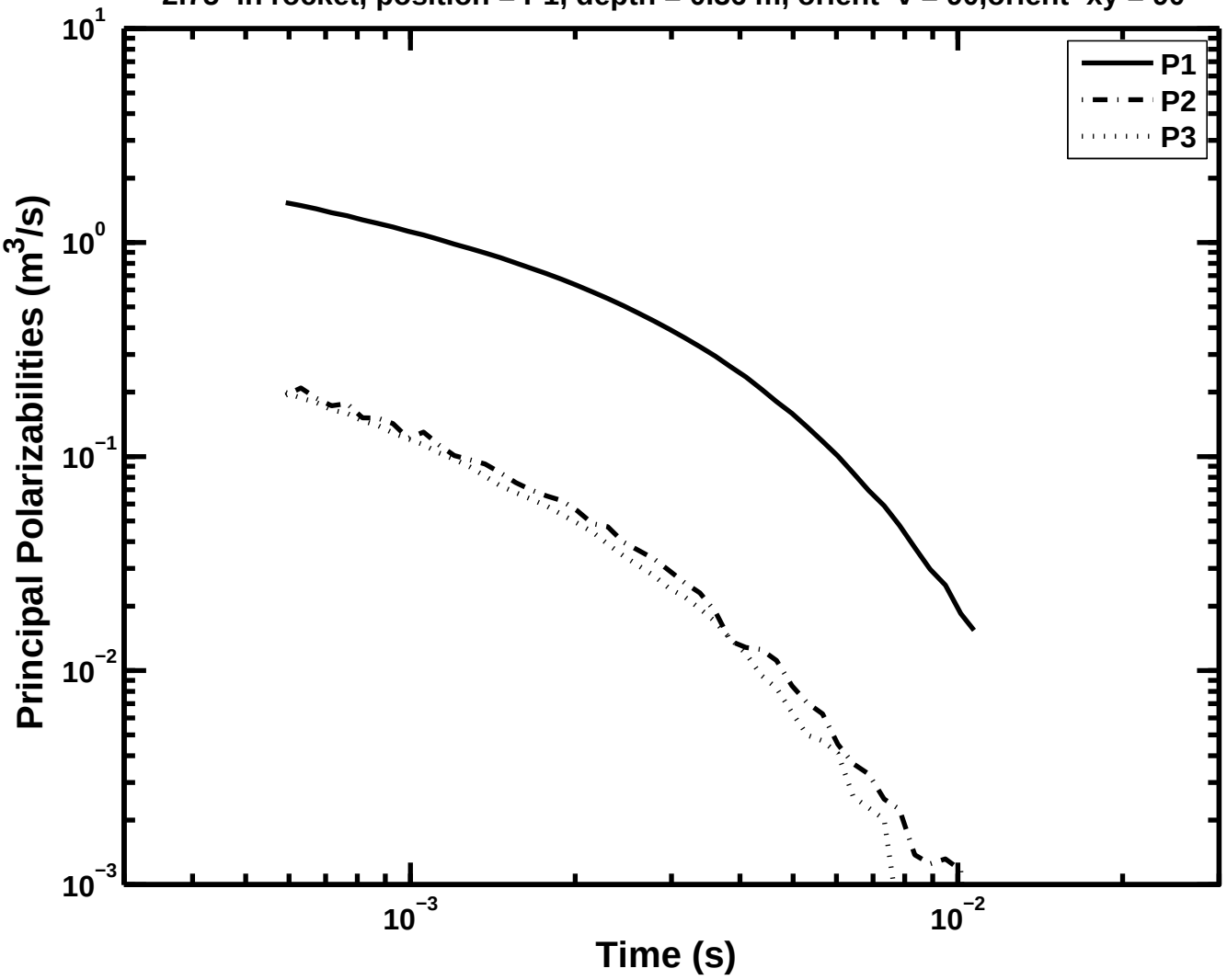

Figure A1−43: Principal polarizabilities as a function of time − 2.75−in rocket, position = P1, depth = 0.66 m, orient−v = 90,orient−xy = 90

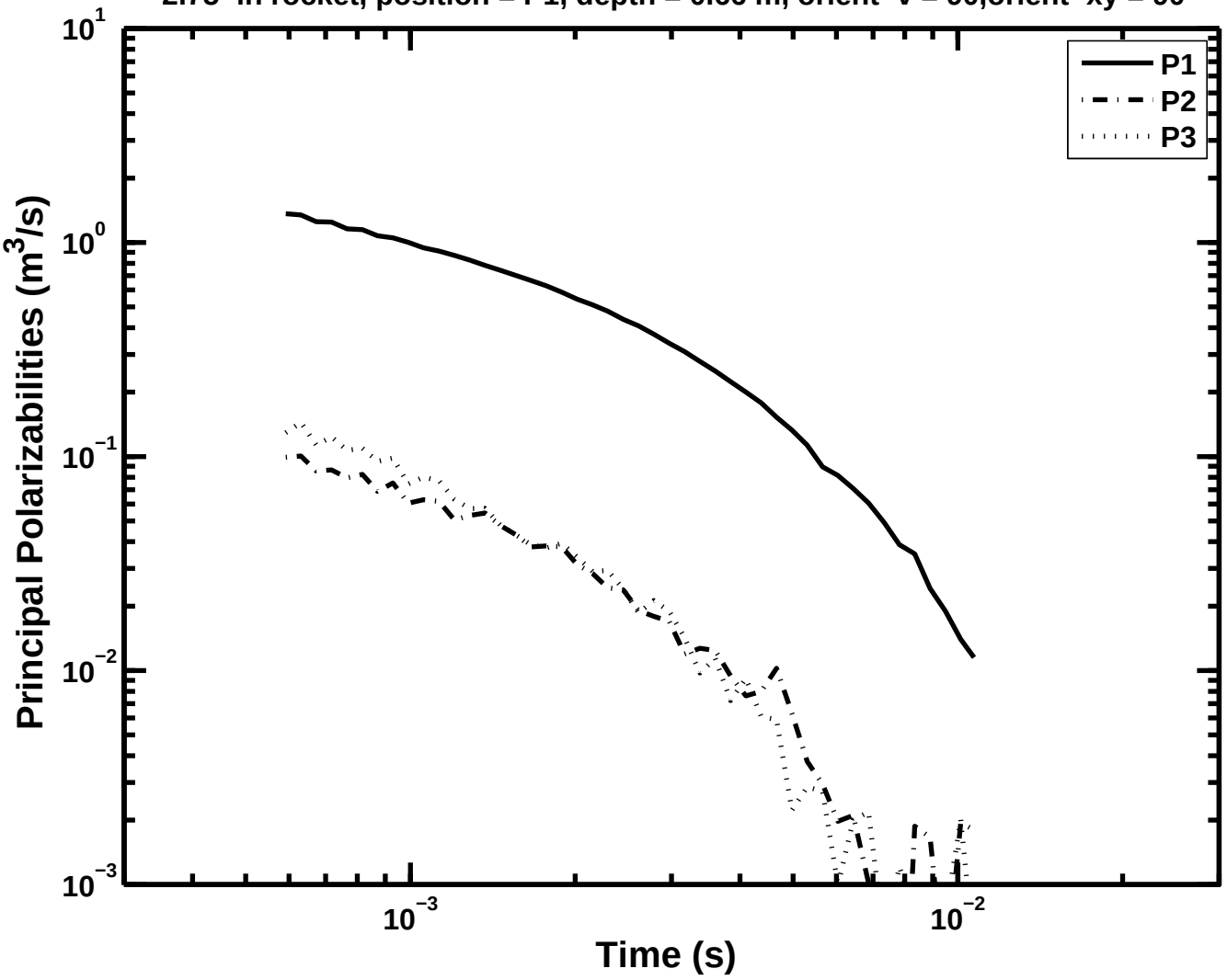

Figure A1−44: Principal polarizabilities as a function of time − 2.75−in rocket, position = P22, depth = 0.7 m, orient−v = 0,orient−xy = N/A

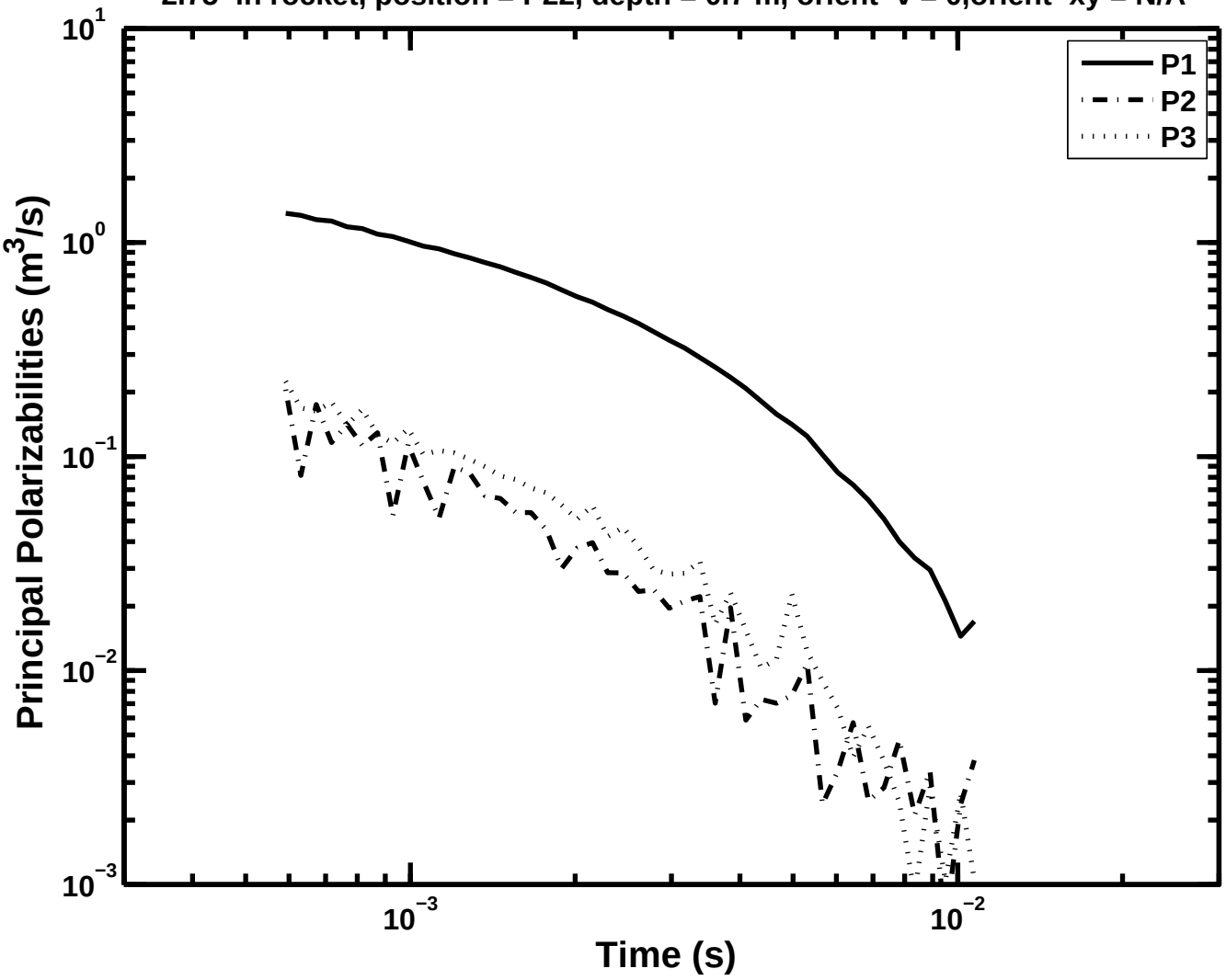

Figure A1−45: Principal polarizabilities as a function of time − 2.75−in rocket, position = P2, depth = 0.36 m, orient−v = 90,orient−xy = 90

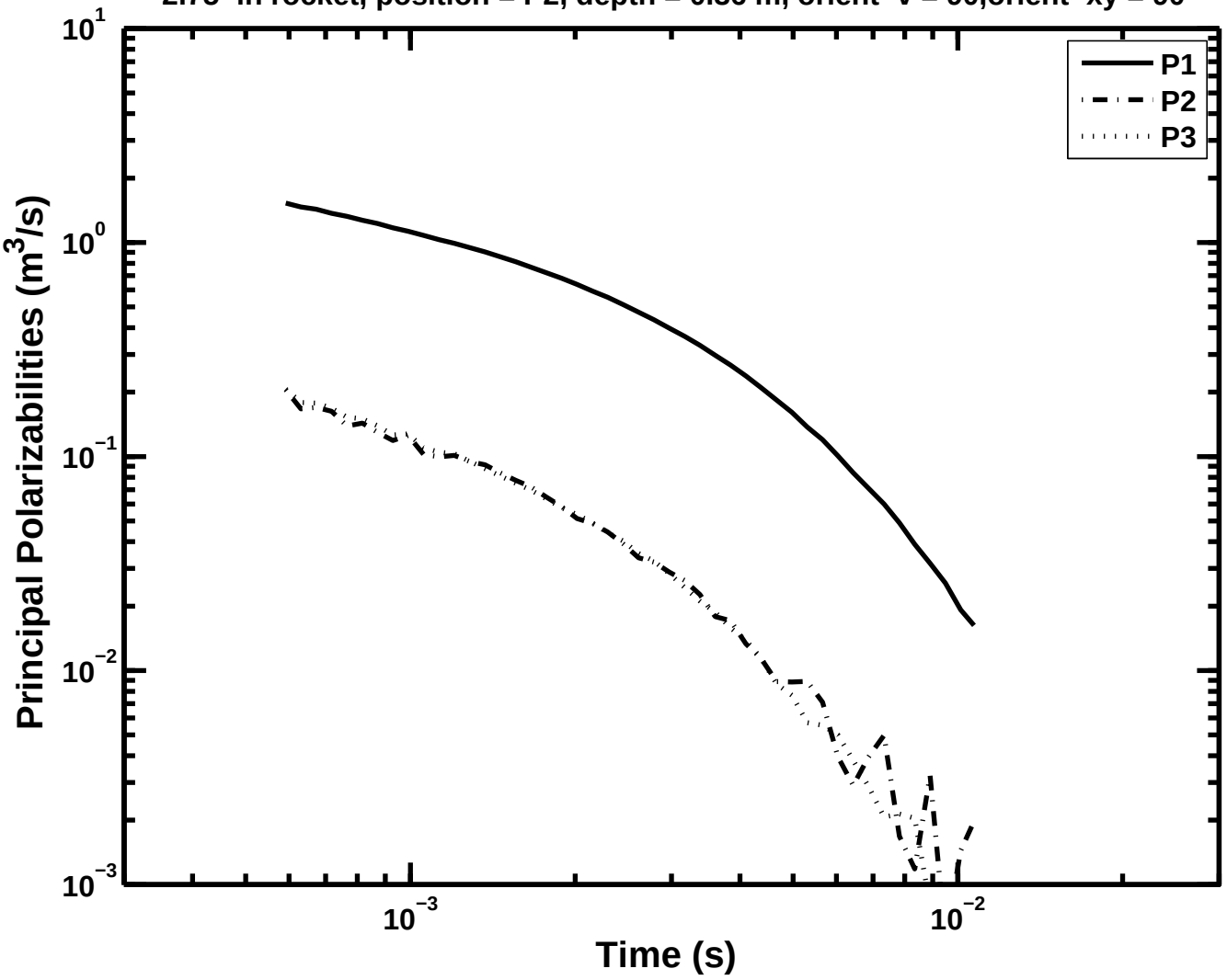

Figure A1−46: Principal polarizabilities as a function of time − 2.75−in rocket, position = P2, depth = 0.36 m, orient−v = 90,orient−xy = 90

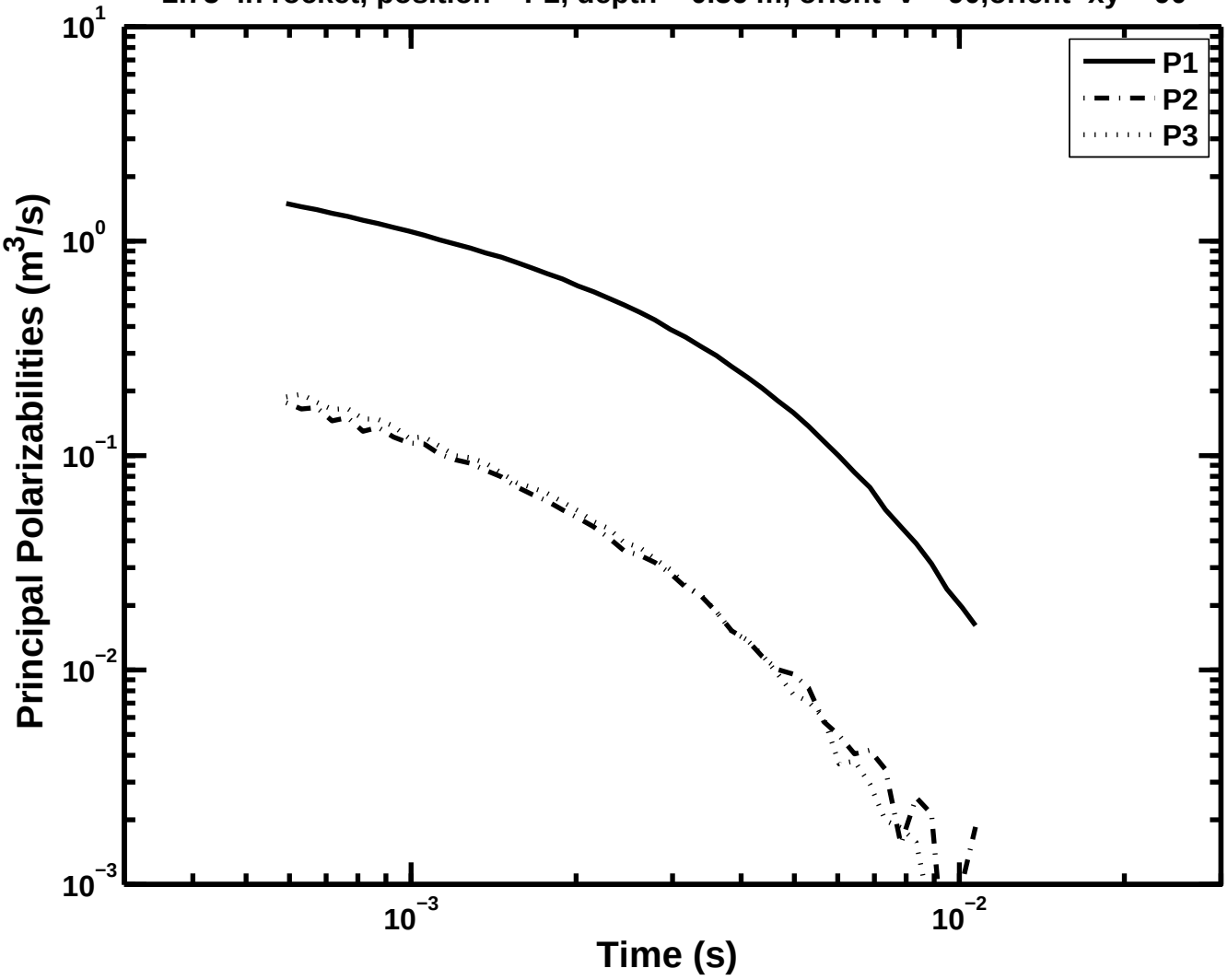

Figure A1−47: Principal polarizabilities as a function of time − 2.75−in rocket, position = P2, depth = 0.66 m, orient−v = 90,orient−xy = 90

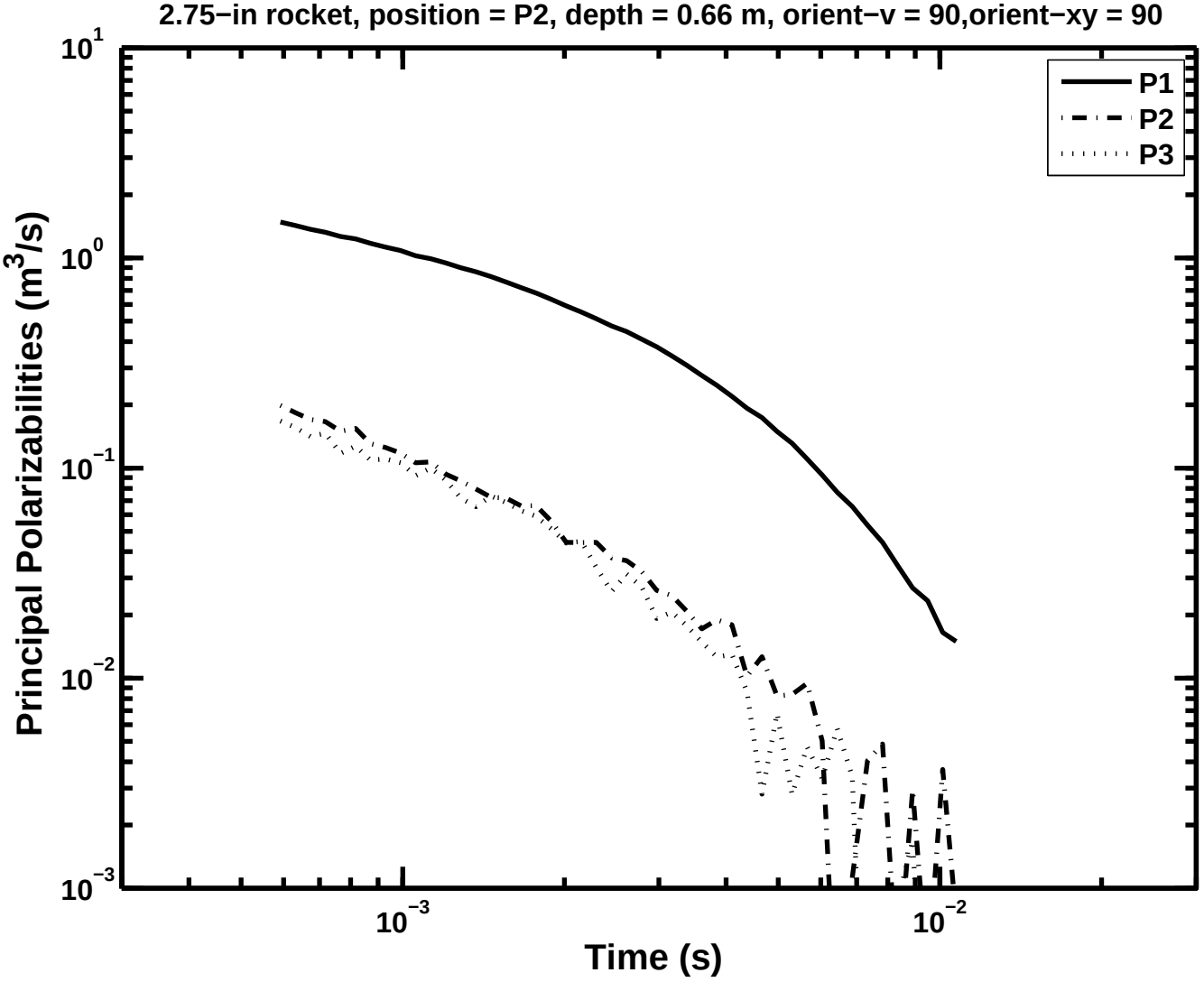

Figure A1−48: Principal polarizabilities as a function of time − 2.75−in rocket, position = P3, depth = 0.36 m, orient−v = 90,orient−xy = 90

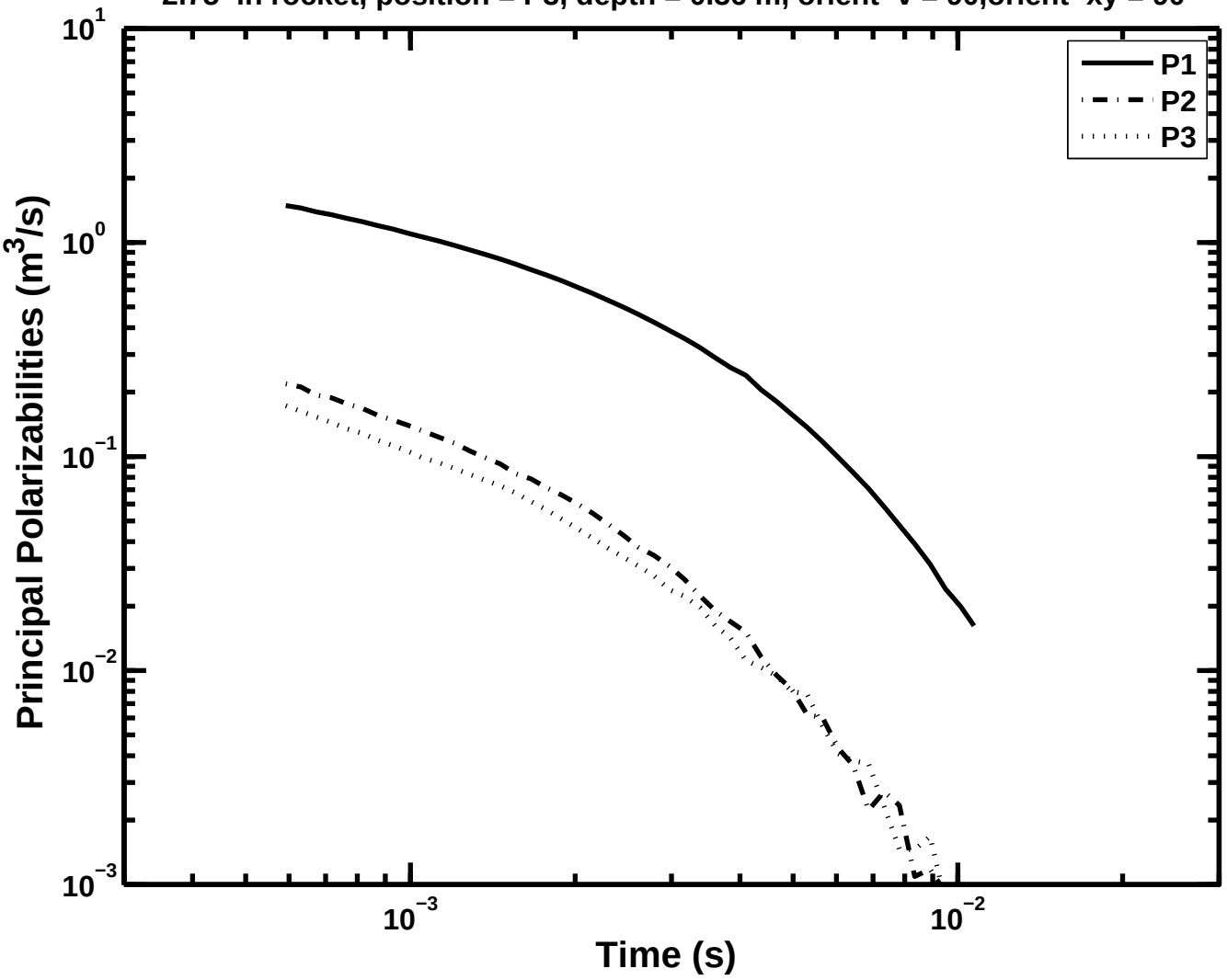

Figure A1−49: Principal polarizabilities as a function of time − 2.75−in rocket, position = P3, depth = 0.66 m, orient−v = 90,orient−xy = 90

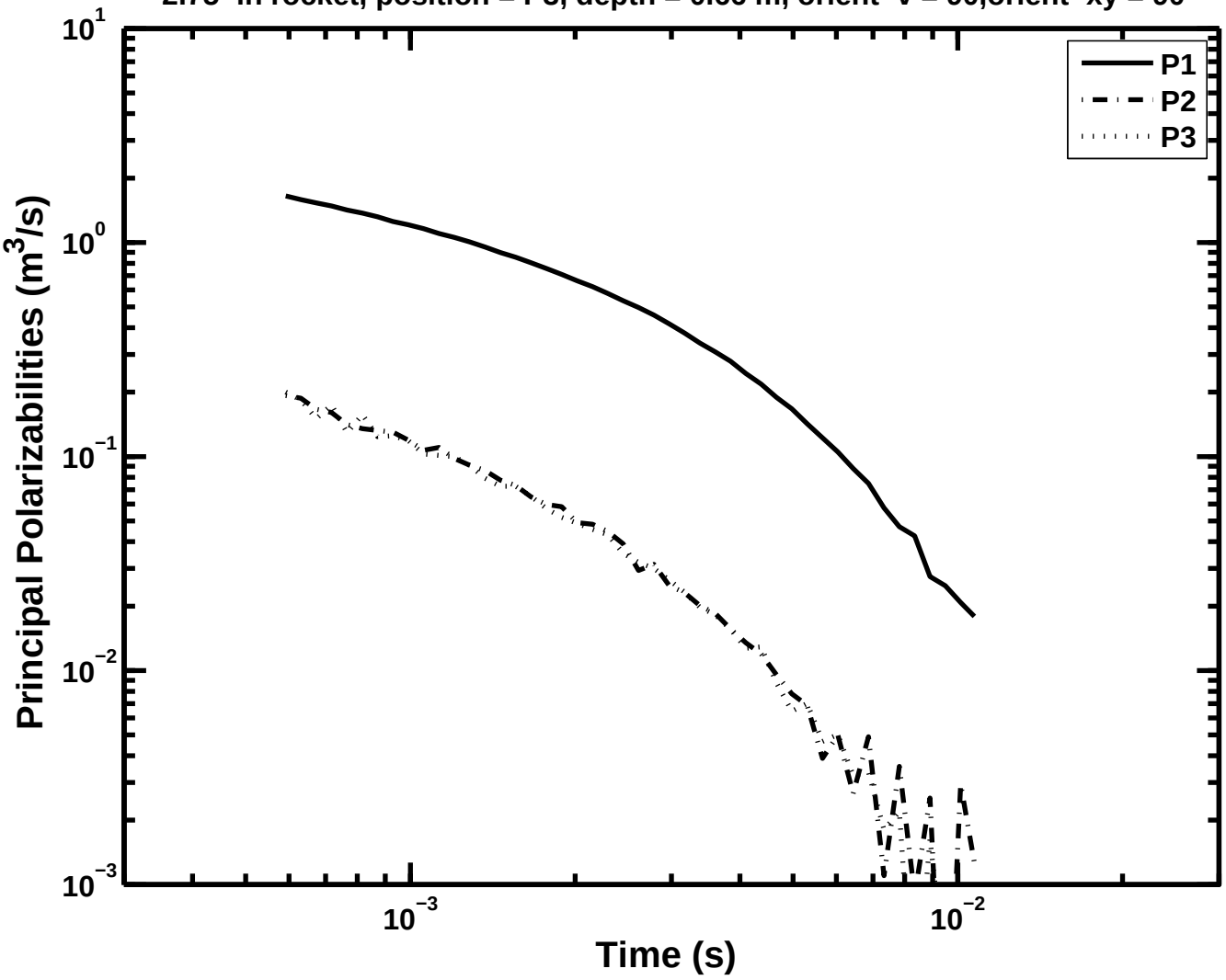

Figure A1−50: Principal polarizabilities as a function of time − 2.75−in rocket, position = P3, depth = 0.36 m, orient−v = −30,orient−xy = N/A

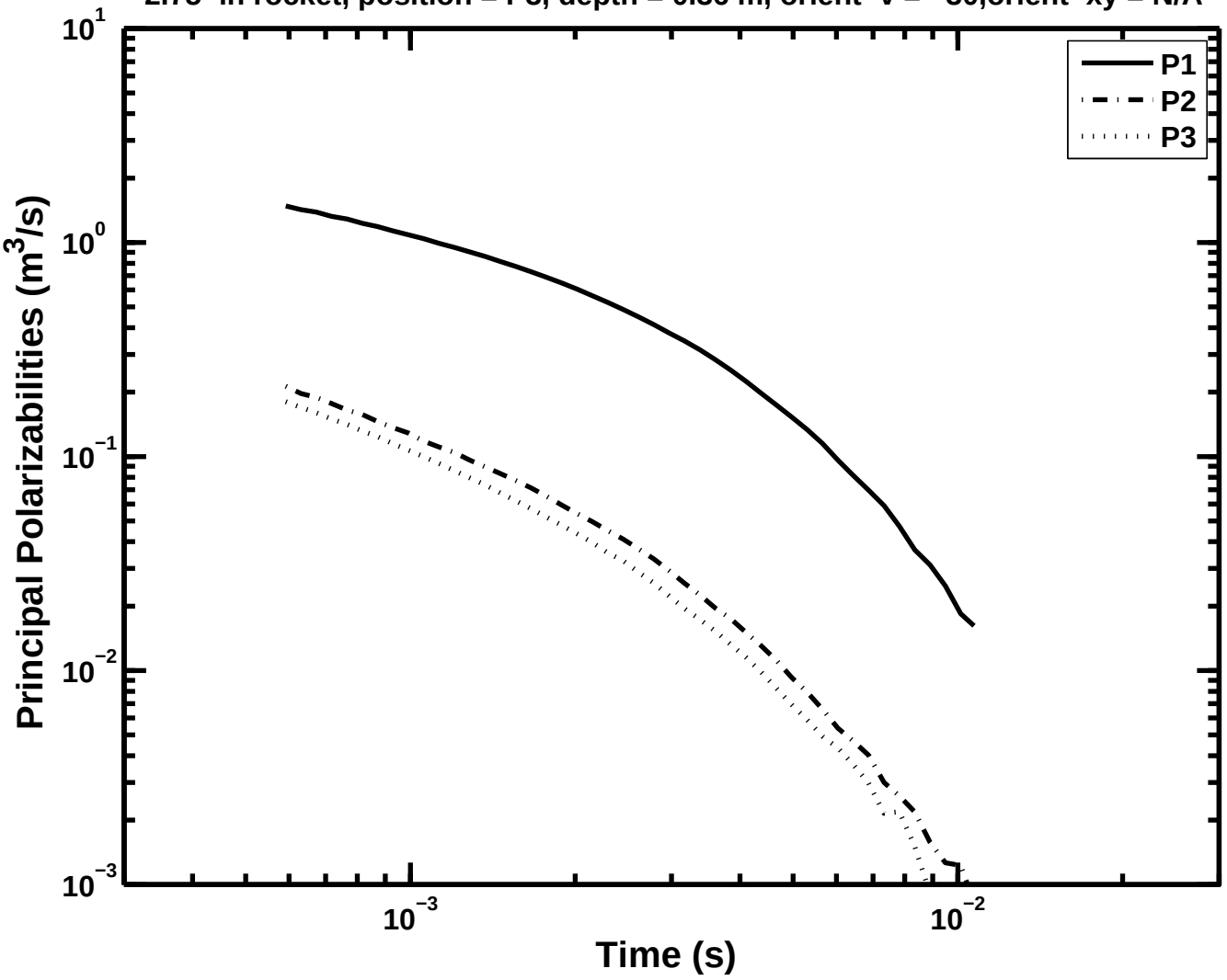

Figure A1−51: Principal polarizabilities as a function of time − 2.75−in rocket, position = P3, depth = 0.36 m, orient−v = 120,orient−xy = N/A

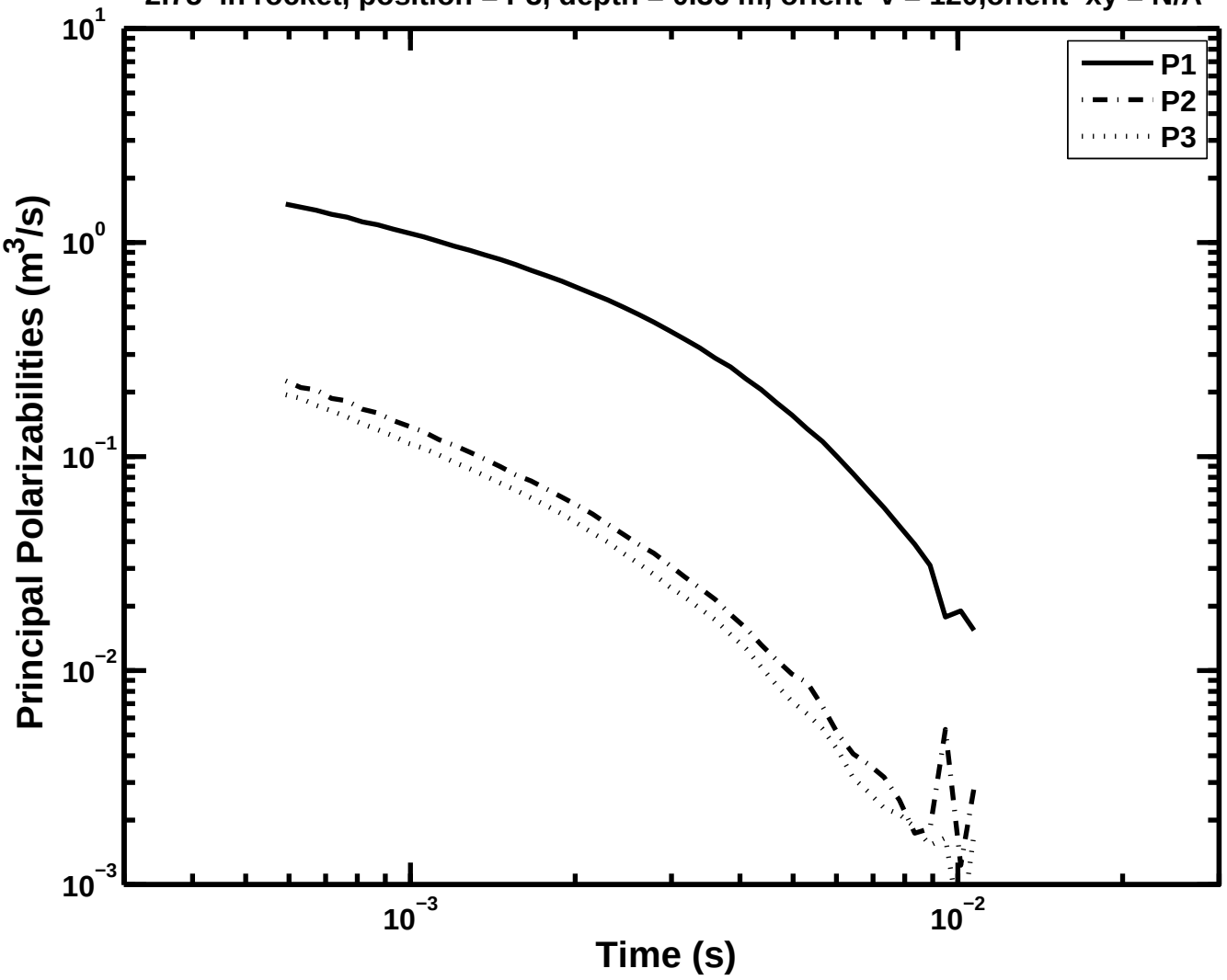

Figure A1−52: Principal polarizabilities as a function of time − 2.75−in rocket, position = P3, depth = 0.36 m, orient−v = 90,orient−xy = −135

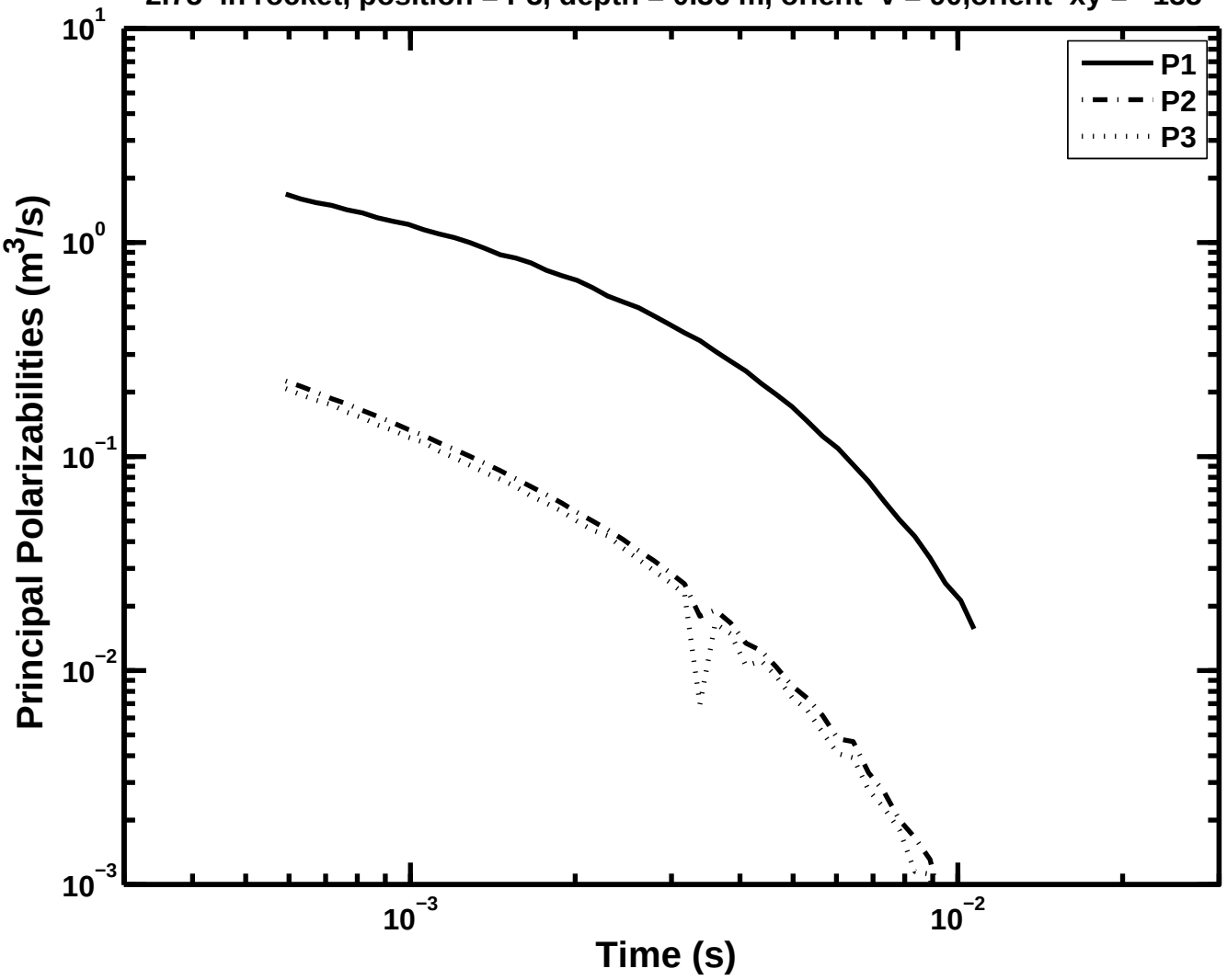

Figure A1−53: Principal polarizabilities as a function of time − 2.75−in rocket, position = P44, depth = 0.7 m, orient−v = 0,orient−xy = N/A

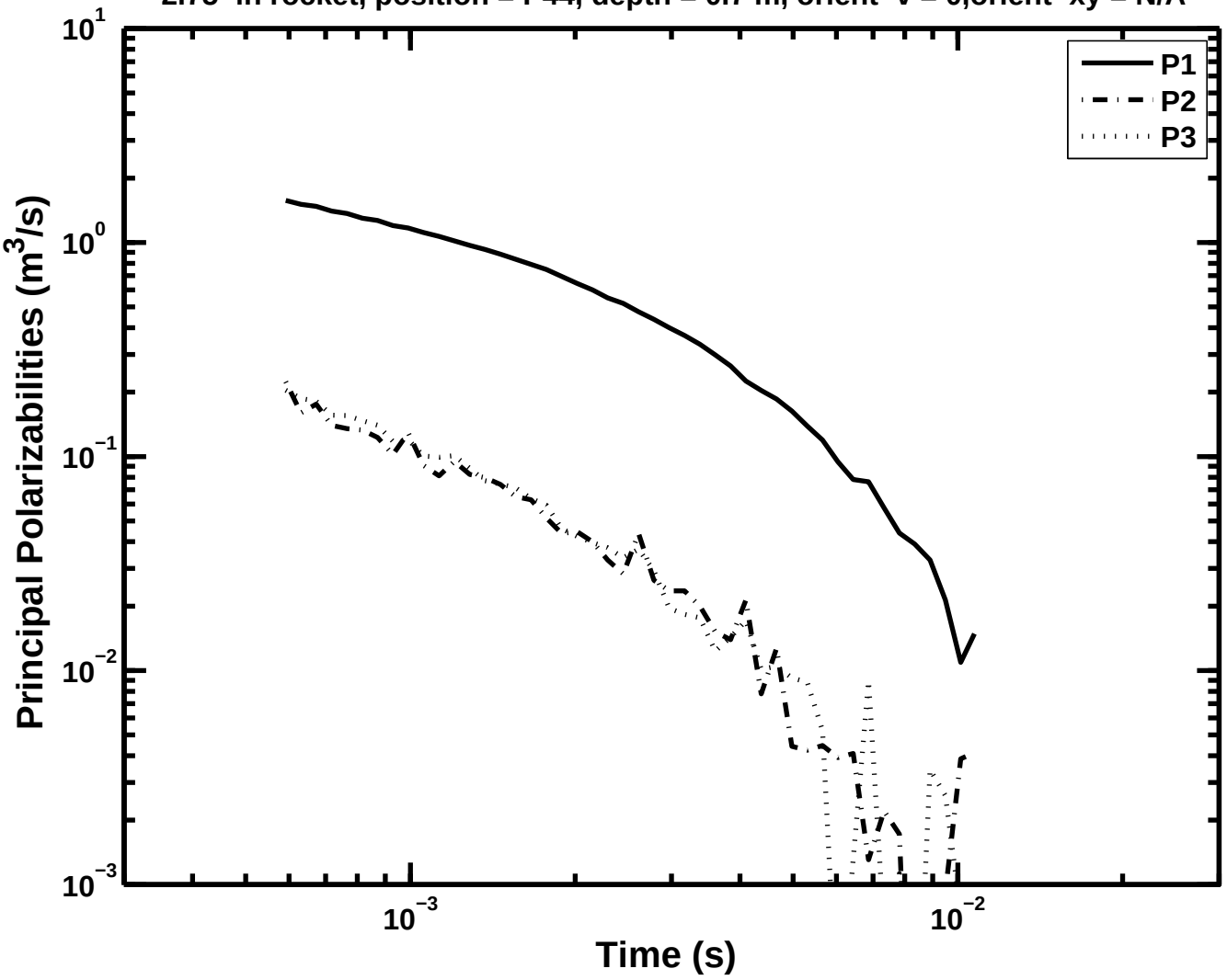

Figure A1−54: Principal polarizabilities as a function of time − 2.75−in rocket, position = P4, depth = 0.36 m, orient−v = 90,orient−xy = 0

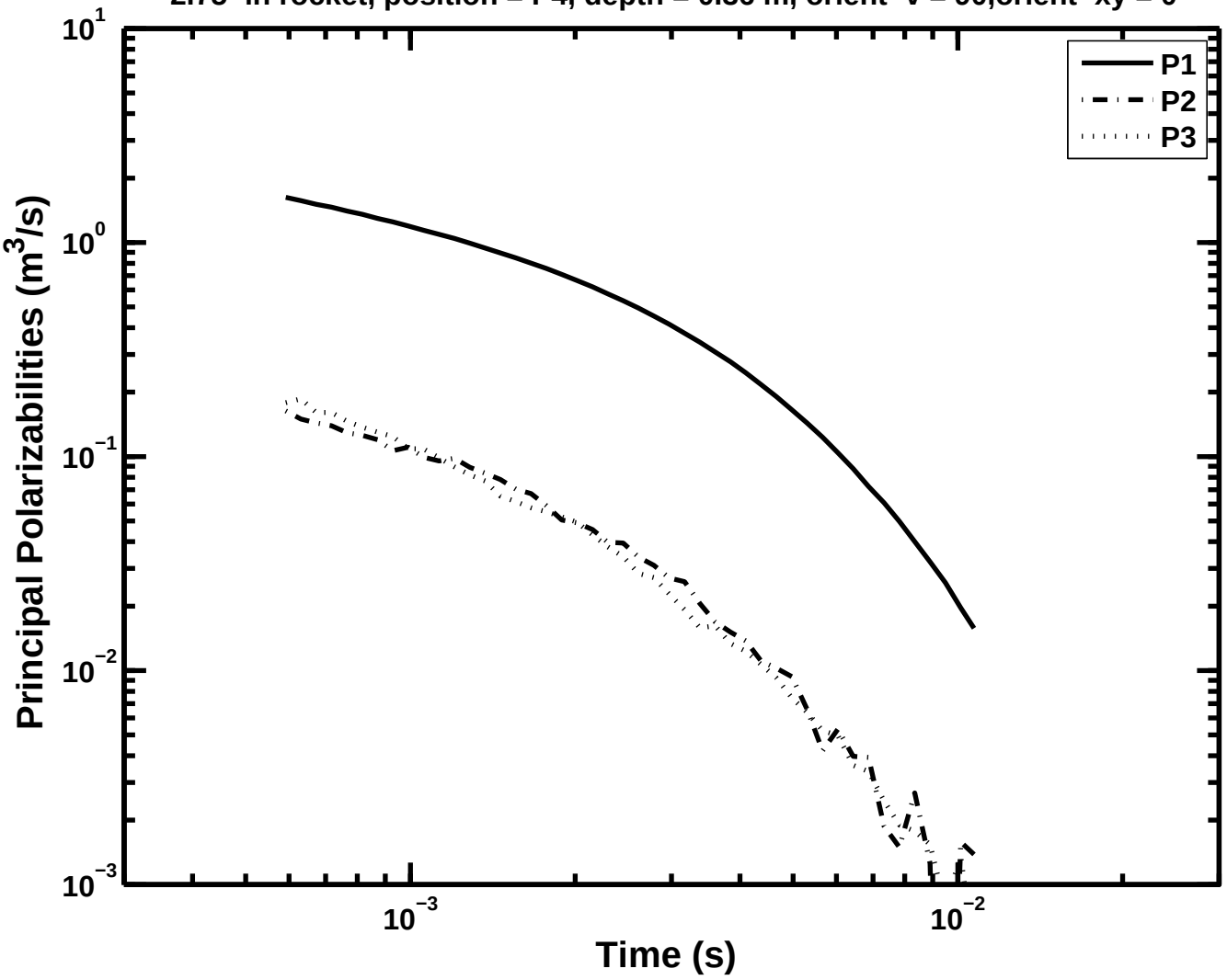

Figure A1−55: Principal polarizabilities as a function of time − 2.75−in rocket, position = P4, depth = 0.36 m, orient−v = 90,orient−xy = 0

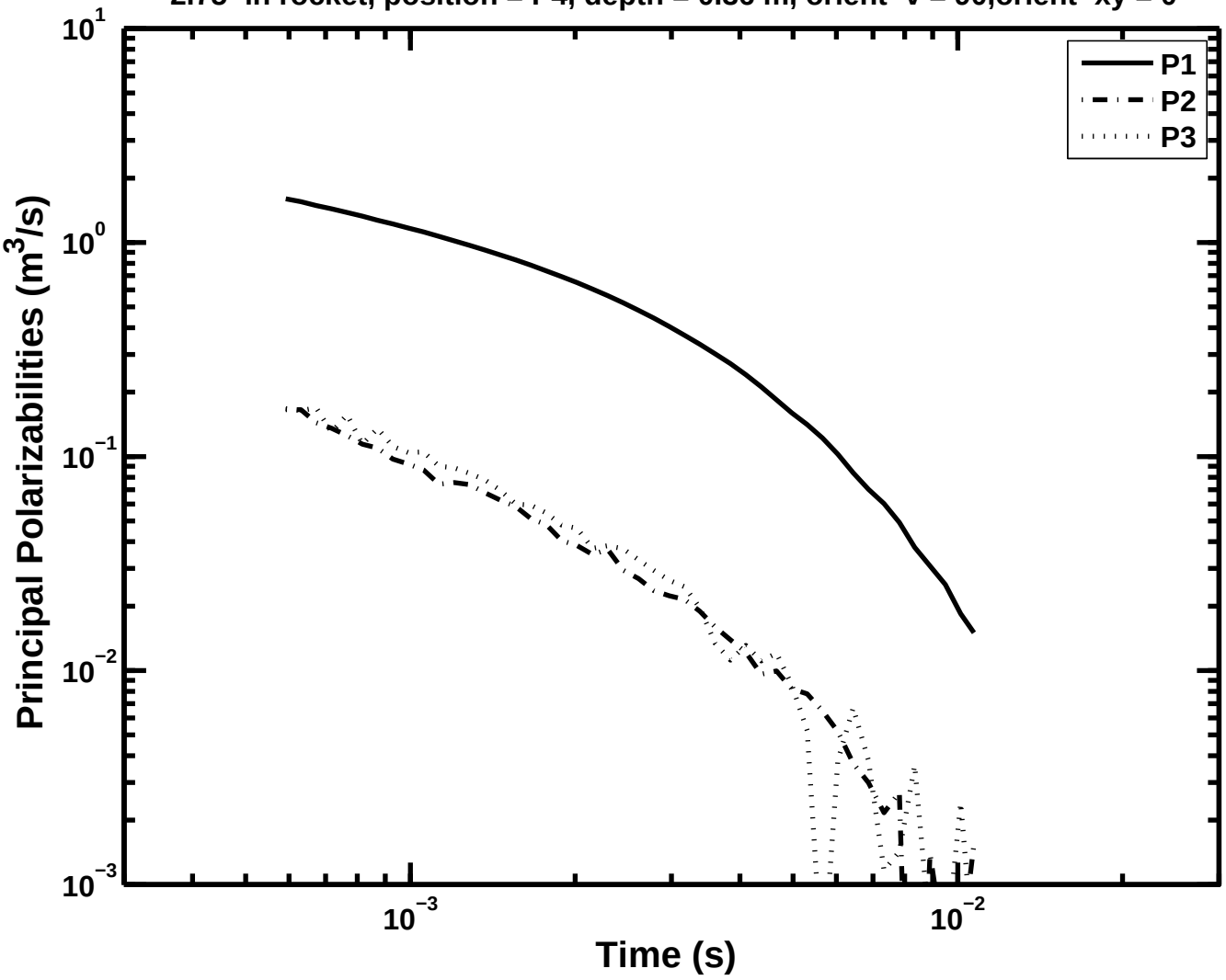

Figure A1−56: Principal polarizabilities as a function of time − 2.75−in rocket, position = P5, depth = 0.36 m, orient−v = 90,orient−xy = 0

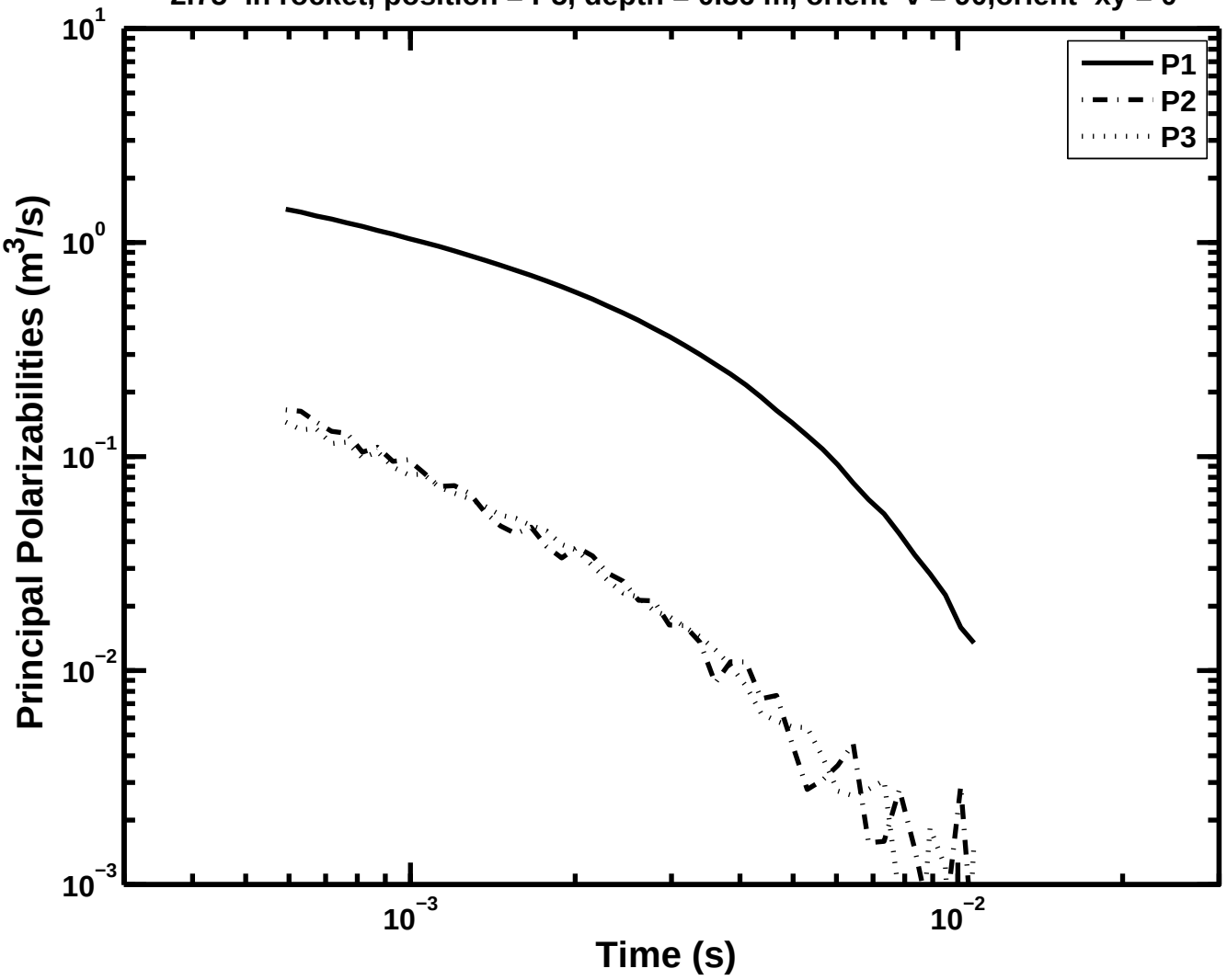

Figure A1−57: Principal polarizabilities as a function of time − 60−mm mortar, position = P3, depth = 0.37 m, orient−v = 90,orient−xy = 90

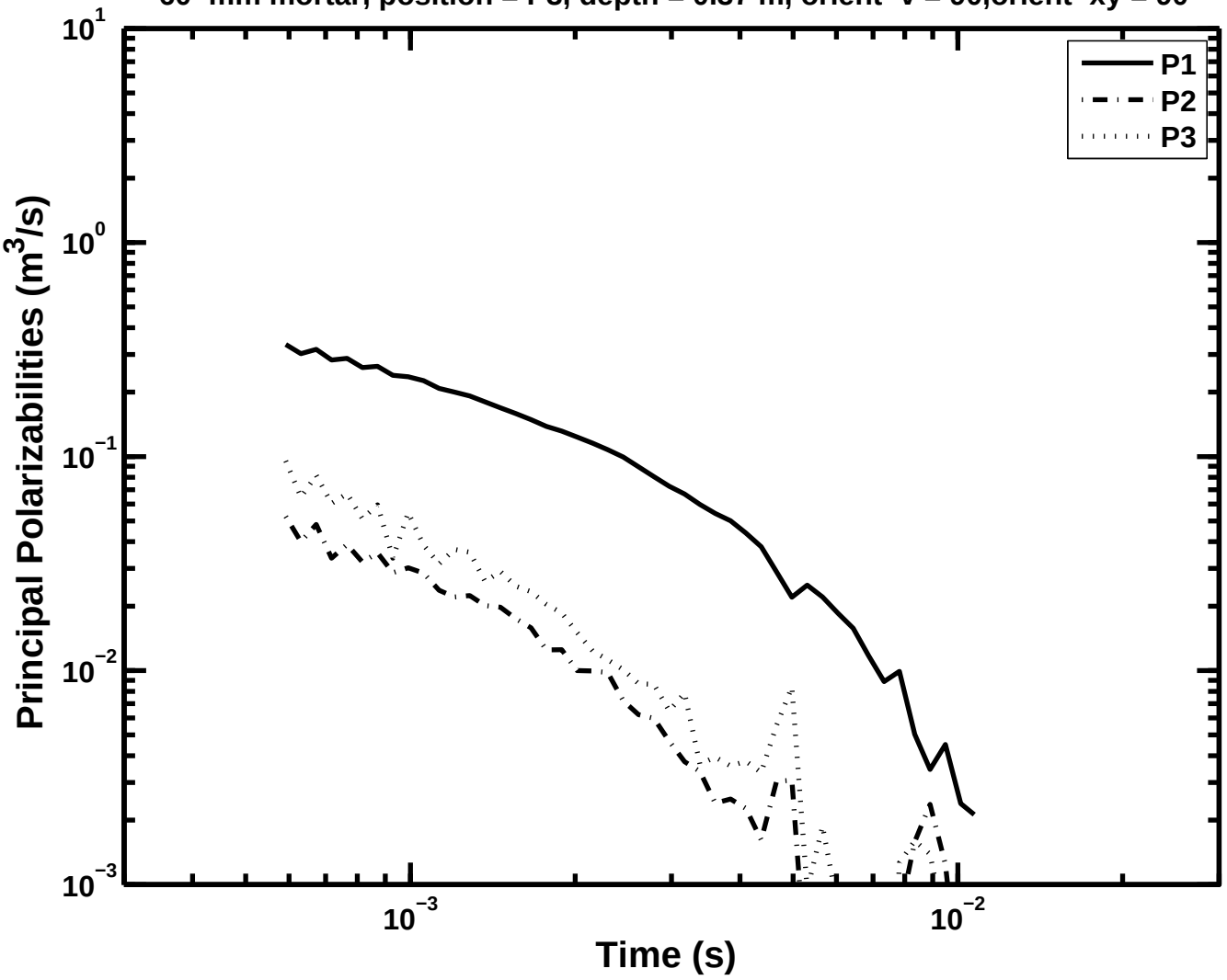

Figure A1−58: Principal polarizabilities as a function of time − 60−mm mortar, position = P3, depth = 0.37 m, orient−v = −30,orient−xy = N/A

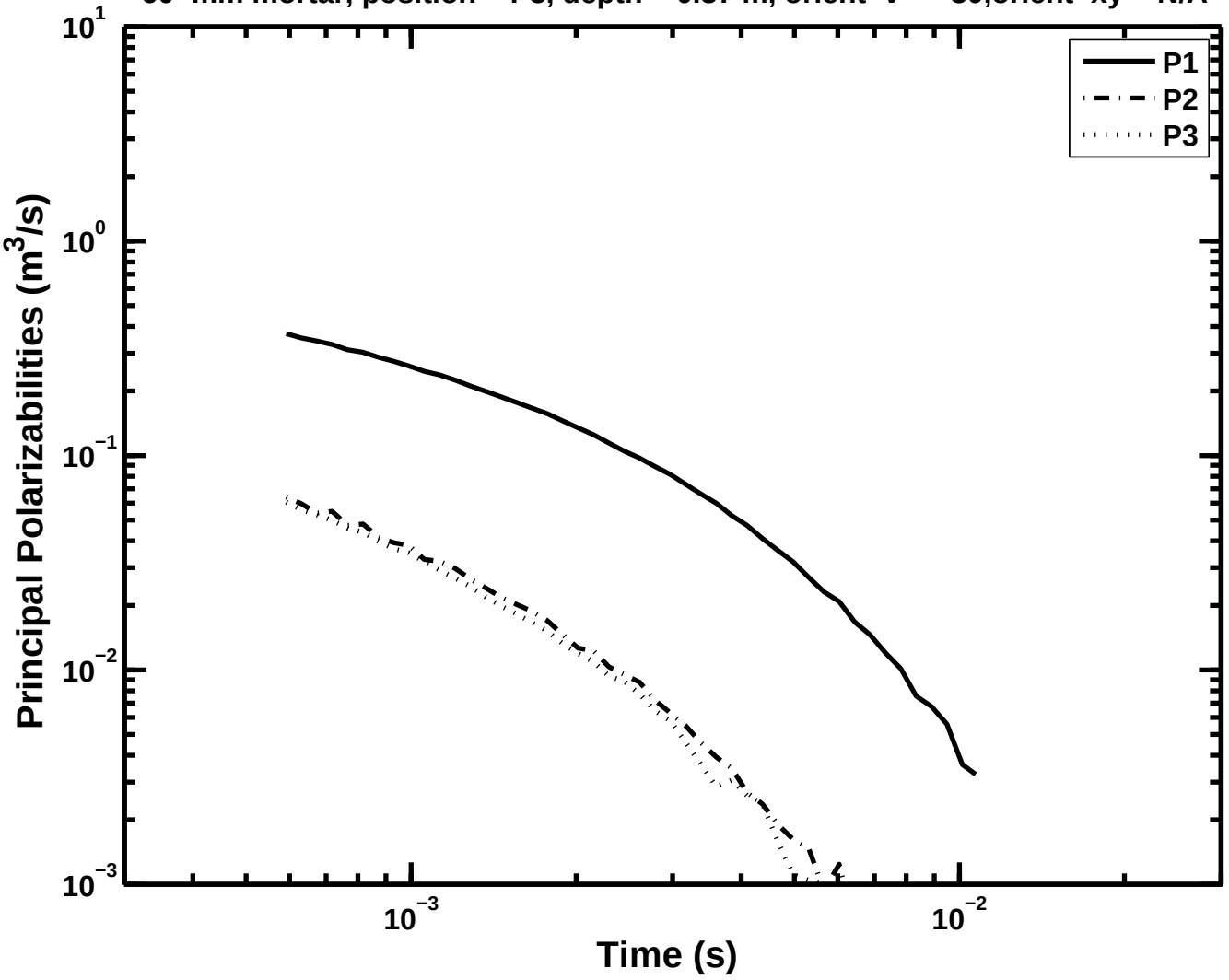

Figure A1−59: Principal polarizabilities as a function of time − 60−mm mortar, position = P3, depth = 0.37 m, orient−v = 120,orient−xy = N/A

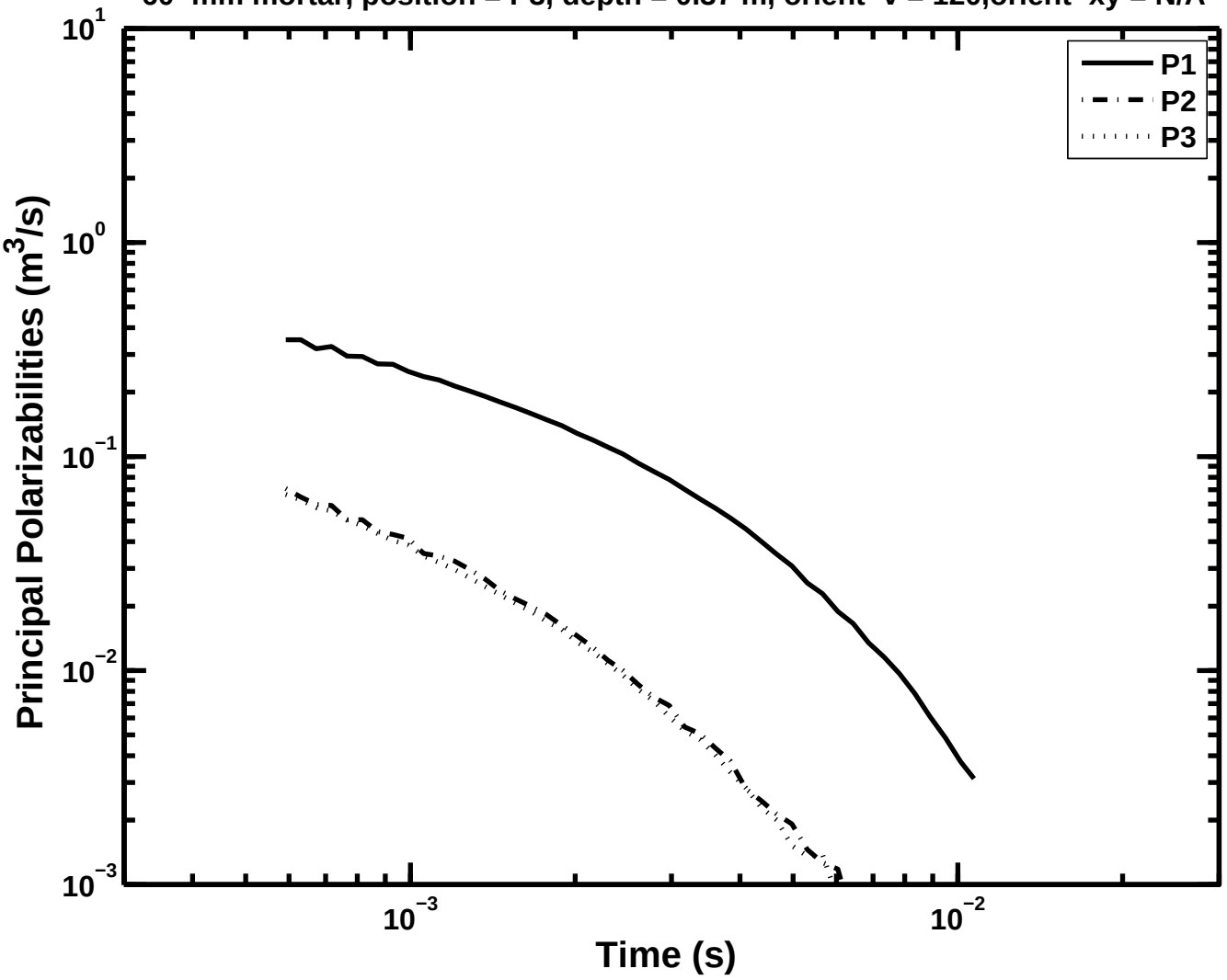

Figure A1−60: Principal polarizabilities as a function of time − 60−mm mortar, position = P3, depth = 0.37 m, orient−v = 90,orient−xy = 180

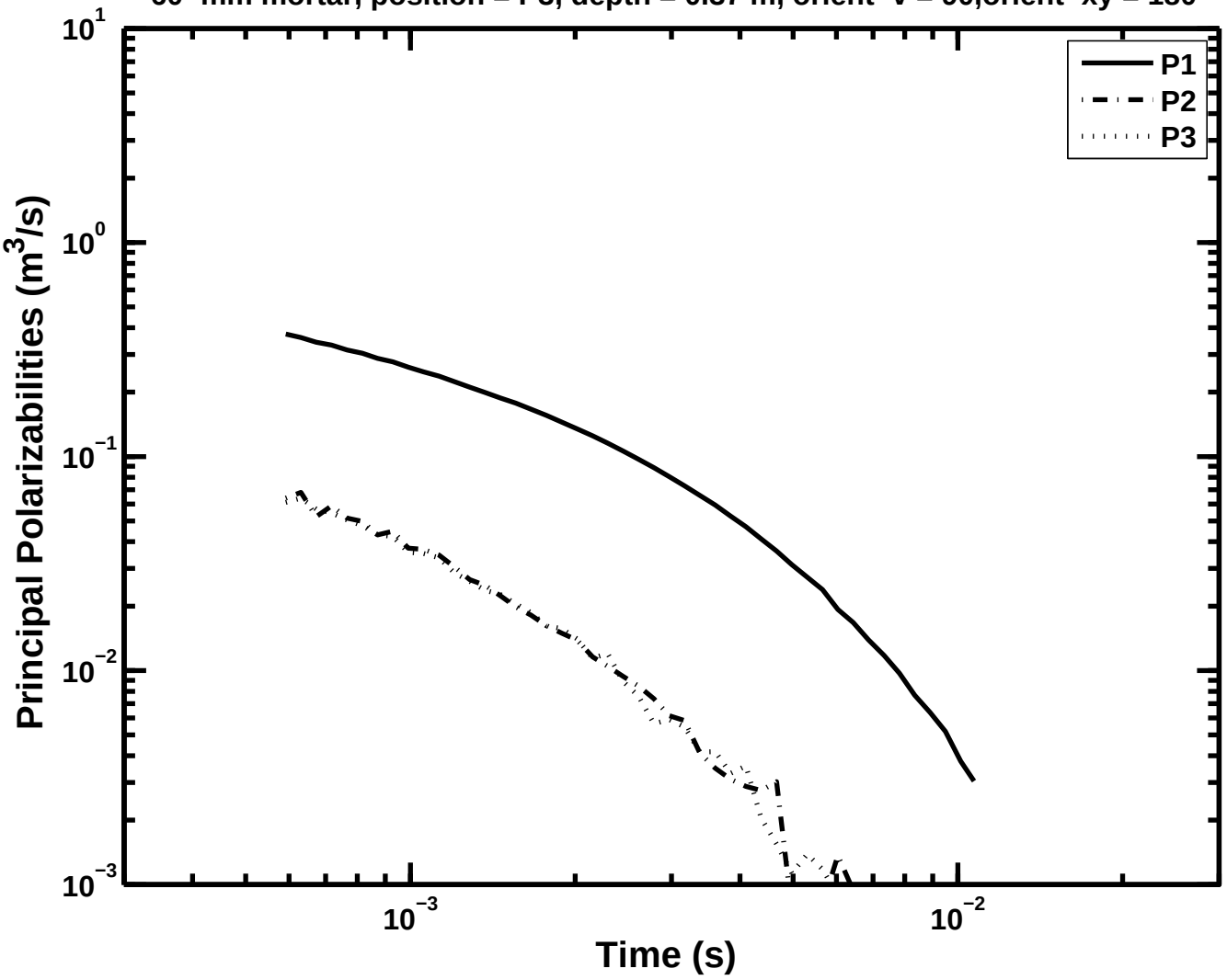

Figure A1−61: Principal polarizabilities as a function of time − 60−mm mortar, position = P3, depth = 0.37 m, orient−v = 90,orient−xy = 0

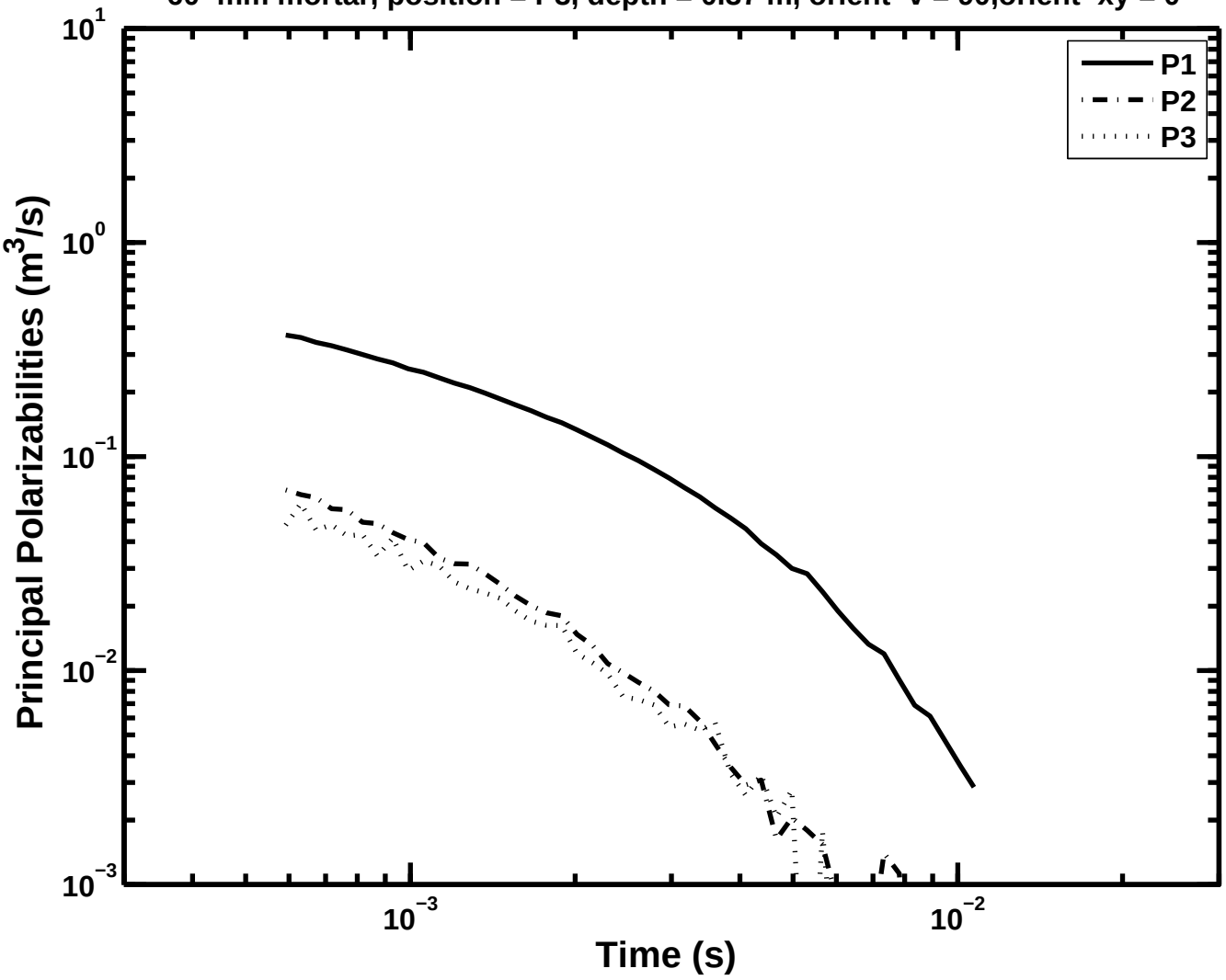

Figure A1−62: Principal polarizabilities as a function of time − 60−mm mortar, position = P3, depth = 0.37 m, orient−v = 90,orient−xy = −90

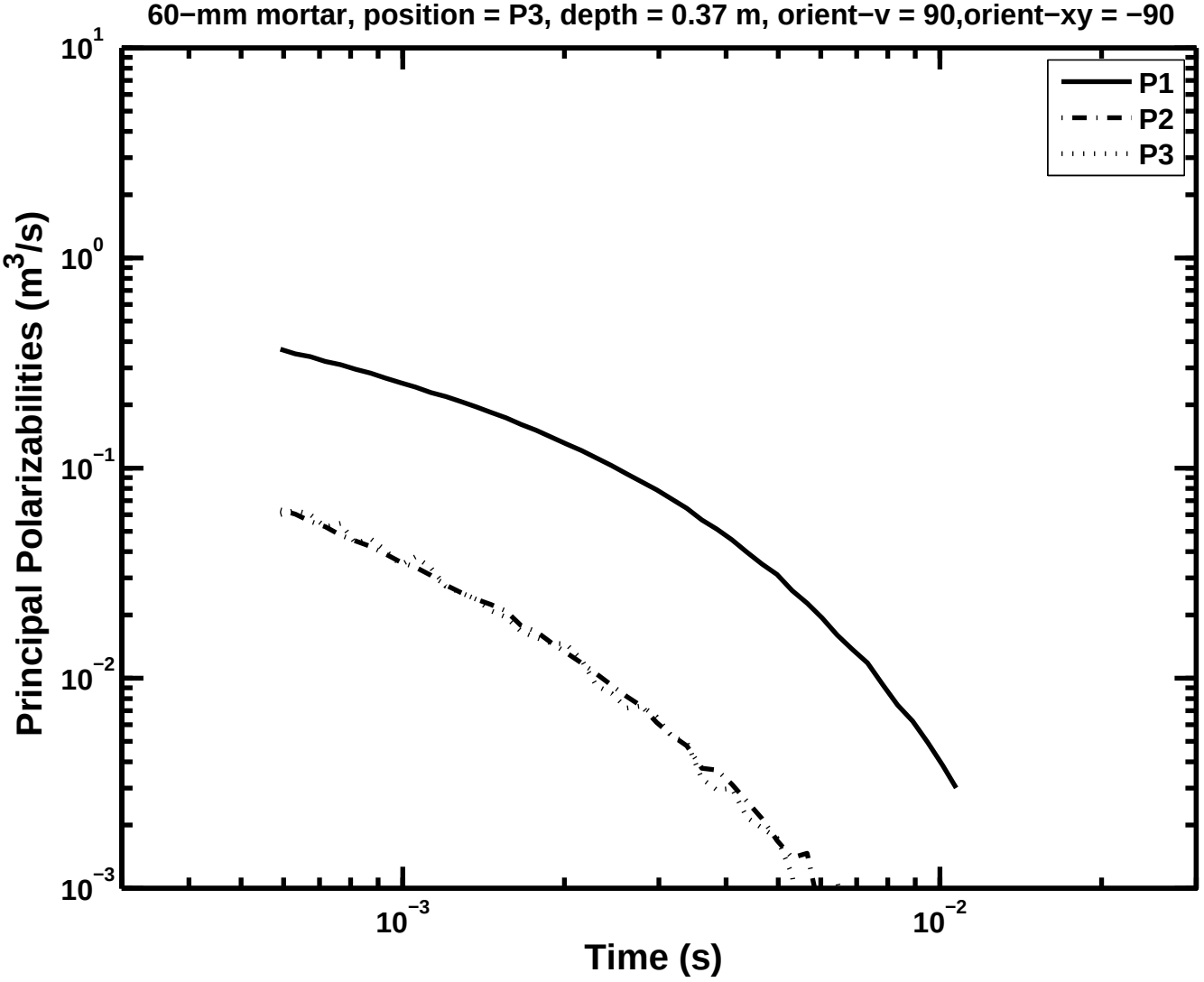

APPENDIX 2

Underwater tests were done at Richmond Marina Yacht Harbor, CA. The data were collected for targets using the following layout. The intermediate plate of the support structure is used to describe object locations. The coordinate system is shown in grey, and (0, 0) is the center of the transmitter cube. Two target positions A and C were used:

A = (0.08; -0.08) m

C = (-0.23; 0.38) m

The target orientation is given with respect to positive z (down), i.e., horizontal is 90° and vertical is 0°.

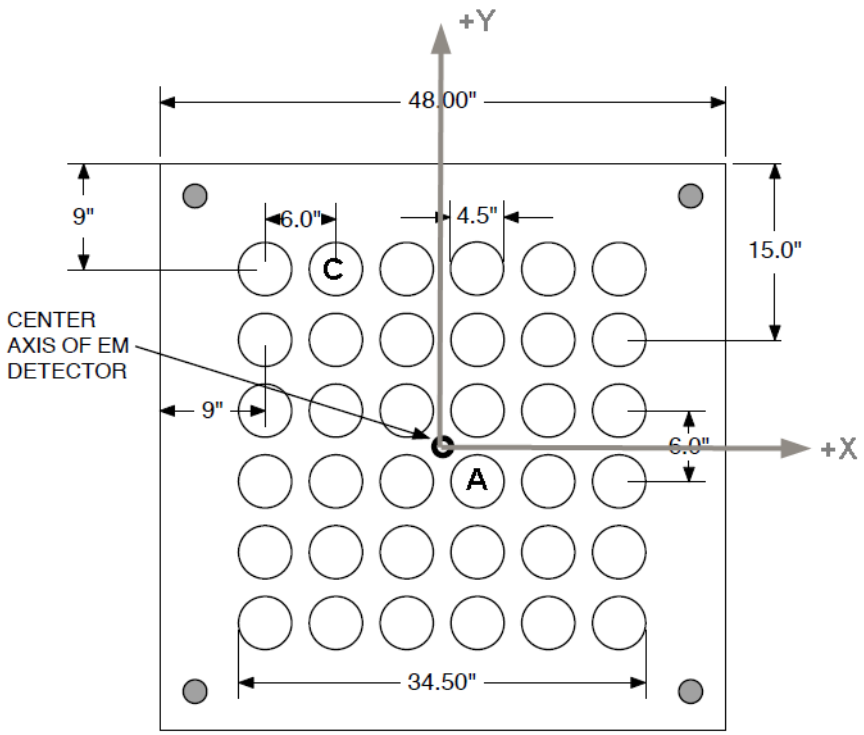

Note: To be consistent with the inversion, which estimates the depth to the center of the object, the actual depth of known objects is also given to the object center. For irregular objects or scrap a distance to the plate holding the target is given instead, which results in a larger discrepancy between actual and estimated depths.

Table 2. Underwater tests - actual targets placements, and inversion estimated horizontal position, depth, orientation, and polarizability index of the targets. Polarizability responses are plotted in Figures listed in the first column.

Figure number	Target	Actual			Inversion Estimates				
		Position	Depth(m)	Orient-v	X(m)	Y(m)	Depth(m)	P-index	Orient-v
Figure A2-1	anchor 2	A	0.5*	N/A	0.09	-0.07	0.55	285	9
Figure A2-2	anchor 2	C	0.5*	N/A	-0.24	0.38	0.52	244	13
Figure A2-3	scrap of metal	A	0.5*	N/A	0.09	-0.07	0.47	164	100
Figure A2-4	scrap of metal	C	0.5*	N/A	-0.23	0.42	0.45	138	104
Figure A2-5	scrap of metal-r2	C	0.5*	N/A	-0.23	0.39	0.5	144	32
Figure A2-6	6-in shotput	A	0.42	90	0.08	-0.07	0.43	226	83
Figure A2-7	6-in shotput	A	0.92	90	0.07	-0.09	0.93	270	69
Figure A2-8	9-in steel spheroid	A	0.45	90	0.06	-0.08	0.45	81	81
Figure A2-9	9-in steel spheroid	A	0.45	90	0.07	-0.09	0.46	88	86
Figure A2-10	9-in steel spheroid	A	0.45	90	0.07	-0.06	0.44	134	92
Figure A2-11	9-in steel spheroid	A	0.45	0	0.08	-0.07	0.47	144	2
Figure A2-12	105-mm projectile	A	0.8	45	0.24	-0.09	0.83	877	44
Figure A2-13	105-mm projectile	A	0.95	90	0.07	-0.05	0.91	756	88
Figure A2-14	105-mm projectile	A	1.0	0	0.08	-0.07	1.05	1208	11
Figure A2-15	105-mm projectile	A	0.5	90	0.07	-0.05	0.45	909	91
Figure A2-16	105-mm projectile	A	0.5	0	0.08	-0.07	0.54	900	1
Figure A2-17	105-mm projectile	C	0.45	90	-0.23	0.43	0.45	1005	91
Figure A2-18	2.75-in rocket	A	0.9	30	0.15	-0.05	0.94	379	149
Figure A2-19	2.75-in rocket	A	0.96	90	0.09	-0.08	0.95	370	92
Figure A2-20	2.75-in rocket	A	0.46	90	0.07	-0.07	0.45	353	90
Figure A2-21	60-mm mortar	A	0.47	90	0.08	-0.11	0.45	73	93
Figure A2-22	60-mm mortar	A	0.47	0	0.08	-0.06	0.43	85	3
Figure A2-23	60-mm mortar	C	0.47	90	-0.23	0.35	0.46	79	93
* distance to the plate holding the target									

Figure A2−1: Principal polarizabilities as a function of time − anchor2, position = A, depth = 0.5 m, orientation = N/A

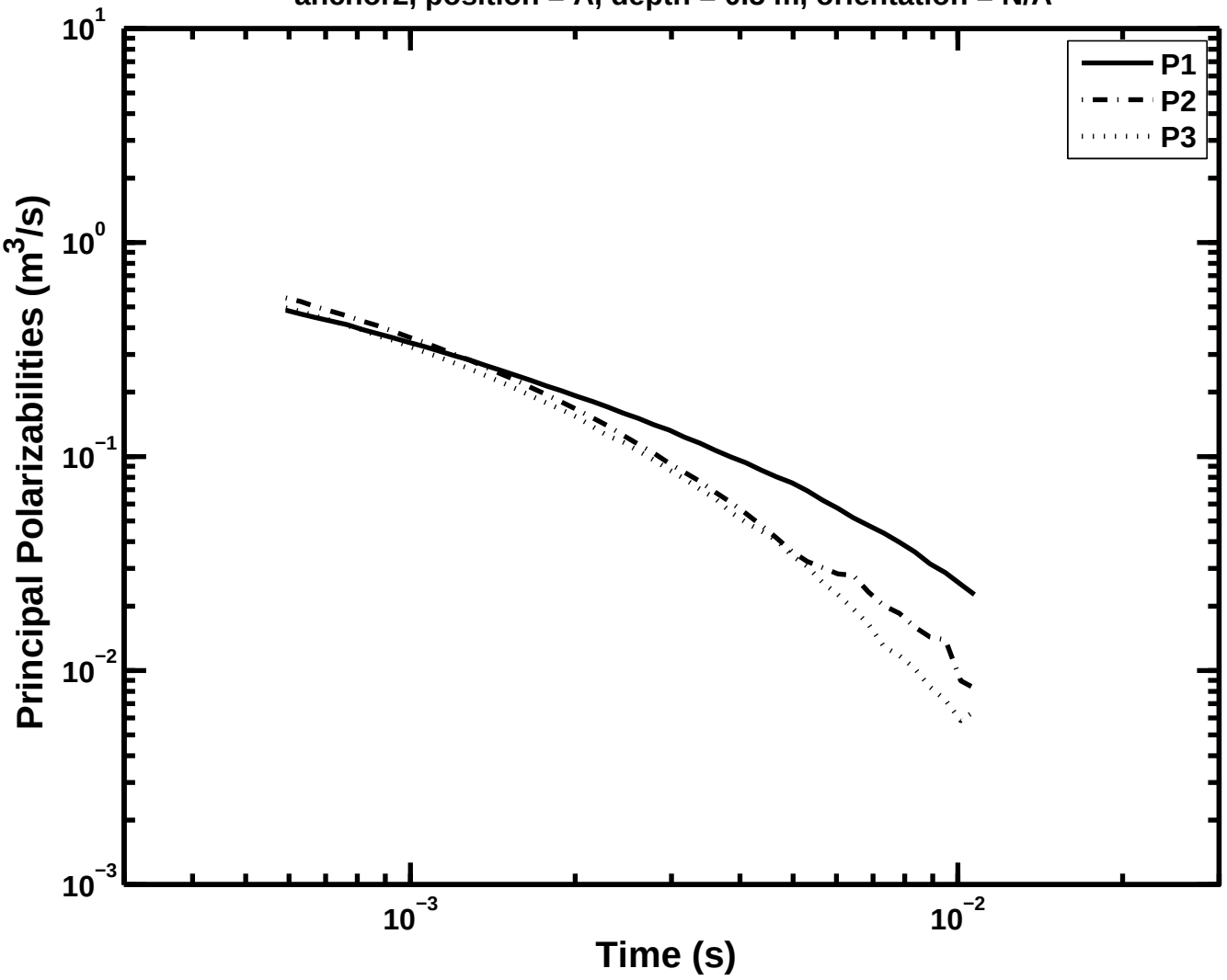

Figure A2−2: Principal polarizabilities as a function of time − anchor2, position = C, depth = 0.5 m, orientation = N/A

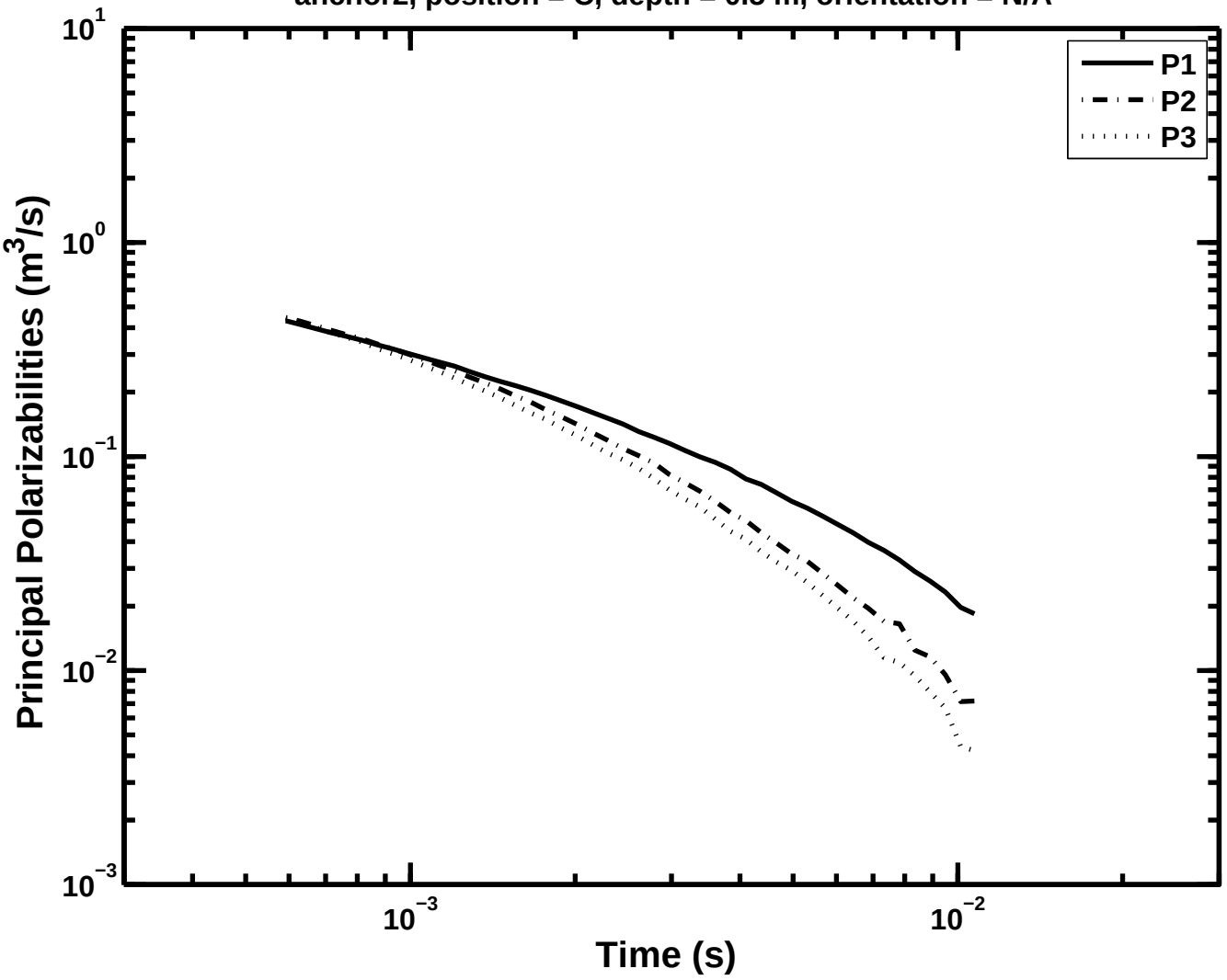

Figure A2−3: Principal polarizabilities as a function of time − scrap, position = A, depth = 0.5 m, orientation = N/A

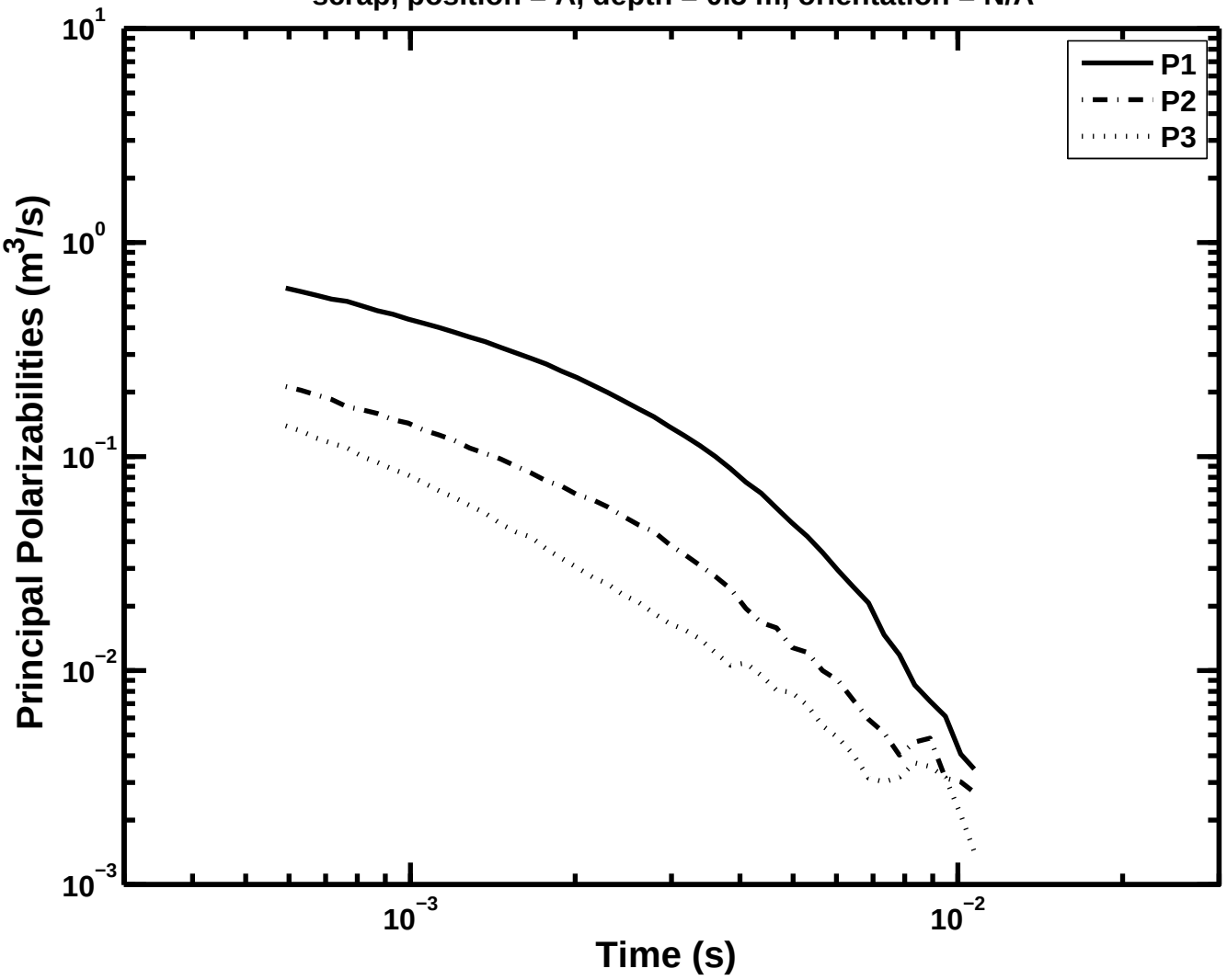

Figure A2−4: Principal polarizabilities as a function of time − scrap, position = C, depth = 0.5 m, orientation = N/A

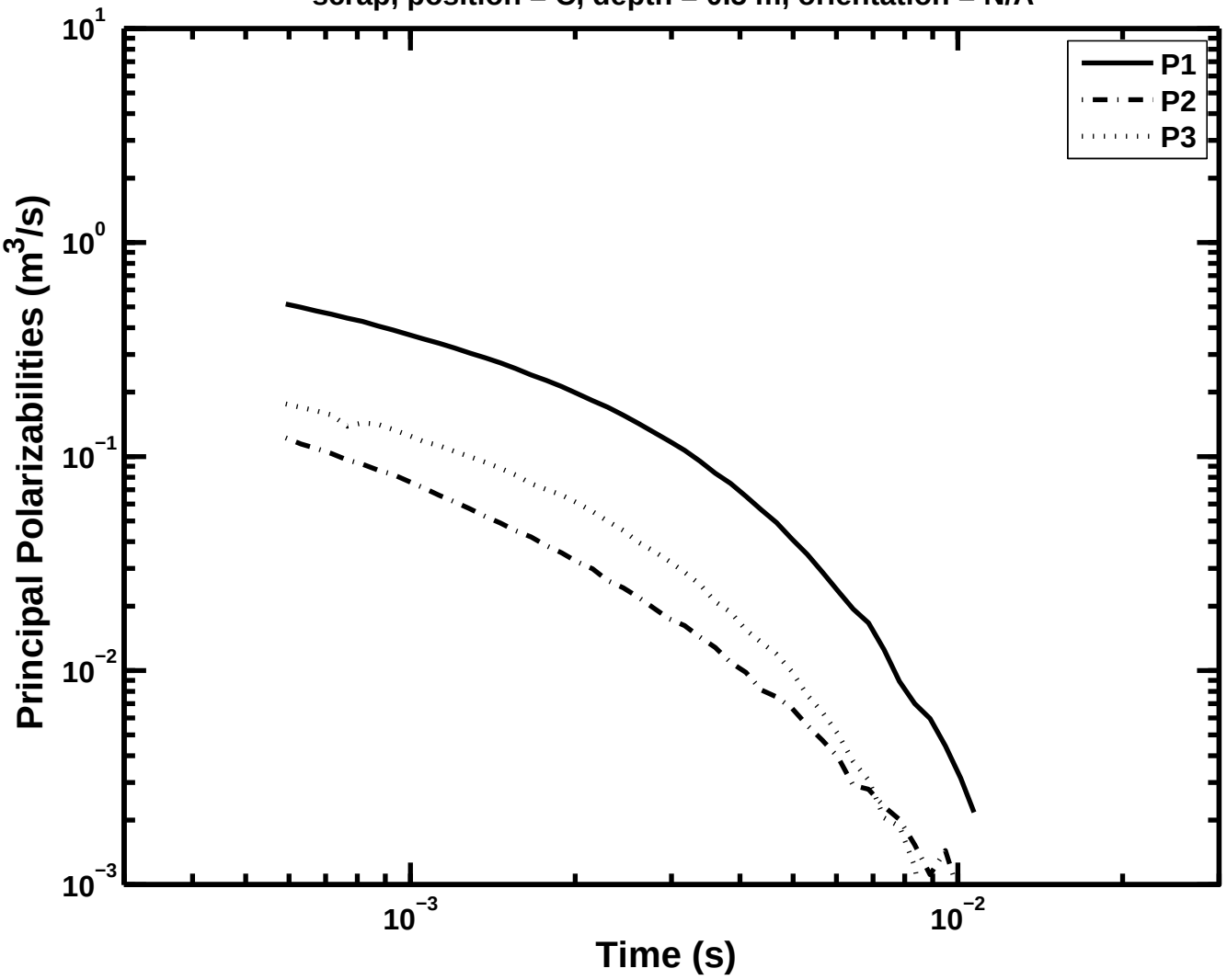

Figure A2−5: Principal polarizabilities as a function of time − scrap, position = C, depth = 0.5 m, orientation = N/A, rotated 90 deg

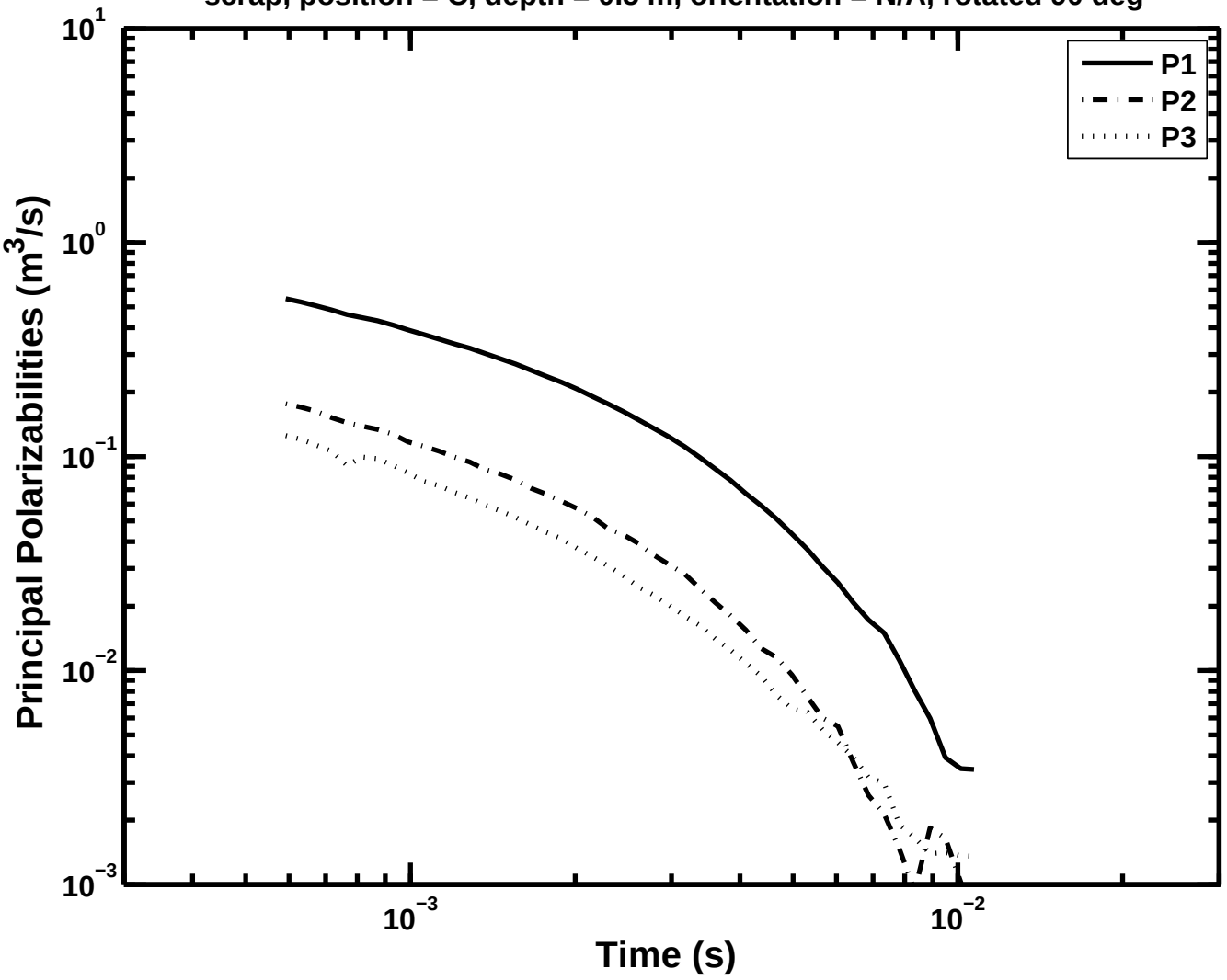

Figure A2−6: Principal polarizabilities as a function of time − 6−in shotput, position = A, depth = 0.42 m, orientation = N/A

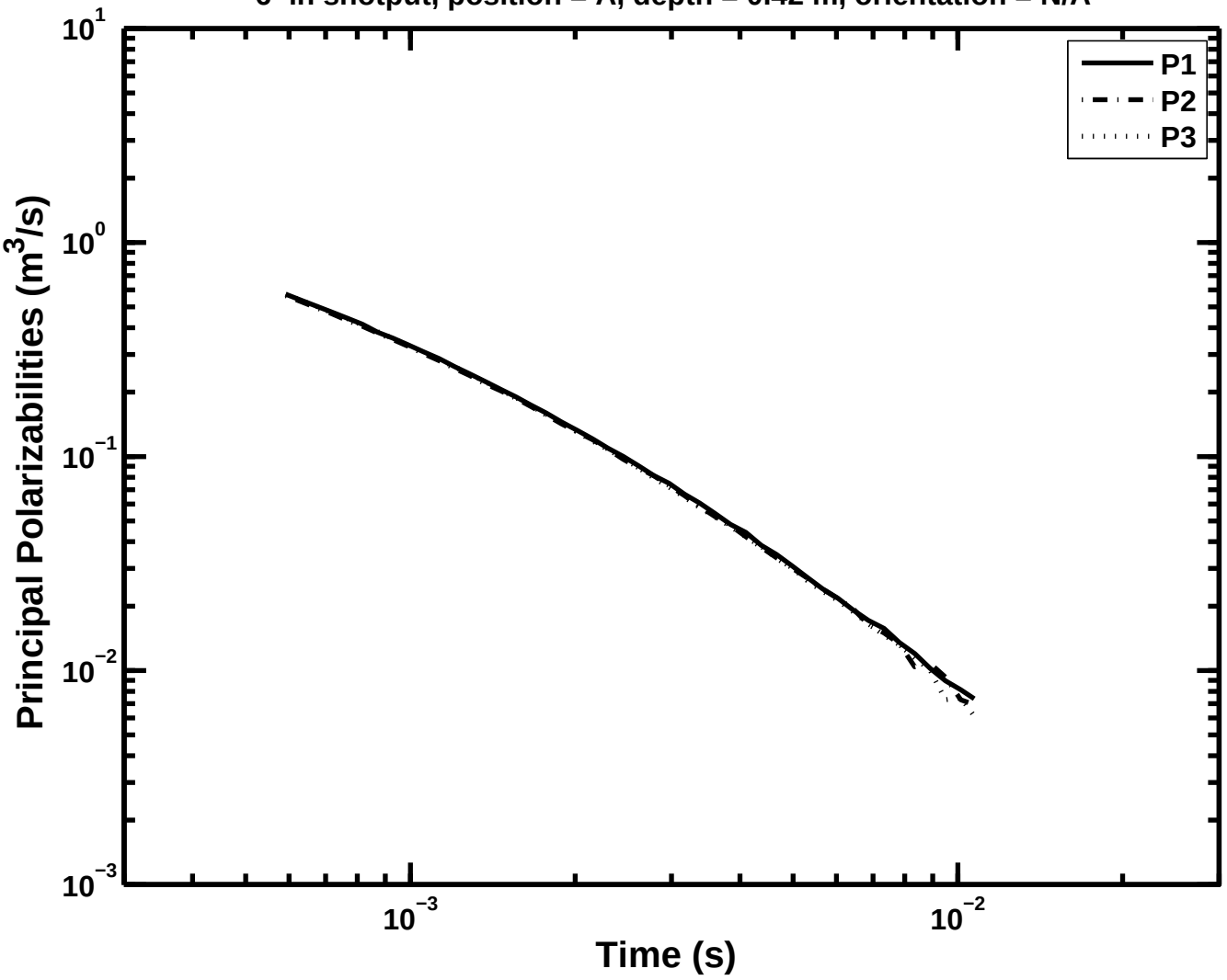

Figure A2−7: Principal polarizabilities as a function of time − 6−in shotput, position = A, depth = 0.92 m, orientation = N/A

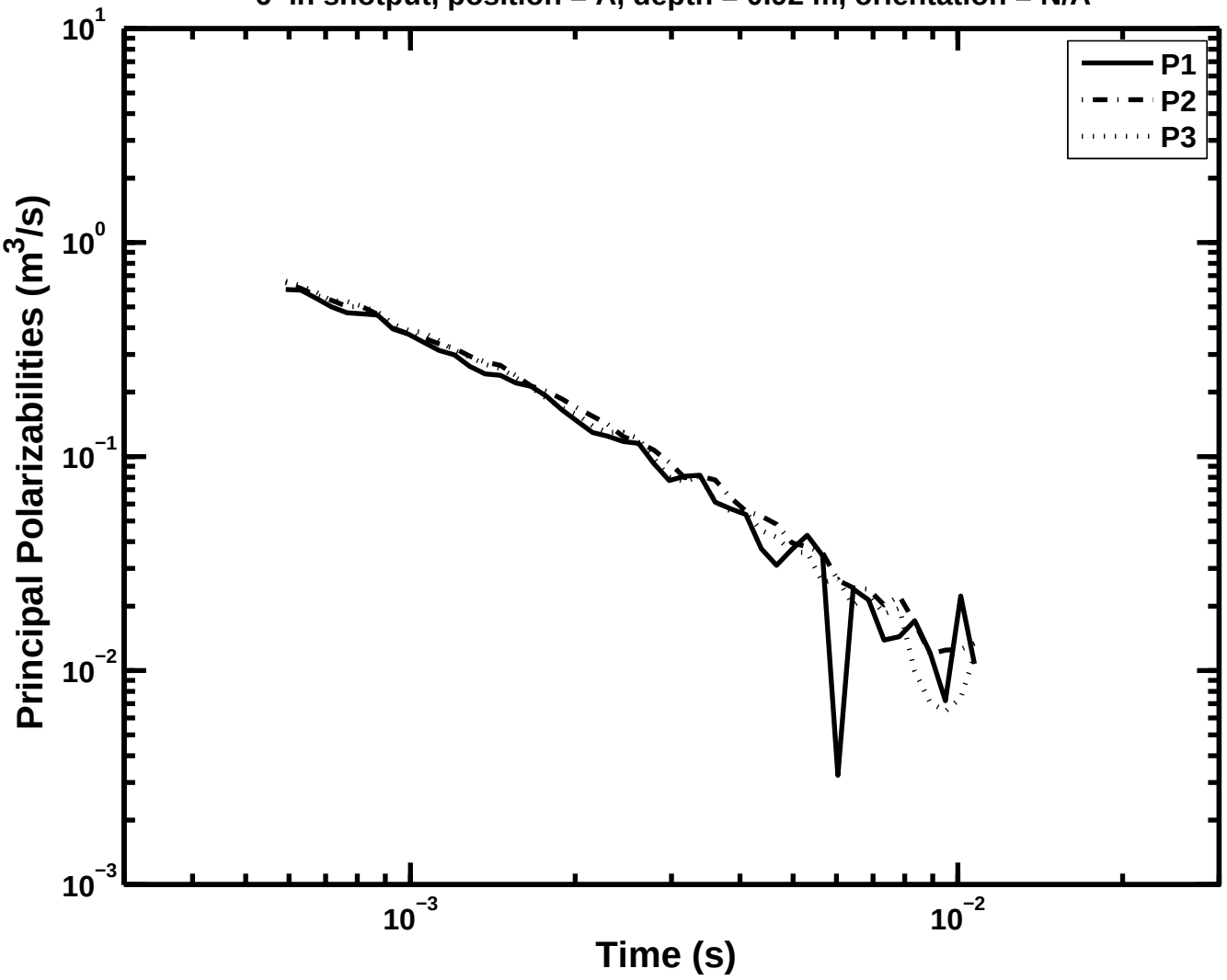

Figure A2−8: Principal polarizabilities as a function of time − 9−in aluminum spheroid, position = A, depth = 0.45 m, orientation = 90

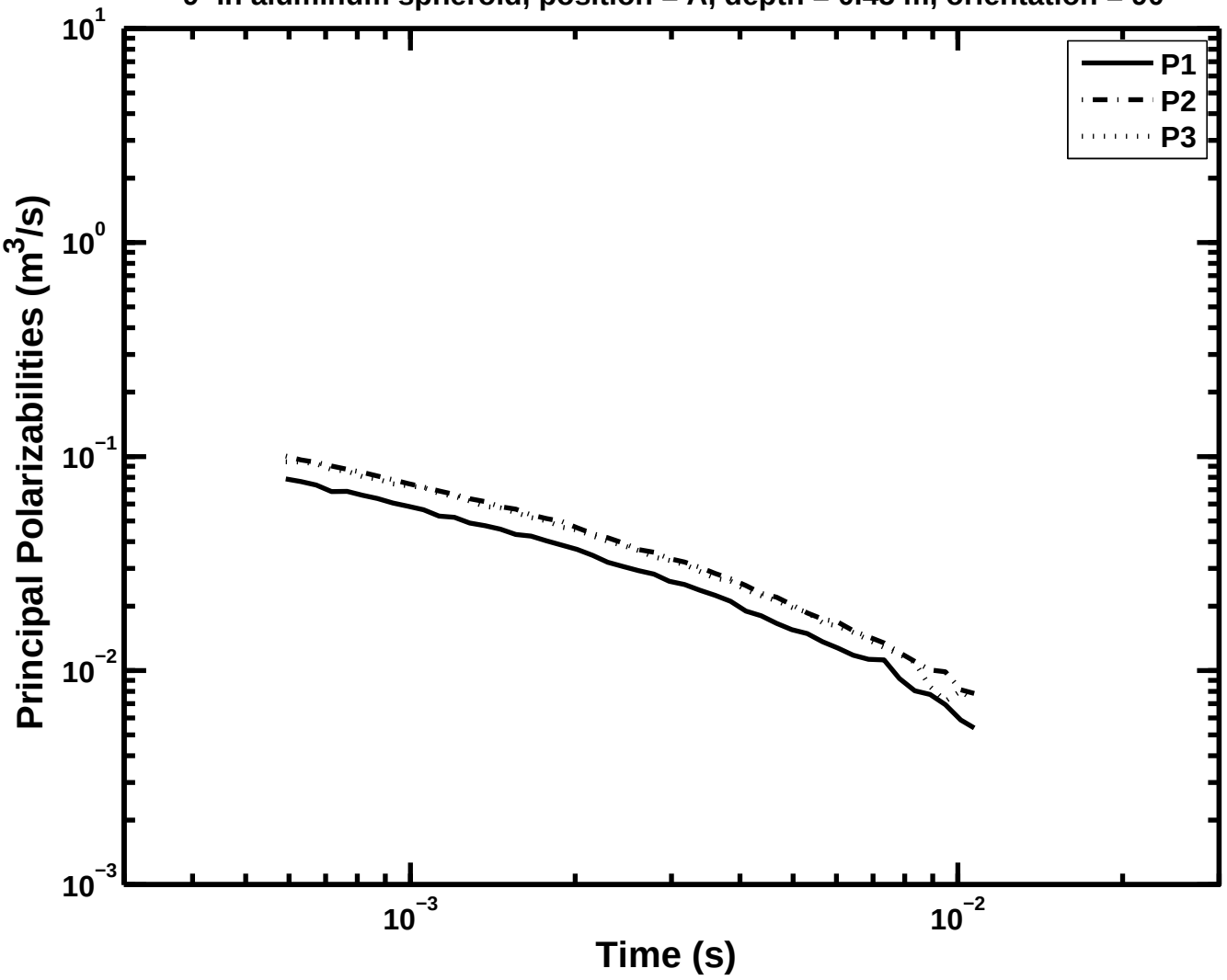

Figure A2−9: Principal polarizabilities as a function of time − 9−in aluminum spheroid, position = A, depth = 0.45 m, orientation = 90

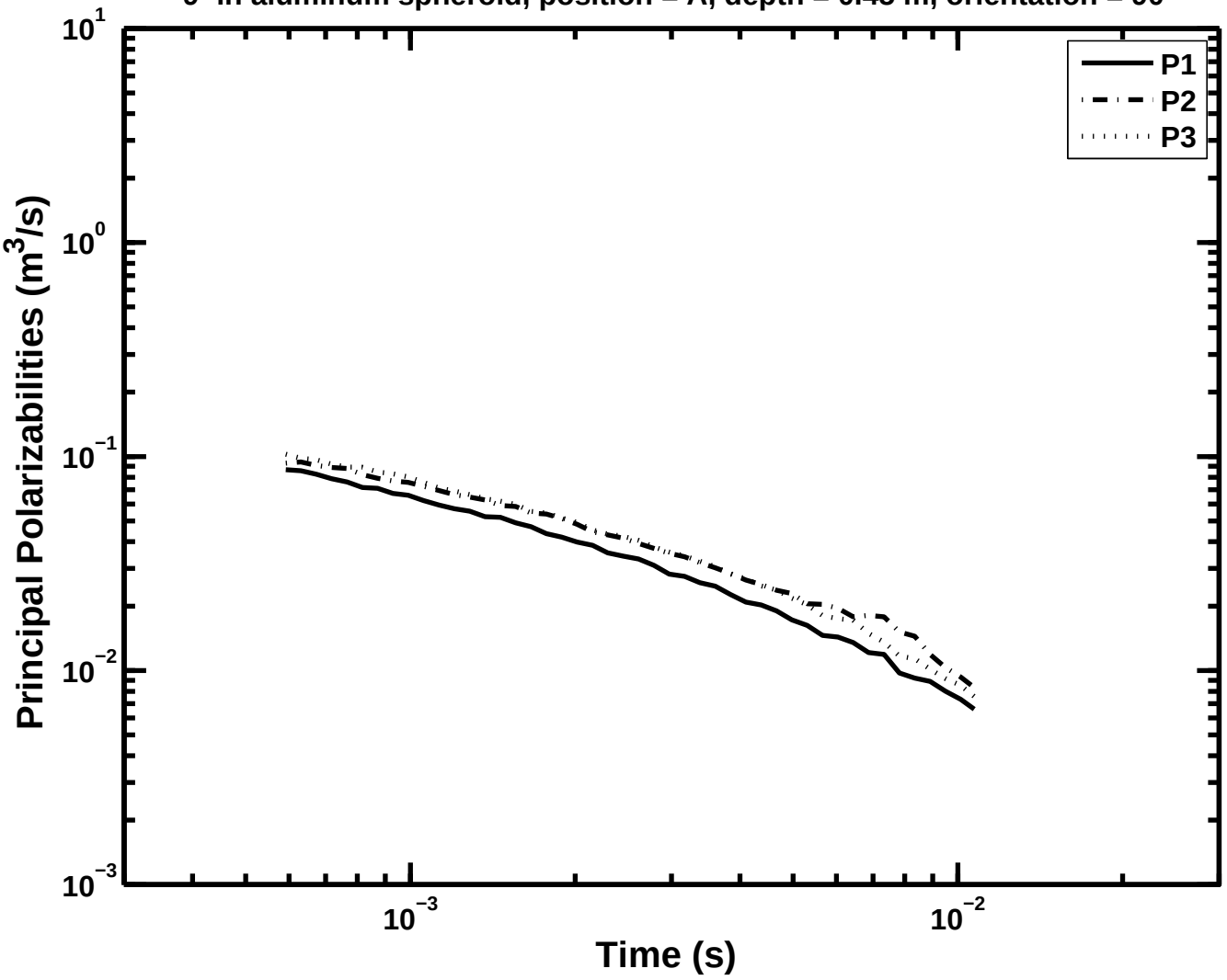

Figure A2−10: Principal polarizabilities as a function of time − 9−in steel spheroid, position = A, depth = 0.45 m, orientation = 90

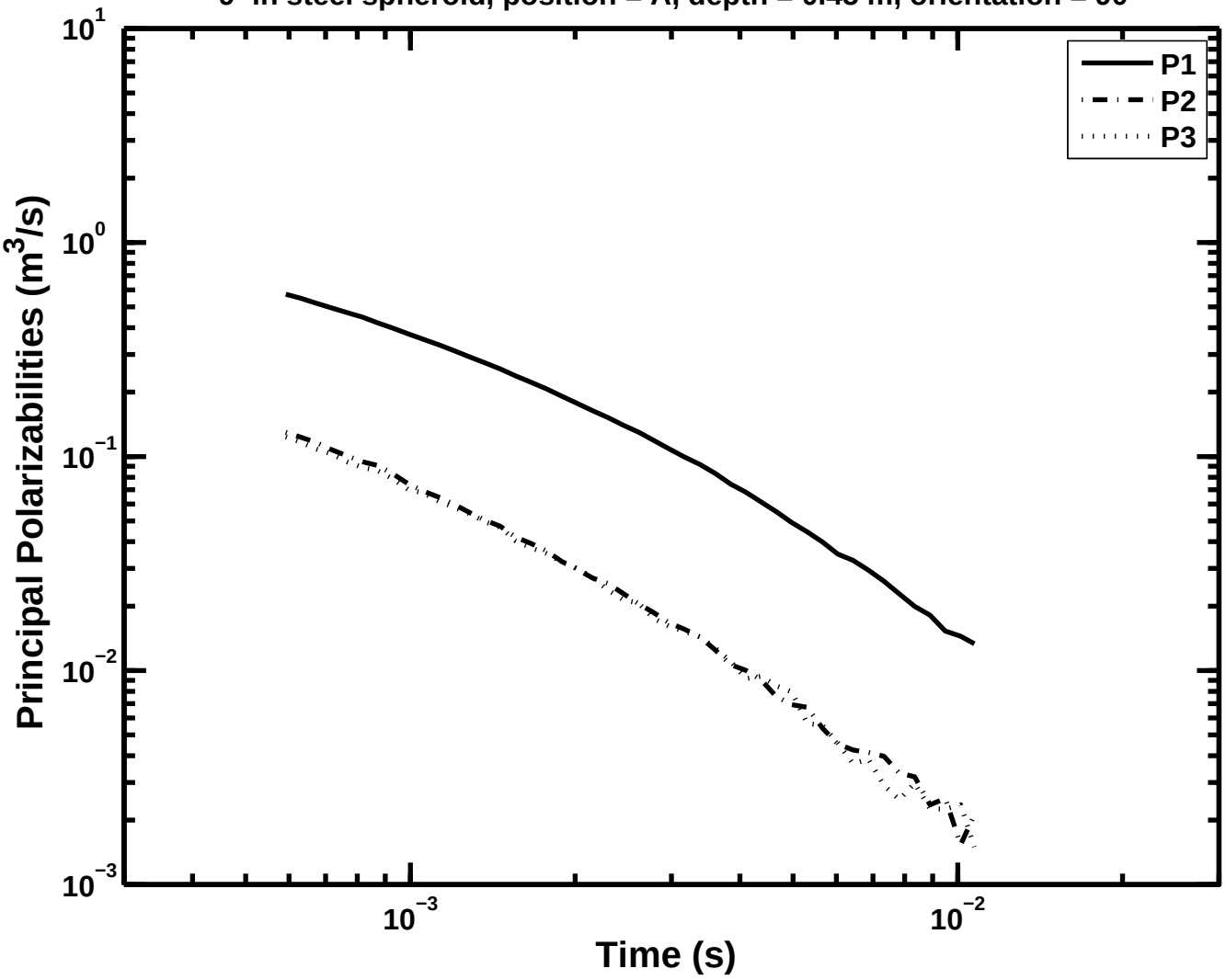

Figure A2−11: Principal polarizabilities as a function of time − 9−in steel spheroid, position = A, depth = 0.45 m, orientation = 0

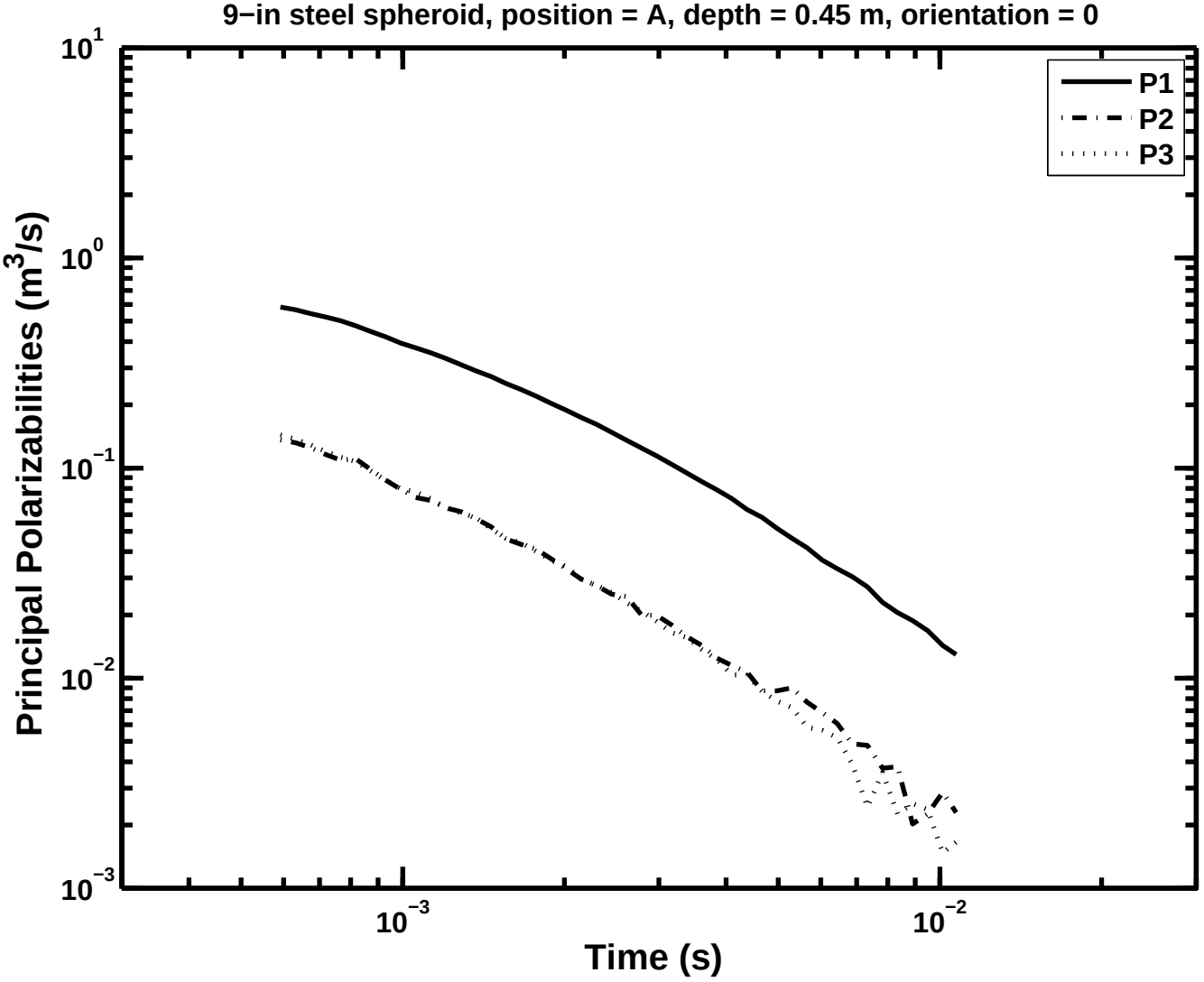

Figure A2−12: Principal polarizabilities as a function of time − 105−mm projectile, position = A, depth = 0.8 m, orientation = 45

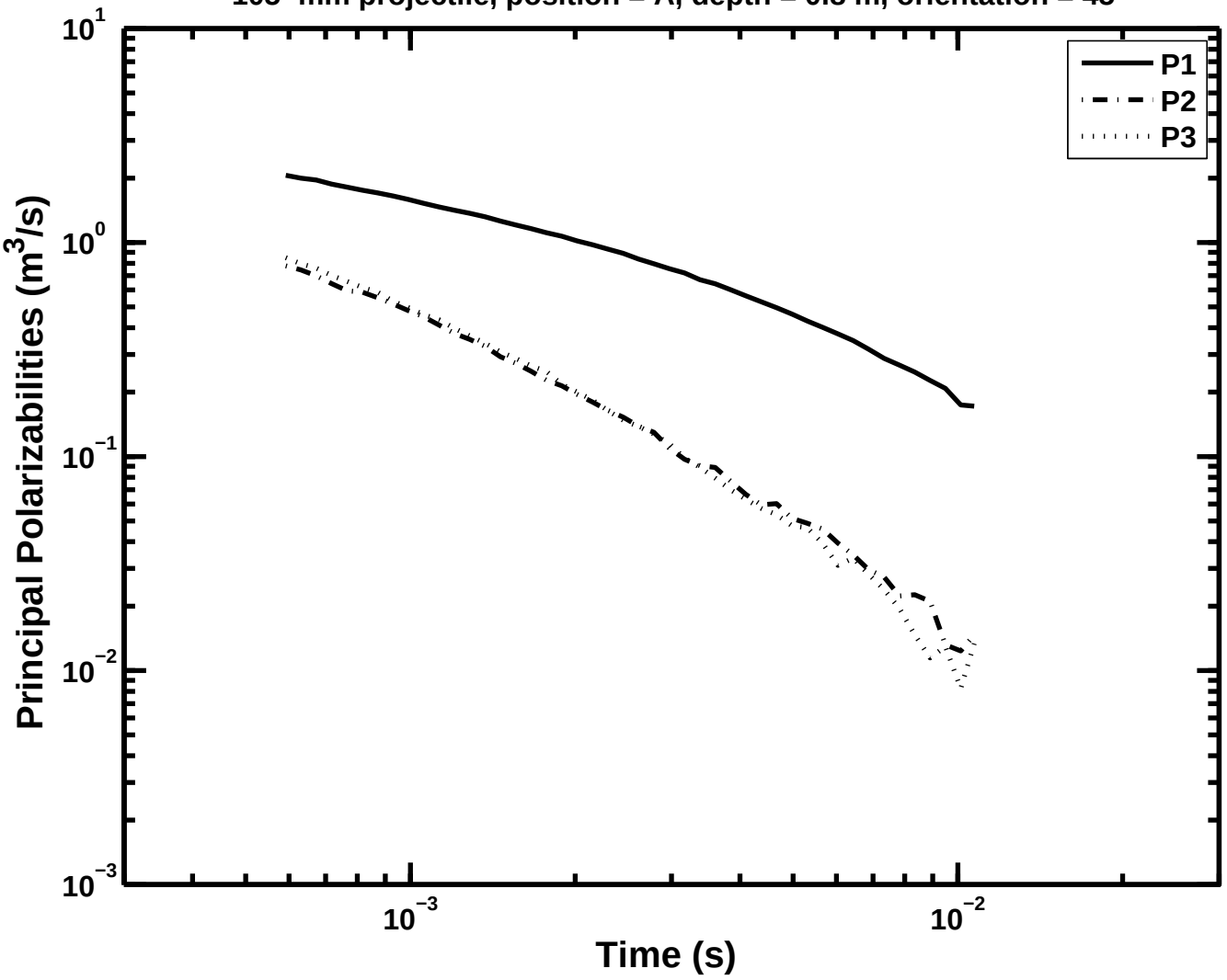

Figure A2−13: Principal polarizabilities as a function of time − 105−mm projectile, position = A, depth = 0.95 m, orientation = 90

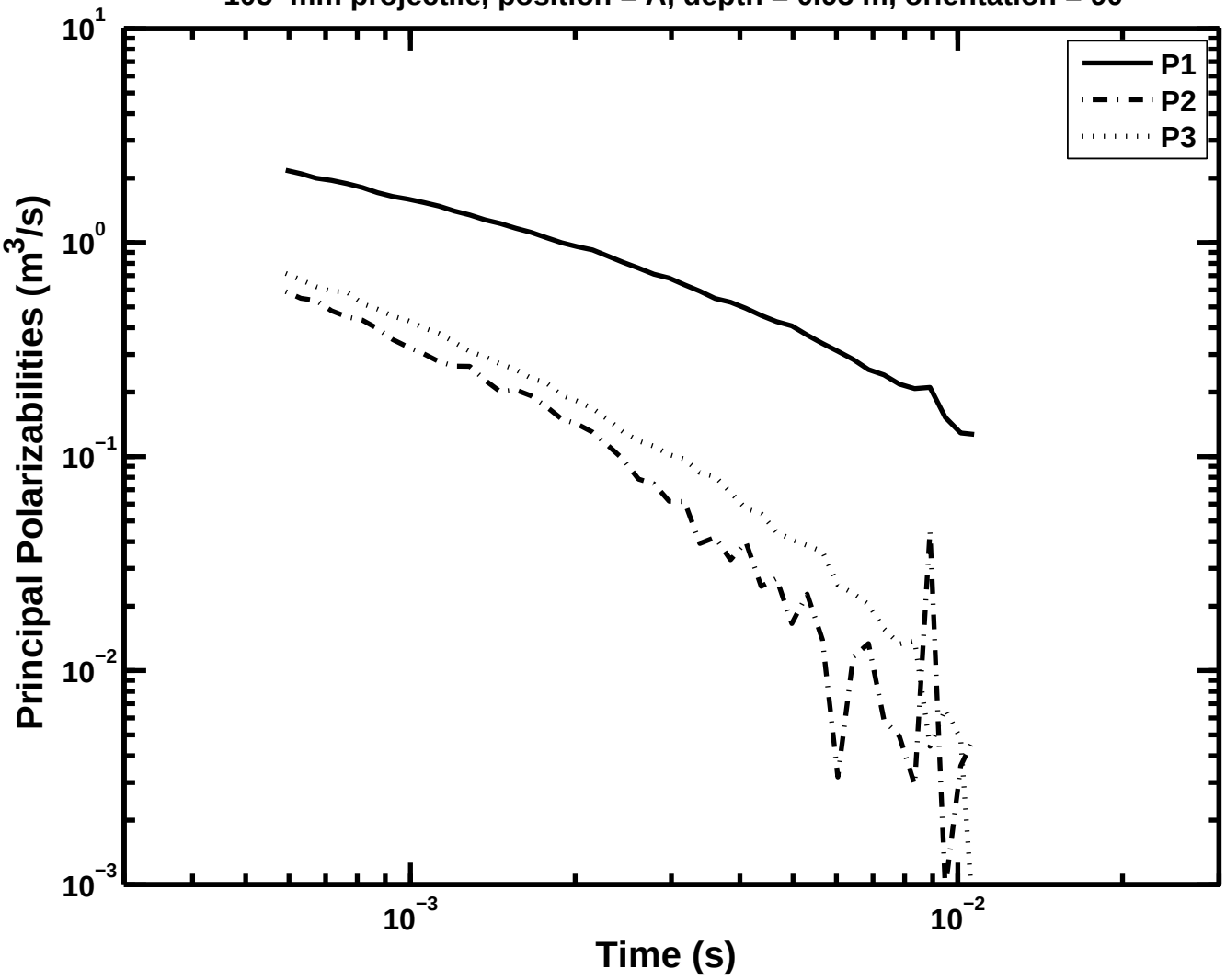

Figure A2−14: Principal polarizabilities as a function of time − 105−mm projectile, position = A, depth = 1.0 m, orientation = 0

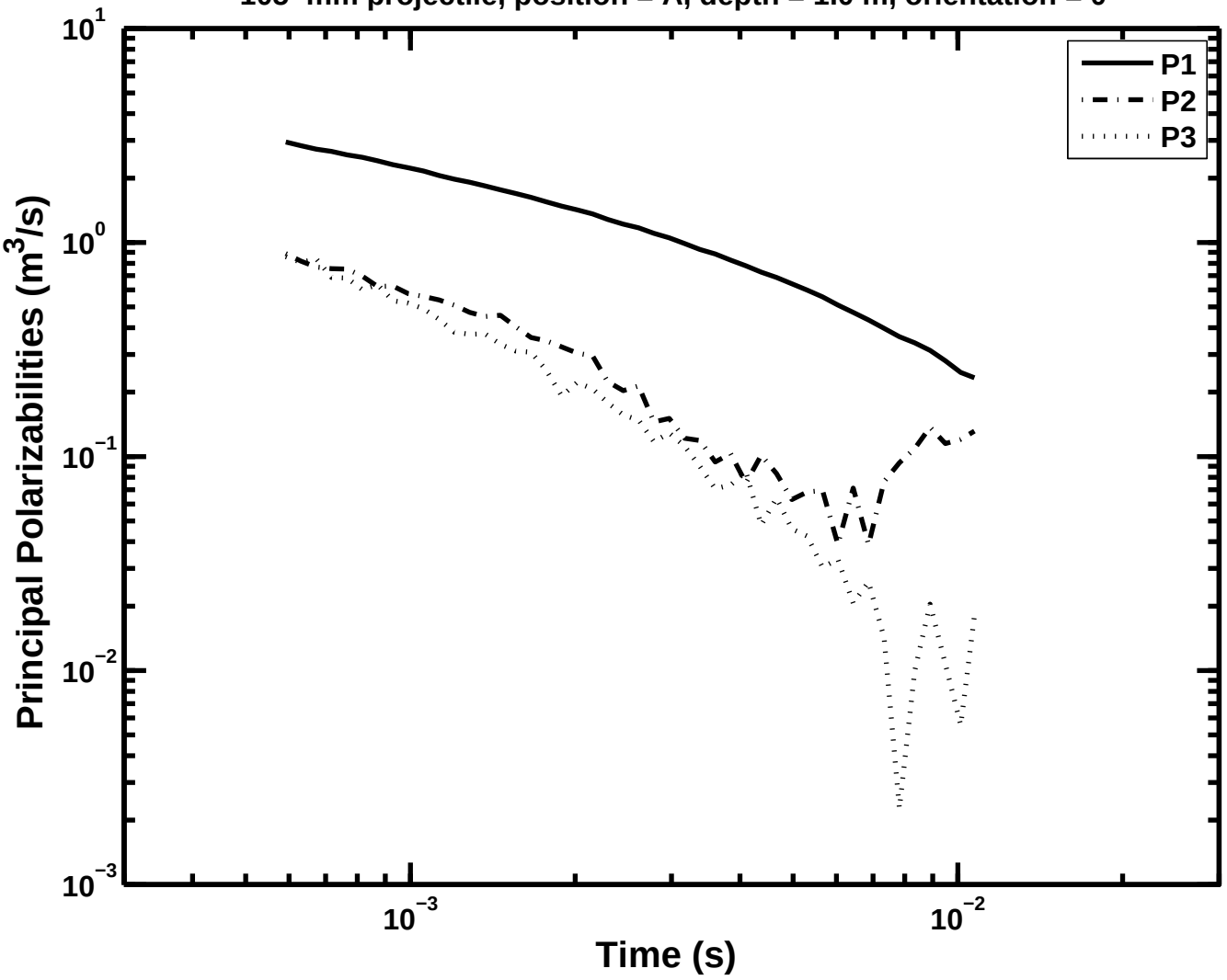

Figure A2−15: Principal polarizabilities as a function of time − 105−mm projectile, position = A, depth = 0.5 m, orientation = 90

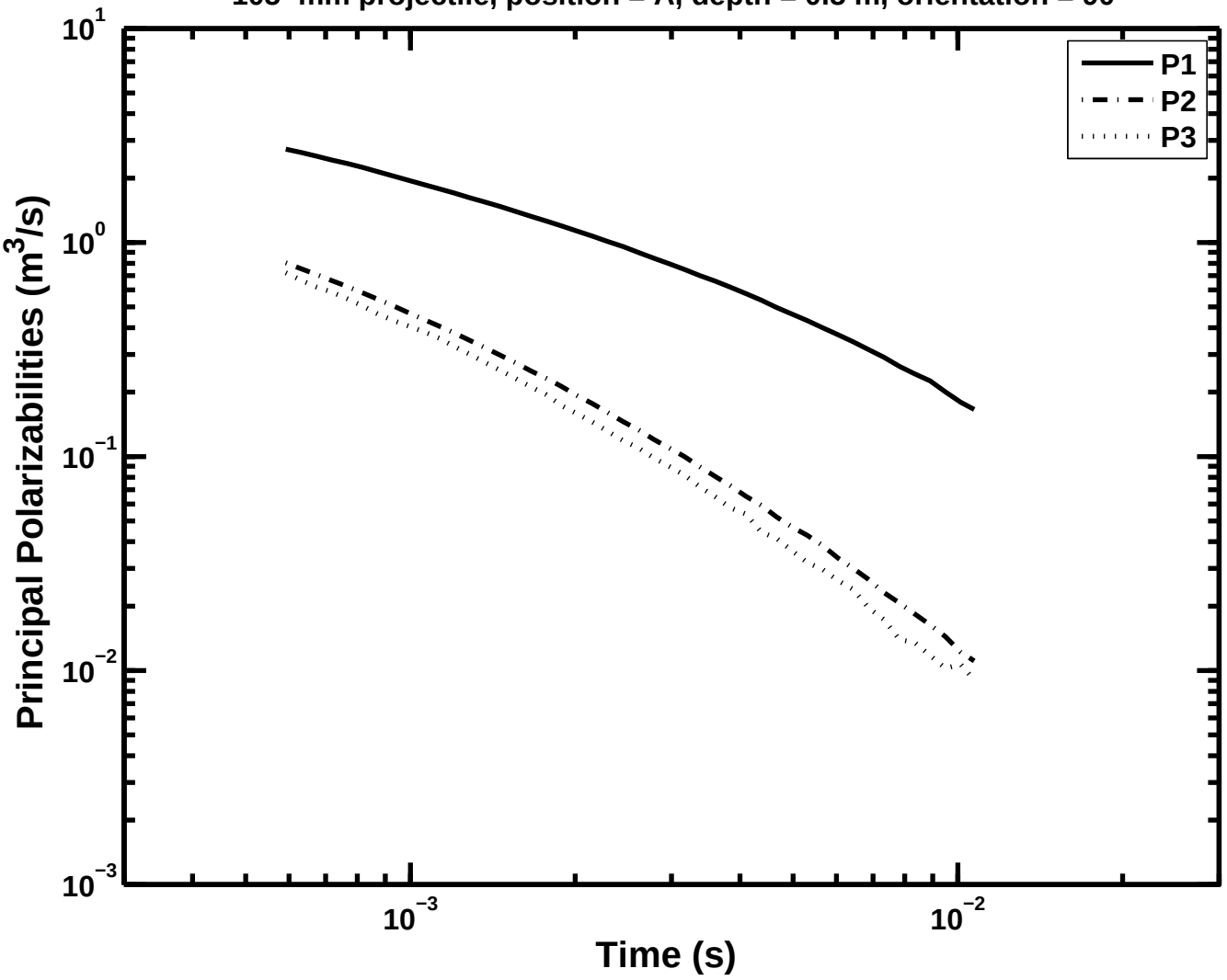

Figure A2−16: Principal polarizabilities as a function of time − 105−mm projectile, position = A, depth = 0.5 m, orientation = 0

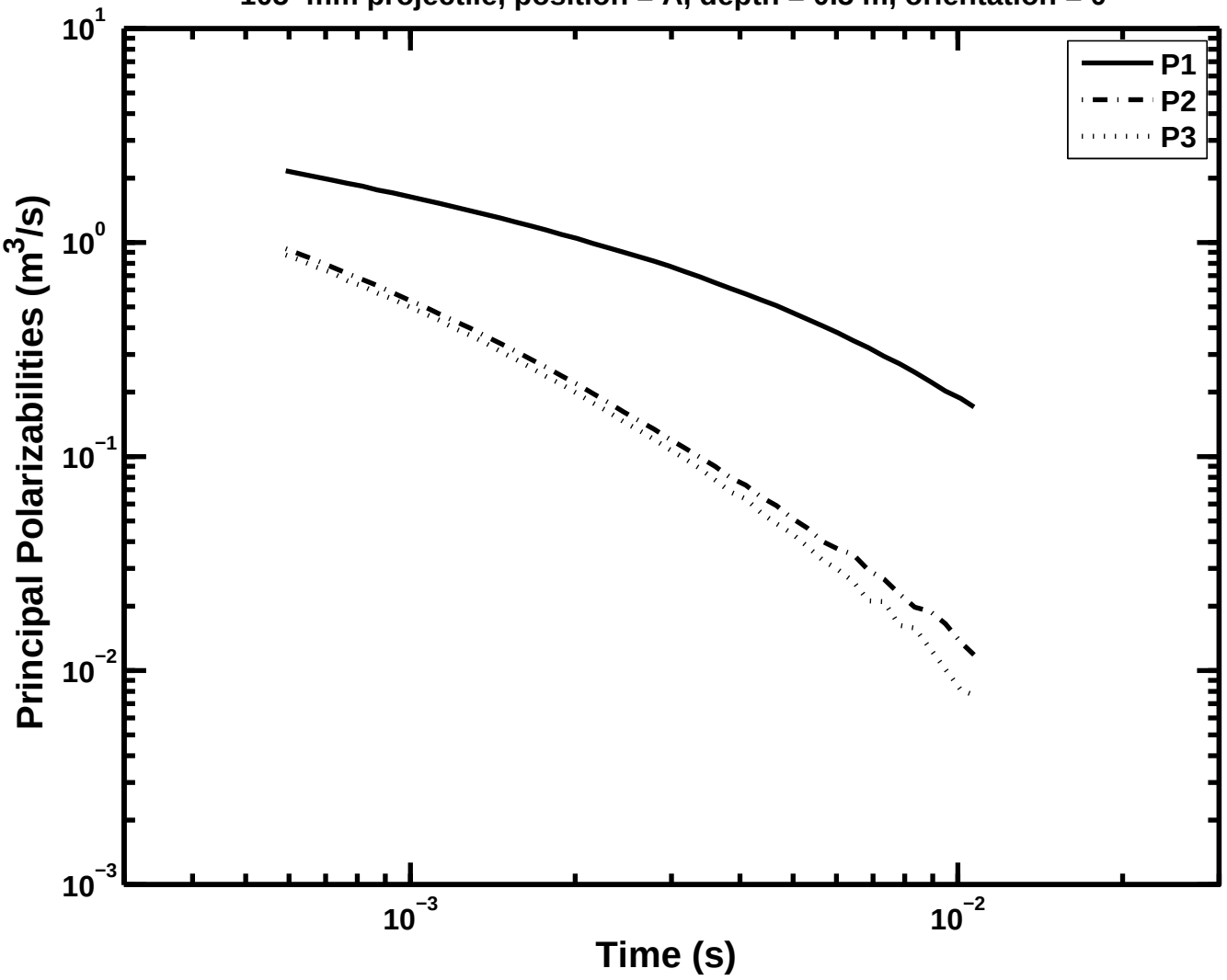

Figure A2−17: Principal polarizabilities as a function of time − 105−mm projectile, position = C, depth = 0.45 m, orientation = 90

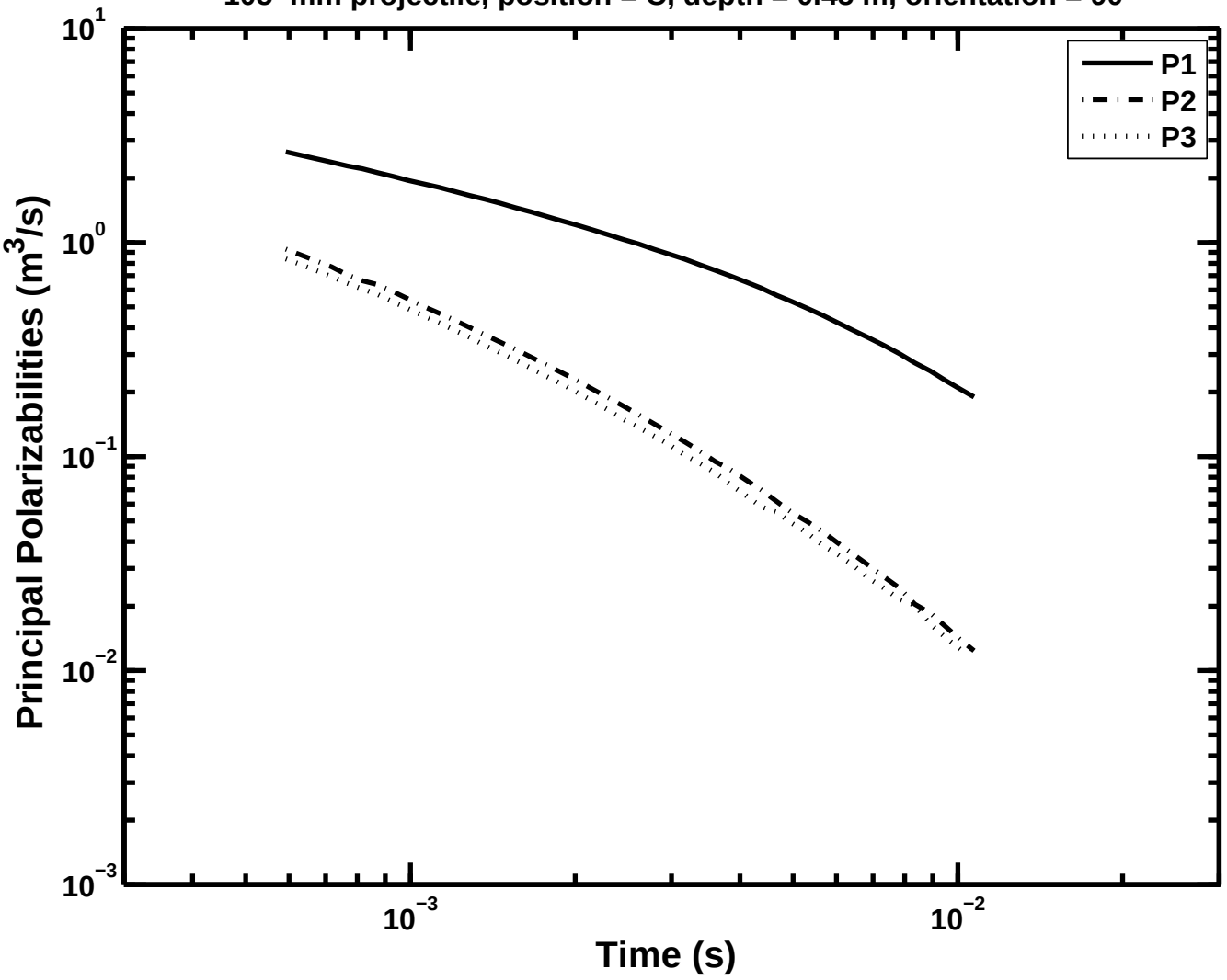

Figure A2−18: Principal polarizabilities as a function of time − 2.75−in rocket, position = A, depth = 0.9 m, orientation = 30

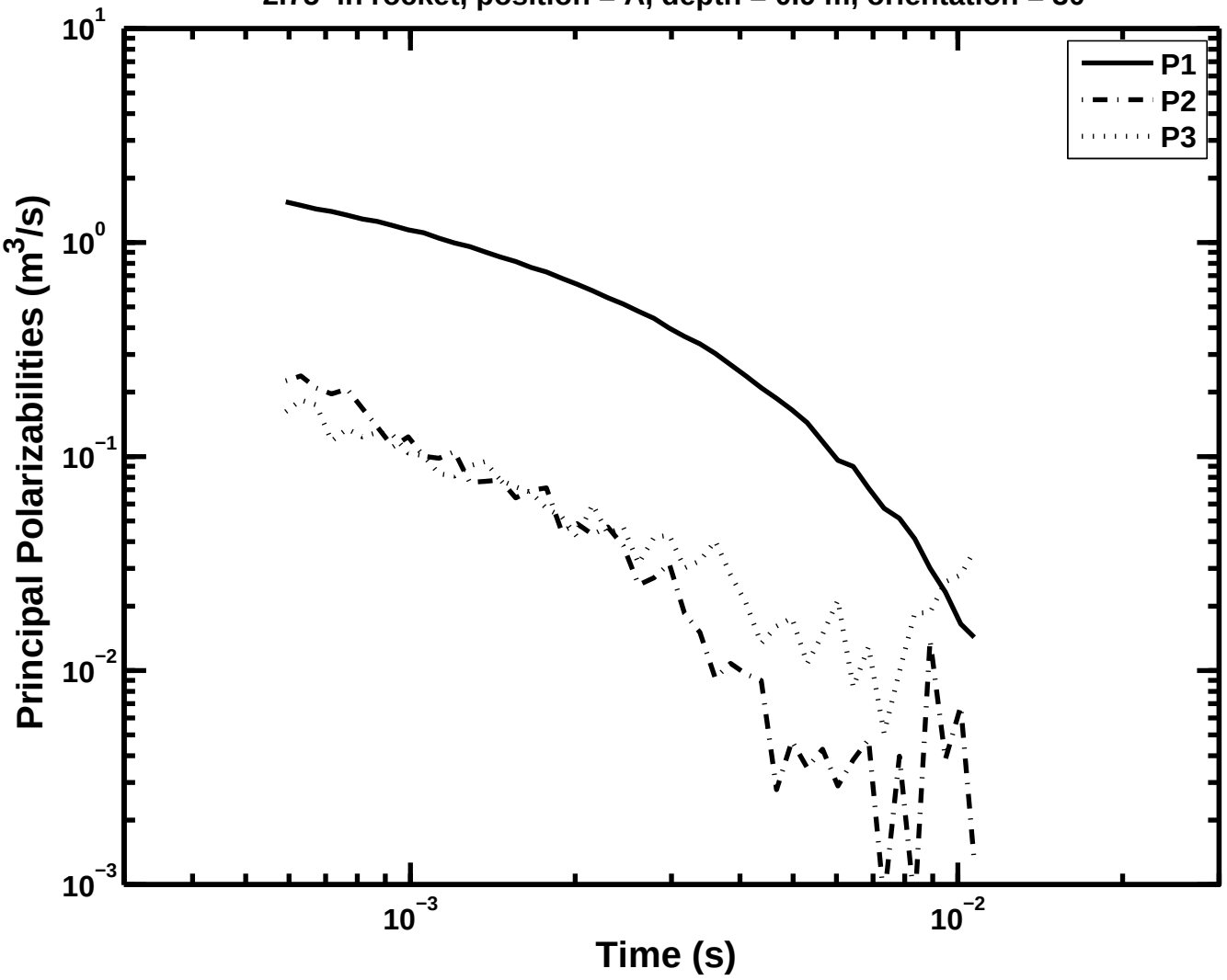

Figure A2−19: Principal polarizabilities as a function of time − 2.75−in rocket, position = A, depth = 0.96 m, orientation = 90

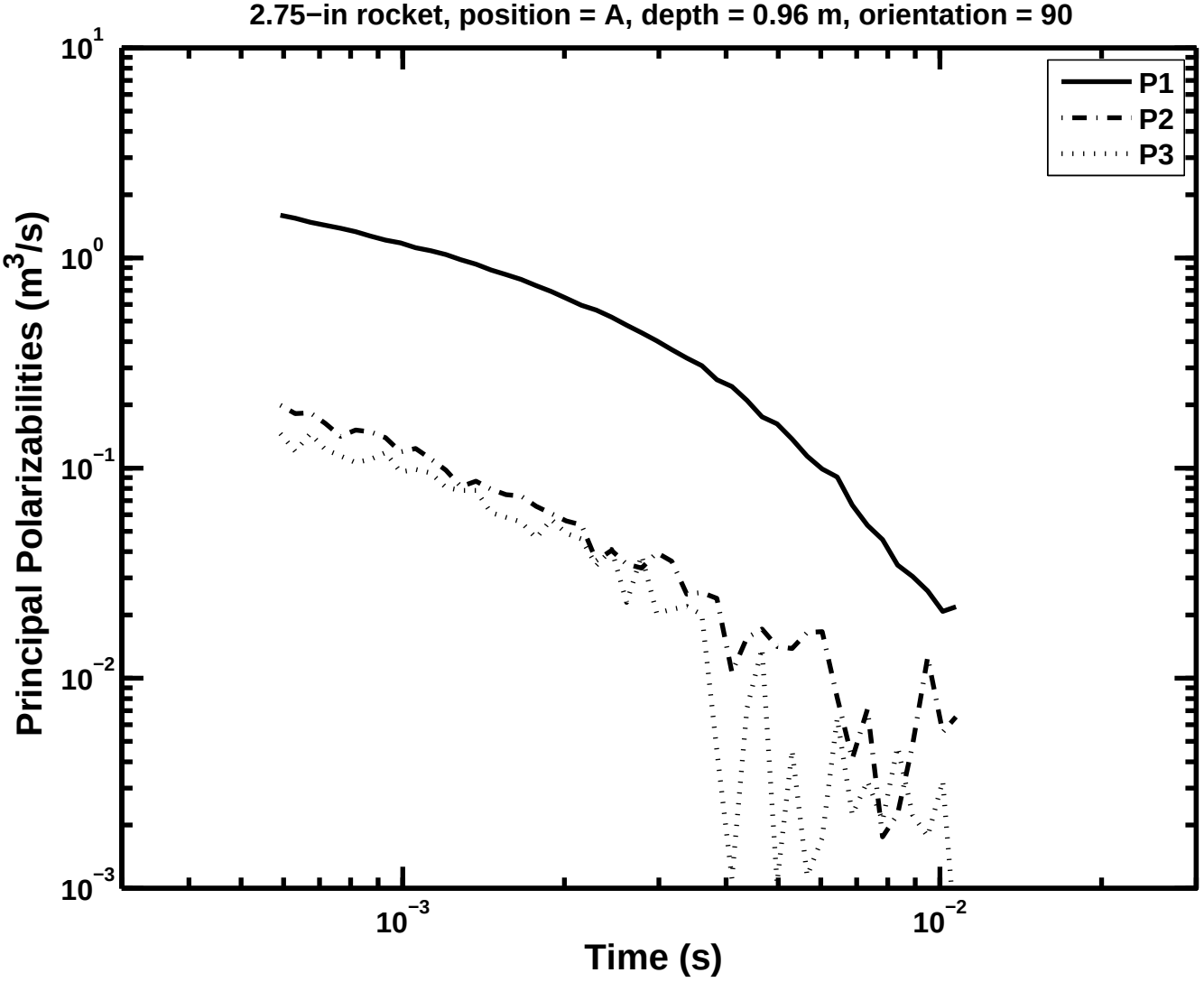

Figure A2−20: Principal polarizabilities as a function of time − 2.75−in rocket, position = A, depth = 0.46 m, orientation = 90

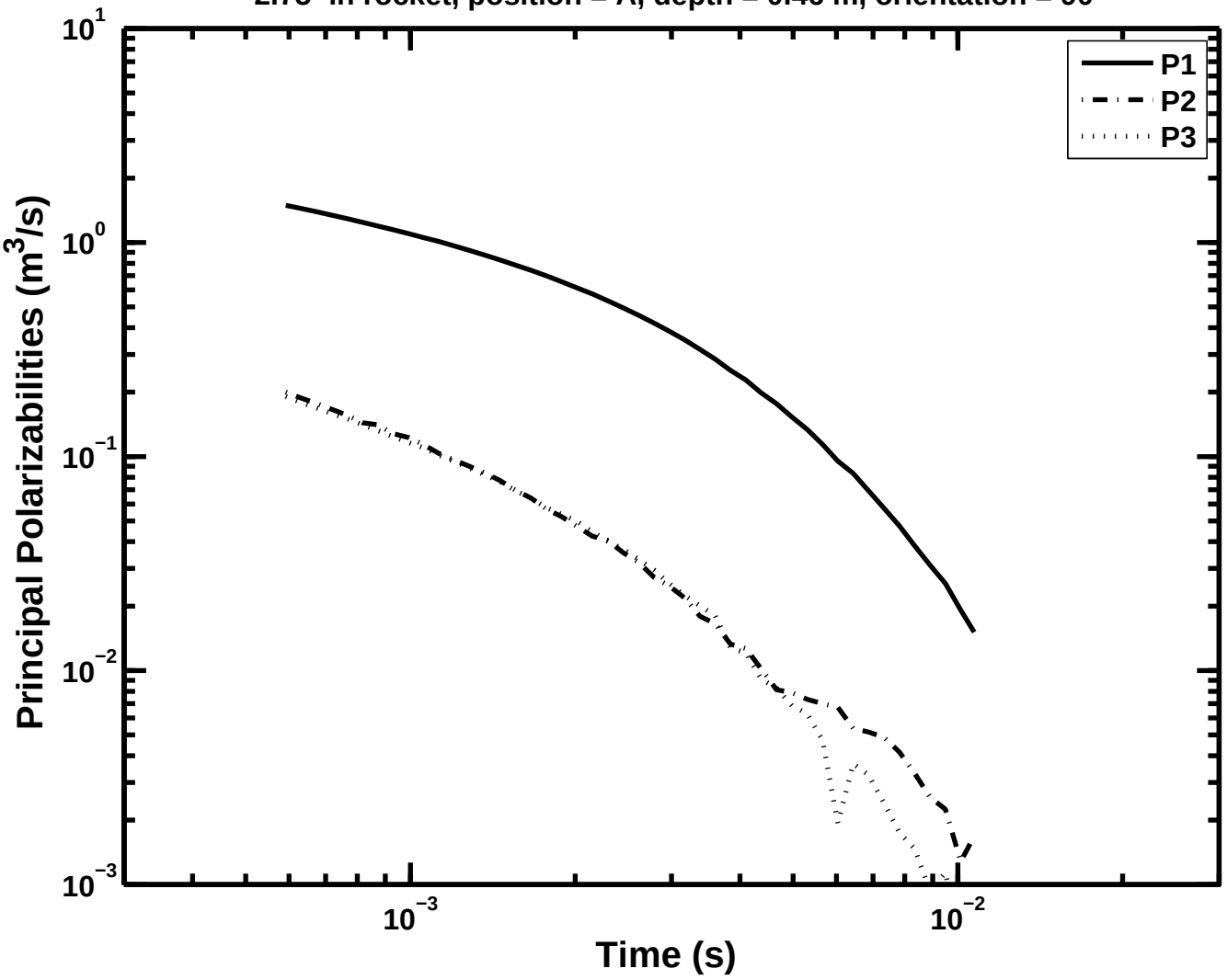

Figure A2−21: Principal polarizabilities as a function of time − 60−mm mortar, position = A, depth = 0.47 m, orientation = 90

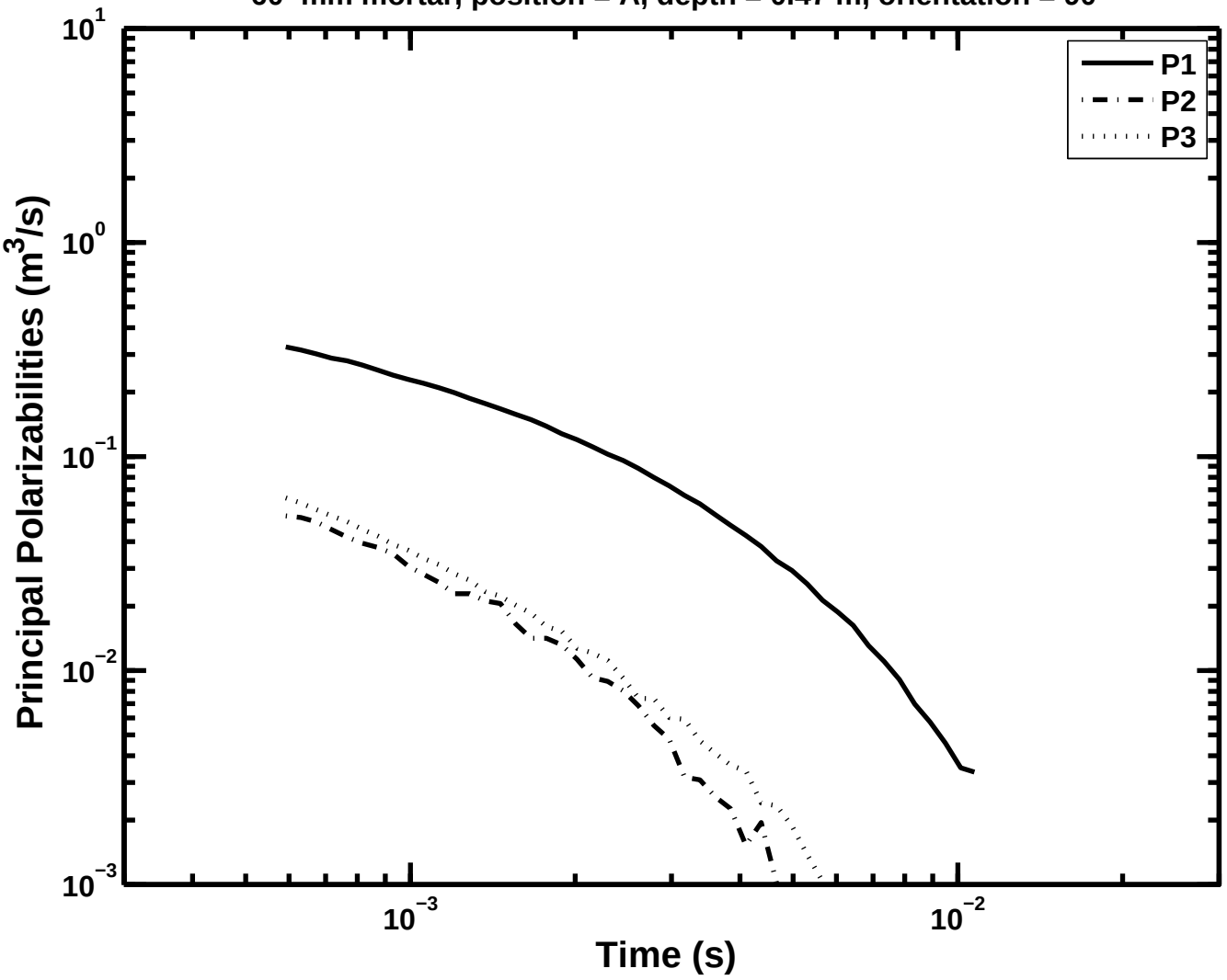

Figure A2−22: Principal polarizabilities as a function of time − 60−mm mortar, position = A, depth = 0.47 m, orientation = 0

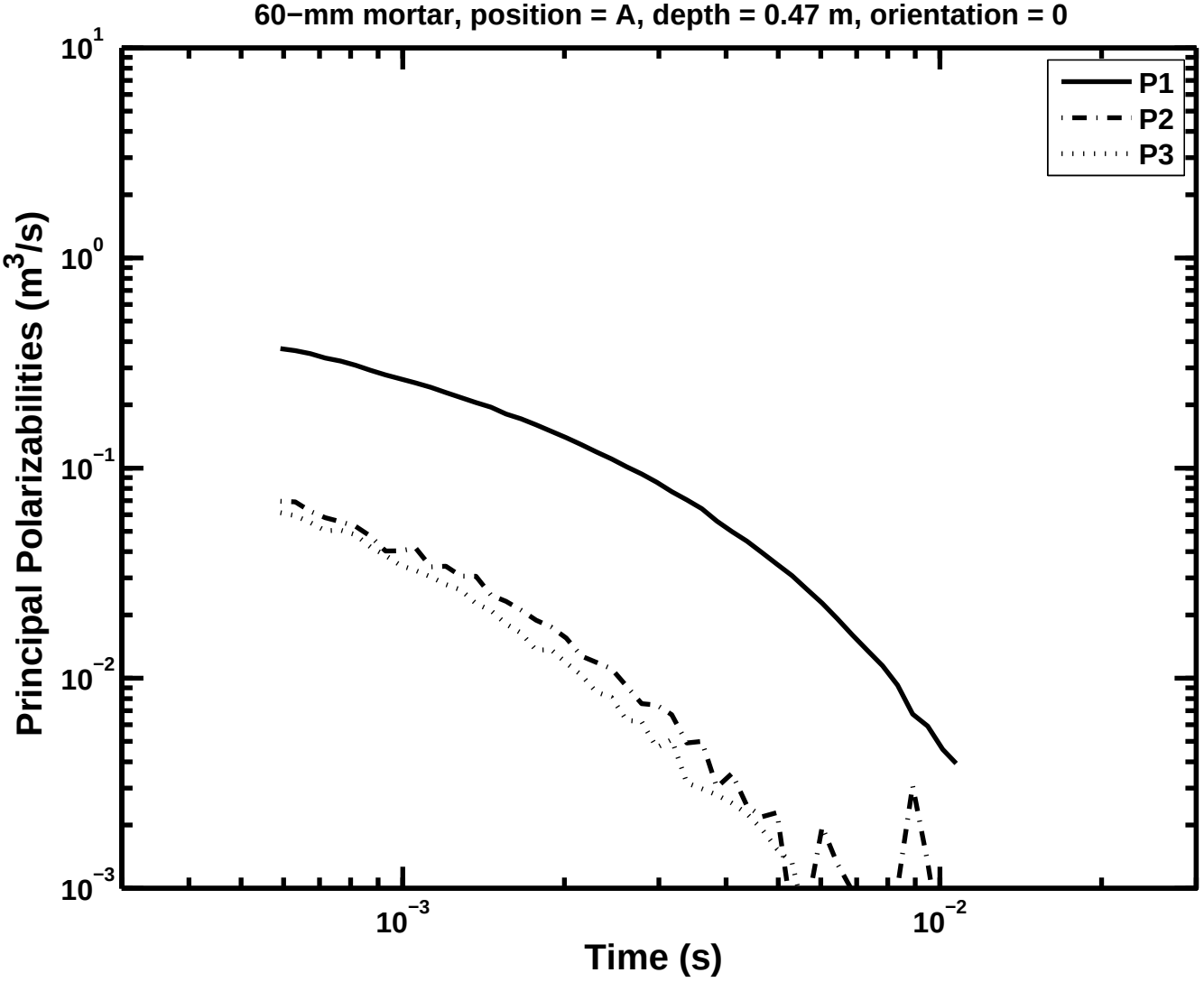

Figure A2−23: Principal polarizabilities as a function of time − 60−mm mortar, position = C, depth = 0.47 m, orientation = 90